Spacecraft Attitude Determination

A Magnetometer Approach

Bak, Thomas

Publication date:
1999

Document Version
Også kaldet Forlagets PDF

[Link to publication from Aalborg University](#)

Citation for published version (APA):
Bak, T. (1999). *Spacecraft Attitude Determination: A Magnetometer Approach*. Aalborg Universitetsforlag.

Spacecraft Attitude Determination
- a Magnetometer Approach

Ph.D. Thesis

Thomas Bak

Department of Control Engineering
Aalborg University
Fredrik Bajers Vej 7, DK-9220 Aalborg Ø, Denmark.

This thesis was typeset using Latex2e in `report` document class.

Drawings were made in CORELDRAW™ from Corel Corporation.
Graphs were generated in MATLAB™ from The MathWorks Inc.

Preface and Acknowledgments

<div align="right">
August 1999, Aalborg, Denmark
Thomas Bak
</div>

Summary

This thesis describes the development of an attitude determination system for spacecraft based only on magnetic field measurements. The need for such system is motivated by the increased demands for inexpensive, lightweight solutions for small spacecraft. These spacecraft demands full attitude determination based on simple, reliable sensors. Meeting these objectives with a single vector magnetometer is difficult and requires temporal fusion of data in order to avoid local observability problems. In order to guaranteed globally nonsingular solutions, quaternions are generally the preferred attitude specifier.

This thesis makes four main contributions. The first is the development of a quaternion based Kalman filter, which is linearized using an exponential map of the correction quaternion. The state space is reduced in dimension, and a covariance singularity is avoided. The second contributions is a detailed study of the influence of approximations in the modeling of the system. The quantitative effects of errors in the process and noise statistics are discussed in detail. The third contribution is the introduction of these methods to the attitude determination on-board the Ørsted satellite. Implementation of the Ørsted filter is discussed and the predicted results are presented.

Finally the Kalman filter/smoother is applied to magnetometer data from the Freja satellite. Data is processed off-line, which enables us to estimate a high fidelity dynamic model of the spacecraft. Combined with a careful detection of field perturbations, the result is an significant improvement in accuracy when compared to previous results. The results allow researchers to fully utilize the electric field science measurements.

Synopsis

Denne Ph.D.-afhandling beskriver udviklingen af et retningsbestemmelsessystem til brug i forbindelse med satellitter. Systemet er baseret på anvendelsen af magnetometre som eneste retningssensor. Brugen af sådanne systemer er motiveret af de forøgede krav til billige, lette løsninger for små satellitter. Disse kræver fuld retningsinformation baseret på simple, pålidelige sensorer. For at kunne garantere globale ikke-singulære løsninger, kræves generelt quaternions til beskrivelsen af retningen. At møde disse krav er vanskeligt med et enkelt vektor magnetometer instrument, og kræver tids fusion af data for at undgå problemer med lokal observerbarhed.

Denne afhandling har fire hovedbidrag. For det første udvikles et quaternion basseret Kalman filter, som lineariseret ved hjælp af et exponentielt map af filter korrektionen. Tilstandsrummet bliver reduceret i dimension and en kovariance singularitet undgåes. Det andet bidrag er et detaljeret studie af inflydelsen fra tilnærmelser i modelleringen af systemet. Den kvantitative effekt af fejl i process og støjbeskrivelserne diskuteres i detalje.

Det tredie bidrag er en introduktion of ovenstående metoder i forbindelse med retningsbestemmelse ombord på Ørsted satellitten. Implementation af Ørsted filtret bliver diskuteret og de forudsagte resultater præsenteres. Endvidere evalueres resultater opnået med flight systemet fra Ørsted.

Endelige bliver et Kalman filter/smoother anvendt på magnetometer data fra Freja satellitten. Data processeres off-line, hvilket muliggør estimering af en meget nøjagtig dynamisk model of rumfartøjet. Dette har i kombination med med omhyggelig detektion af felt perturbationer, muliggjort en bestemmelse af retningen af Freja med hidtil uset nøjagtighed.

Contents

List of Figures

List of Tables

Nomenclature

Symbols

$\mathbf{A}$	General 3×3 rotation matrix
$J(\cdot)$	Wahba's loss function
$\mathbb{R}^3$	Three dimensional real space
$SO(3)$	Special orthogonal group of order three
$\boldsymbol{\theta}$	Rotation vector
$\mathbb{H}$	The quaternion group
$\mathbb{R}$	Real space
S^3	Unit sphere in four-dimensional space
S^2	Unit sphere in three-dimensional space
$\boldsymbol{\Lambda}_p$	Left operator, matrix representation of quaternion product
$\boldsymbol{\Xi}_p$	Right operator, matrix representation of quaternion product
$\boldsymbol{\Omega}(t)$	Skew symmetric matrix (4×4), quaternion kinematics.
$\boldsymbol{\omega}(t)$	Angular velocity vector.
$\boldsymbol{h}_b(t)$	Angular momentum
$\boldsymbol{n}(t)$	Torque vector
$\boldsymbol{I}$	Moments of inertia tensor (3×3)
$\boldsymbol{\omega}_b(t)$	Angular velocity in the body frame
$\boldsymbol{n}_{gg}(t)$	Gravity gradient torque vector
$\boldsymbol{\eta}_b(t)$	Unit zenith vector, gravity gradient modeling
$\boldsymbol{x}$	State vector
$\boldsymbol{f}(\cdot)$	Continuous time process model
$\boldsymbol{u}(t)$	Deterministic control input
$\boldsymbol{\beta}(t)$	Brownian motion
$\boldsymbol{v}(t)$	Continuous noise input to process model
$\boldsymbol{Q}(t)$	Spectral density of of $\boldsymbol{v}(t)$
$\boldsymbol{z}_k$	Discrete observation vector
$\boldsymbol{h}(\cdot)$	Observation model
$\boldsymbol{w}_k$	Discrete noise on observation model

$\boldsymbol{R}(k)$	Discrete observation noise covariance
$\hat{\boldsymbol{x}}_{i\|j}$	Estimated conditional mean of state
$\boldsymbol{P}_{i\|j}$	Conditional covariance
Z_j	Sequence of observations
$\tilde{\boldsymbol{x}}_{k\|k-1}$	Error in the prediction at time t_k given observations up to time t_{k-1}
$\boldsymbol{\nu}_k$	Innovation vector
$\boldsymbol{K}_k$	Kalman gain at time t_k
$\boldsymbol{P}^{\nu\nu}$	Innovation covariance
$\boldsymbol{P}^{x\nu}$	Cross covariance, state – innovation
$\boldsymbol{F}(t)$	Linear continuous process model
$\boldsymbol{H}_k$	Linear discrete observation model
$\Delta\boldsymbol{x}$	State perturbation
$\boldsymbol{F}_g$	Linearized gravity gradient
$\boldsymbol{F}_e$	Linearized Euler coupling
$R_m(k)$	Sensor noise description
$R_b(k)$	Reference model noise description
$\boldsymbol{b}_k$	Geomagnetic field measurement
$\Phi(t_{k+1}, t_k)$	State transition matrix
$\boldsymbol{M}(\cdot)$	Observability Grammian
$\boldsymbol{F}_1, \boldsymbol{G}_1, \boldsymbol{H}_1$	Model parameters in field truth model
$\boldsymbol{b}_{tm}(t)$	Field truth model representation of geomagnetic field
$\boldsymbol{i}$	Basis vector in the ECEF coordinate frame
$\boldsymbol{n}_a(t)$	Aerodynamic torque model
$\boldsymbol{T}$	Aerodynamic torque model, diagonal matrix of positive bias time constants
$\boldsymbol{Q}_a$	Aerodynamic torque model, power spectral density
$\boldsymbol{\Sigma}$	Aerodynamic torque model, diagonal matrix, noise variance
s_1, s_2, s_3	Inertia ratios
$\boldsymbol{Q}_s$	Inertia uncertainty
k_s	Empirically found weight on inertia uncertainty
$\boldsymbol{G}_e, \boldsymbol{G}_g$	Euler and gravity gradient coupling
$\boldsymbol{Q}_{wi}$	Inertia uncertainty noise description
$\boldsymbol{Q}_{p1}, \boldsymbol{Q}_{p1}$	P1, P1 process noise
$\boldsymbol{Q}_w, \boldsymbol{Q}_q$	Stabilizing process noise on velocity and quaternion state respectively
$\boldsymbol{U}$	Unit upper diagonal matrix
$\boldsymbol{D}$	Diagonal matrix
$\boldsymbol{\lambda}$	$\boldsymbol{U}_{k-1}^T \boldsymbol{H}_k^T$
$\boldsymbol{A}_g$	Intermediate matrix used in time update
$\boldsymbol{D}_w$	Diagonal matrix used in time update
$\boldsymbol{L}$	Unit lower triangular matrix
$\boldsymbol{E}_i$	Induced electric field

$\boldsymbol{x}^S, \boldsymbol{P}^s$ Smoothed state and covariance estimates

Abbreviations

ACS	Attitude Control System
ADS	Attitude Determination System
APS	Active Pixel Sensor
CCD	Charged Coupled Device
CDH	Command and Data Handler
CM	Center of Mass
CP	Center of Pressure
CPD	Charged Particle Detector
CSC	Compact Spherical Coil (vector magnetometer)
CUSUM	Cumulative sum
ECI	Earth Centered Inertial Coordinate System
ECEF	Earth-Centered-Earth-Fixed coordinate system
EKF	Extended Kalman filter
ESA	European Space Agency
FDIR	Fault detection, Isolation, and Reconfiguration
FOAM	Fast Optimal Attitude Matrix
GFZ	GeoForschungsZentrum, Potsdam
GPM	Greenwich Prime Meridian (GPM)
GPS	Global Positioning System
IAGA	International Association of Geomagnetism and Aeronomy
IGRF	International Geomagnetic Reference Field
ISSD	Internet Supported Space Database
JPL	Jet Propulsion Laboratory, Pasadena
LEO	Low Earth Orbit
LVLH	Local Vertical Local Horizontal coordinate system
MME	Minimum Model Error
NASA	National Aeronautics and Space Administration
NORAD	North American Aerospace Defense Command
OBCS	Object Control Structure
OVH	Overhauser scalar magnetometer
PCS	Principal Coordinate System
REQUEST	REcursive QUaternion ESTimator
RMS	Root Mean Square
R-T-S	Rauch-Tung-Striebel smoother
SCB	Spacecraft Body Coordinate system
RTSF	Real Time Sequential Filter
SGP4	Special General Perturbation model of order four
STVF	Statens Teknisk Videnskabelige Forskningsråd (Danish Research Council)

QUEST	QUaternion ESTimator
SVD	Singular Value Decomposition
SAMPEX	Solar Anomalous and Magnetospheric Particle Explorer

Terminology

Apogee	is the point at which a satellite in orbit around the Earth reaches its farthest distance from the Earth.
Attitude	of a spacecraft is its orientation in a certain coordinate system.
Altitude	is the distance from a reference *geoid* to the satellite.
Ecliptic	is the mean plane of the Earth's orbit around the Sun.
Eclipse	is a transit of the Earth in front of the Sun, blocking blocking all or a significant part of the Sun's radiation.
Geoid	is an equipotential surface that coincides with mean sea level in the open ocean.
Ionosphere	The region of the atmosphere from about 80 to 480 kilometers above the Earth. The ionosphere has layers of ions formed from atmospheric gasses that have been ionized by ultraviolet radiation from the Sun.
Latitude	is the angular distance on the Earth measured north or south of the equator along the meridian of a satellite location.
Longitude	is the angular distance measured along the Earth's equator from the Greenwich meridian to the meridian of a satellite location.
Mean Anomaly	is the angle from the *perigee* to the satellite moving with a constant angular speed (*orbital rate* ω_o) required for a body to complete one revolution in an orbit. Mean anomaly, M, is $\omega_o \Delta t$, where Δt is the time since last perigee passage.
Orbital rate	is the mean angular velocity of the satellite rotation about the Earth.
Pitch, Roll, Yaw	are the angle describing satellite attitude. Pitch is referred to the rotation about the x-axis of a reference coordinate system, roll to the y-axis, and yaw to the z-axis.
Perigee	is the point at which a satellite in orbit around the Earth most closely approaches the Earth.
Vernal Equinox	is the point where the *ecliptic* crosses the Earth equator going from south to north.
Zenith	is a unit vector in the Control Coordinate System along the line connecting the satellite centre of gravity and the Earth centre pointing away from the Earth.

Chapter 1

Introduction

This thesis describes the design, analysis and development of estimation algorithms to an attitude determination system based on magnetic field measurements. The work has primarily been motivated and supported by the Ørsted satellite project.

Magnetometers are inexpensive, reliable instruments included in the sensor complement of most three-axis stabilized spacecraft designed for near-Earth orbit. The difference between computed and measured magnetic field components is a function of the spacecraft attitude. This makes magnetometer measurements attractive for use in an attitude determination system on small spacecraft. This thesis approaches the problem from an engineering point of view, and practical experience from two case studies forms the basis of the investigation.

1.1   Background and Motivation

Attitude information is required for nearly all space missions. Without reliable attitude estimates mission objectives may be severely compromised. As spacecraft move towards higher levels of autonomy, the demands on spacecraft reliability generally increase. Attitude determination is a key component of most missions and improvements in its accuracy and reliability contribute directly to the success of the mission.

Magnetometers are inexpensive, lightweight, and highly reliable sensors that are carried on most low Earth orbit spacecraft. As they provide us with information about the attitude of the spacecraft they become interesting for small satellite systems. The reliability of magnetometers is demonstrated by the fact

that, only one failure of a magnetometer has ever been reported on missions supported by NASA's Goddard Space Flight Center (Deutchmann *et al.* (1998)). Another example of the use of magnetometers for attitude determination is given by the Earth Radiation Budget Satellite (ERBS). In July 1987 ERBS went into a tumble, which made Sun and Earth sensors unreliable and the gyro telemetry saturated, so that the three-axis magnetometer became the only useful attitude sensor (Challa *et al.* (1997)).

The Earth's magnetic field is primarily a dipole generated largely by currents in the Earth's fluid core. The Earth's magnetic field interacts with and shields us from the solar wind. Coronal mass ejections from the Sun cause changes in the magnetosphere shape and local field strength. These fluctuations are the cause of phenomena like the Aroura Borealis and the Van Allen Radiation Belts. Such perturbations to the main field limit the accuracy of magnetometer based solutions. They are, however, still attractive for missions with relative low accuracy requirements, which require simple inexpensive sensors. Alternatively, missions desiring an inexpensive backup method for a more complex attitude and rate estimation packages may use a magnetometer solution.

In 1998 the Gurwin-II Techsat was launched. The platform was stabilized based on attitude information from a magnetometer only. The *coarse cruise* algorithms has an expected accuracy of 5 deg.. In the *fine cruise* phase, the use of an extended Kalman filter is expected to provide an accuracy of 1-2 deg. (Oshman (1999)).

Two case studies have motivated this work, and the results are presented in two case study chapters.

1.1.1   The Ørsted Case

The first case is defined by the Danish Ørsted Satellite. Ørsted is a small satellite, which was launched by a Delta II launch vehicle February 23, 1999. The primary science objective is to measure the main geomagnetic field, and a magnetometer is carried as part of the science payload (see Figure 1.1).

For low-budget space experiments like Ørsted we desire to provide as much data as possible regarding the dynamics while satisfying severe constraints on the size, weight, power, and cost of the instrumentation package. Attitude determination is therefore based on a gyro-less configuration with a star imager as the primary instrument. Fault tolerance is obtained, through attitude determination based on the science magnetometer as a backup. The backup attitude algorithm for Ørsted has been a primary motivation for the work presented in this
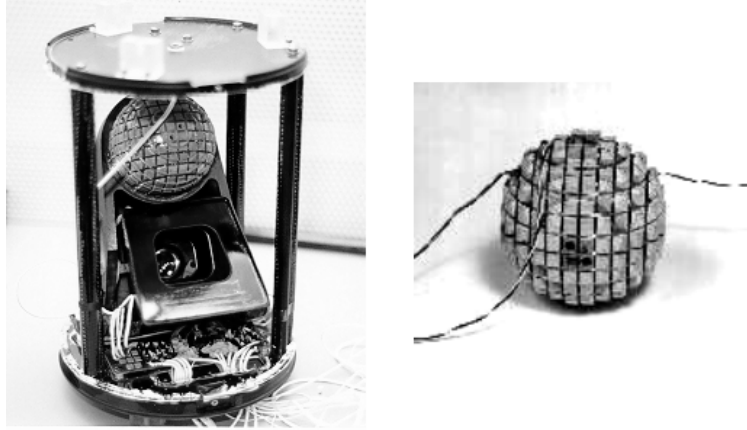
Figure 1.1: *The magnetometer used on the Ørsted satellite (right photo). The magnetometer is mounted on an instrument platform with a star camera (left photo).*

thesis. The focus is not only on developing an estimation algorithm, but also on the system design and implementation. Reliability is a key issue, and integrity monitoring and supervision of the attitude determination system are important issues.

1.1.2 The Freja Case

The other case study deals with the Swedish/German Freja satellite. The Freja attitude is needed in off-line science investigations related to electric and magnetic field studies. The attitude has previously been determined once or twice per orbit using a combination of an Earth horizon sensor and a Sun sensor. This approach does not, however, allow attitude determination in eclipse, as thermally induced inertia variations prevent simple extrapolation. Through the use of magnetometers this thesis will show how attitude estimates can be reconstructed with the required accuracy also during eclipse, where no reliable attitude was previously available. Using the measured magnetic field data in an attitude solution attributes any long periodic changes in the observed field to changes in the attitude of the spacecraft. As the main scientific interest is related to short periodic structures, the use of the same data for attitude estimation should not signifi-

cantly affect the science measurements.

1.1.3   Other Examples

An example of the usefulness of miniature magnetometers may indicate what
the future will bring in terms of the use of magnetometers for spacecraft atti-
tude determination. Researchers at the Jet Propulsion Laboratory have proposed
a mission where a single larger satellite ejects several spinning hockey puck
sized, disposable, free flying satellites in order to make simultaneous spatially
distributed measurements. Each pico-sat carry a miniature 3-axis fluxgate mag-
netometer and a transmitter. After launch from the main satellite, the picosats
transmit sensor readings back to the main satellite where the data is available
for retrieval. After the battery discharges completely, the pico satellite dies, and
eventually burns up in the atmosphere. The on-board magnetometer supports
the science objectives, and provides attitude dynamics information for use in
evaluation of the science data (Clarke *et al.* (1996)).

1.2   Overview of Existing Methods

In 1965, Wahba (1965) posed the problem of finding a proper orthogonal (rota-
tion) matrix given a number (≥ 2) of vector measurements (see Chapter 2 for a
more detailed discussion). Numerous solutions to the problem posed by Wahba
has been proposed over the years (e.g. Lerner (1978), Shuster and Oh (1981),
Markley (1993)). These point estimation algorithms do, however, require at least
two vector measurements, and therefore fail when only one vector measurement
(e.g. magnetometer measurement) is available. The problem is related to observ-
ability. A single three-axis magnetometer measurement can give only two-axes
worth of attitude information. At any given time point the rotation about the
reference vector can not be resolved.

Under the right circumstances the attitude can be determined using measure-
ments of a single reference vector (Psiaki *et al.* (1990)) by using recursive es-
timation algorithms and dynamic models. The measurements are processed se-
quentially and retain the information content of past measurements, thereby re-
ducing the observability problem by temporal fusion with past data. The most
commonly used technique for attitude estimation is the Kalman filter (Kalman
(1960)).

Very few (if any) on-board attitude determination systems have attempted to

use only magnetometer data to estimate attitude. This is most likely due to the apparent low accuracy of the measurements. The accuracy of a magnetometer based attitude solution is mainly limited by:

Calibration Magnetometers are inherently nonlinear devices and an accurate in-flight calibration of the magnetometer is required to get to the specified accuracy.

Magnetic cleanliness The spacecraft has to be magnetically clean to minimize disturbances in the observations and well as disturbances in terms of torques acting on the spacecraft.

Accurate timing In order to correlate the measurements and the reference field vectors, accurate timing of the measurements is needed.

Perturbations to the main field Perturbations to the main field may vary in magnitude from fractions of a nT to thousands of nT (Langel (1987)). This inaccuracy in the knowledge of the Earth's field model easily produces errors of 0.4 deg. about each axis.

Furthermore the complexity of spherical harmonics models of the Earth's magnetic field as well as the complexity of the attitude estimator, may prevent the use of magnetometer based attitude solutions.

1.3   Objectives and Contributions

The main contributions of this thesis are as follows:

– The issue of temporal fusion of data is addressed. It is shown how temporal fusion of data may supplement locally unobservable measurement in a way such that the system is observable over time.

– It is argued that most practical implementations of estimators require approximations. The quantitative effects of the approximation errors in the process and noise statistics are discussed in detail.

– The covariance singularity resulting from the quaternion constraint is demonstrated and the use of quaternions in the extended Kalman filter addressed.

- The role of the quaternion in the Kalman filter update is addressed based on a power series of an exponential map.

- A significant contribution of this thesis is the complete design, implementation, and test of an attitude determination system for the Ørsted satellite. The Ørsted magnetometer based solution solved the initial problem of providing attitude during all mission phases and in case of star camera dropout.

- The demonstration of the Ørsted attitude determination based on results from on–board attitude determination system. Magnetometer based results are compared with star camera attitude as a reference. The magnetometer based solution has been used frequently since the start of the Ørsted operation due to frequent star camera dropout.

- The demonstration of an attitude reconstruction algorithm working flight data from the Freja spacecraft. The attitude reconstruction algorithm solved the initial science problem, getting attitude during eclipse to the specified accuracy. The accuracy was enhanced significantly by detecting and avoiding perturbations to the field model.

- It is demonstrated how a single three-axis magnetometer provides a great deal of information when the data are appropriately processed.

While this thesis focuses on the specific problem of magnetometer based attitude determination the techniques have much wider potential in the design of navigation/attitude estimators.

1.4 Thesis Outline

The thesis is organized as follows:

- **Chapter 2, Attitude Determination in Perspective** This chapter provides an overview of the diverse field of attitude determination. A brief overview of attitude sensors most commonly used in attitude determination systems are given with special emphasis on the measurements obtained from a fluxgate type magnetometer. A brief introduction to deterministic and recursive approaches to attitude estimation are provided.

– **Chapter 3, Attitude and Spacecraft Motion Models** This chapter intro-
duces a number of attitude representations with the focus on quaternions.
An exponential map formulation is presented, which allow an series ex-
pansion of the quaternion in terms of 4×4 skew symmetric matrices.
Satellite motion models are derived and the dominant disturbance torques
described.

– **Chapter 4, Attitude Estimation** This chapter considers estimation based
on extended Kalman filtering. Its structure and operation is described,
and the application to nonlinear systems is examined. It is shown how
the Kalman filter predictions allow temporal fusion of the measurements
thereby avoiding a local observability problems, which arise when using
magnetometers as the only reference sensor. The issue of approximate
models is also addressed and the effects on the noise statistics quantified.
The issue of preserving the norm of the quaternion in the Kalman filter
as well as covariance singularity problems related to a full state estimator
are discussed. Finally an attitude estimator solution based on a quaternion
vector update is outlined.

– **Chapter 5 Ørsted Attitude Estimation** The first application, the Ørsted
satellite is described. Two different process models are described and their
noise statistics discussed in detail. The chapter summarizes and evaluates
the performance of the two algorithms. An algorithm is selected and fur-
ther analyzed, and the predicted performance of the Ørsted attitude algo-
rithm is presented.

– **Chapter 6 Implementation and Results from Ørsted** It is well–known
that the Kalman filter in its original formulation is sensitive to numerical
inaccuracy and potential instability. The numerical behaviour of the algo-
rithm is therefore addressed and a brief description of the issues related to
a fixed point Ada implementation for Ørsted is given. Finally results from
the on-board estimator are presented. The results from the magnetome-
ter based attitude solution are compared to star camera attitudes thereby
providing an assessment of the absolute accuracy.

– **Chapter 7 Freja Attitude Estimation** The second application, the Freja
satellite is described. The chapter summarizes and evaluates the perfor-
mance of the attitude reconstruction algorithm applied to Freja data. The
required accuracy and the implications on the estimator design are dis-

cussed. The solution approach is addressed and reconstruction results are presented. Periods with disturbed magnetic field measurements are detected using a statistical test.

– **Chapter 8 Conclusion** This chapter gives concluding remarks and recommendations for future work.

Chapter 2

Attitude Determination in Perspective

Obtaining accurate attitude information is a fundamental aspect of most space missions. Without reliable estimates of the spacecraft attitude, the ability to control the spacecraft and send data back to Earth, or meet other mission objectives may be jeopardized.

Sensor information is generally combined in an attitude determination system to provide the best possible estimates at all times. Depending on the requirements of the mission, the attitude determination may be performed in real-time on-board, or alternatively processed in batches on the ground based on information down-linked from the spacecraft.

Attitude determination systems are a diverse field, but fundamentally they all require a measurement system that includes sufficient sensors to enable that attitude information is extracted with the necessary accuracy. Section 2.1 gives a brief overview of attitude sensors most commonly used in attitude determination systems. Special emphasis is put on the measurements obtained from a fluxgate type magnetometer. Section 2.2 introduces different solution approaches that have been investigated over the last decades.

2.1 Attitude Sensors

This section provides a general overview of present attitude sensor technology. Only salient features are highlighted and the section is intended to be informative rather than complete. It should also be noted, that sensors evolve rapidly, and

new more precise and lighter sensors are continuously developed.

There are basically two classes of sensors commonly used in attitude determination systems

– Inertial sensors

– Reference sensors

The two classes of sensors are in most practical implementations used to complement each other in a measurement system. Reference sensors typically provides noisy vector observations at a low frequency. Rate information from the inertial sensor (e.g. gyroscopes) is often fed forward through a state estimator as a prediction to be corrected by observations from the reference sensor, thereby complementing the reference sensor. Recent advances in reference sensors has prompted for gyroless attitude determination systems which are very interesting for inexpensive small satellite missions, such as Ørsted.

2.1.1   Inertial sensors

Inertial sensors consists of sensors that measure rotation and/or translational acceleration relative to an inertial frame. The sensors are subject to random drift and bias errors, and as a result, the errors are not bounded. In order to provide an absolute attitude, regular updates are performed, based on references such as the Sun, stars, or the Earth. Traditional inertial reference units are mounted in a multi axis gimbal assembly. While accurate, gimballed units are mechanically complex, heavy, and use more power than the increasingly popular strapdown units. Strapdown units are typically composed of an orthogonal three-axis set of inertial angular rate sensors and accelerometers. The inertial sensors are directly mounted (strapdown) to the spacecraft structure. Today, strapdown accuracies compare to gimballed units (Larson and Wertz (1992)). Strapdown units often use rate gyros which measure only changes in attitude. A number of new solid-state concepts have become available in recent years, such as fiber optic and piezo electric quartz gyros, resulting in decreased size, weight, and cost. Gyros typically have a drift rate of down to 0.002 deg./hour.

2.1.2   Reference Sensors

A reference sensor measures the direction of a known vector e.g. the Sun pointing vector. The vector measurement is a function of spacecraft attitude, making

it attractive for attitude determination. The direction of a known vector is typically measured as (*i*) all three vector components, or (*ii*) only a direction (line of sight). The vector magnetometer is a typical example of the first type, whereas sun sensors represent the latter.

One sample from a reference sensor does not provide full attitude information; a Sun sensor cannot detect any rotation of spacecraft about the Sun vector, for example. Two vector directions, ideally orthogonal are needed for complete attitude information. The uncertainty of a reference sensor is made up of two parts, the accuracy of the sensor itself and the accuracy of the reference it uses. Stars provide the most accurate sources, with the Sun and Earth being progressively less accurate references.

Sun sensors The Sun provides a well defined unambiguous reference vector. Sun sensors are visible light detectors, which measure one or two angles between their mounting base and incident sunlight. Sensors range from analog presence detectors to digital instruments which measure the sun direction to an accuracy down to one arc-minute.

Sun sensors are popular, accurate and reliable, but require clear fields of view. Since most low-Earth orbits include eclipse periods, the attitude determination system must provide some way of handling the regular loss of Sun reference. Typical sun sensor accuracy range from 0.005 deg. to 4 deg. (Larson and Wertz (1992)).

Star sensors Star sensors can be trackers or scanners, the latter being mainly used on spinning spacecraft. Charged-Coupled Device (CCD) sensors or Active Pixel Sensors (APS) provides a relatively inexpensive way to image the sky and extract information about stellar locations. Any vehicle motion will show up as a shift of the stars in the field of view.

A star camera measures the elevation of the line of sight to a star as projected onto mutually perpendicular planes which contain the sensor boresight axis. The locations of two or more stars on the sensor, along with their locations in inertial coordinates are sufficient to determine the attitude of the camera with respect to an inertial frame of reference. The star camera is generally sensitive to large angular velocities of the spacecraft as this causes a smearing of the star images on the sensor. Current trends in star sensor technology are treated in Padgett *et al.* (1997). Typical accuracy range from arc seconds to arc minutes (Larson and Wertz (1992)). For the Ørsted mission the star camera was developed and built

by the Department of Automation at the Technical University of Denmark. The instrument recognizes star patterns in its field of view in any arbitrary direction using on-board star databases. The camera is highly intelligent and autonomous, yet lightweight and low power consuming. The star camera on Ørsted has an accuracy of 5-20 arc seconds (Liebe (1995), Jørgensen (1995)).

Horizon sensors   Horizon sensors are infrared devices that detect the contrast in temperature between space and the Earth's atmosphere. Some nadir-pointing spacecrafts use a wide field-of-view fixed head sensor, which views the entire Earth disk and centers the spacecraft on it, see Reigber (1996). The direct Earth-relative information obtained from Horizon sensors may simplify on-board processing on Earth pointing spacecraft. Typical accuracies for systems using horizon sensors are 0.1 to 0.25 deg., with some applications approaching 0.03 deg. (Larson and Wertz (1992)).

Global Positioning Sensors   A novel use of the Global Positioning System (GPS) or Navstar is to adapt it for use in spacecraft attitude determination (see Melvin and Hope (1993) and Cohen (1992)). Measurements of carrier phase differences of the GPS signal measured by two antennas separated by a baseline fixed in the spacecraft allow the relative range of the two antennas to be determined (except for an integer ambiguity). Reference vectors may be inferred from the GPS satellite ephemerides readily available in the receiver. GPS receivers are now becoming more common on spacecraft for timing and precise orbit determination. Differential carrier receivers are more sophisticated (and expensive) than traditional space receivers, but the benefits from an attitude solution may very well make them common over the next decade.

A GPS attitude determination experiment flown on the radar calibration (RADCAL) spacecraft (Lightsey *et al.* (94)) indicates accuracies of about 0.5 - 1.0 deg. for relatively small baselines (< 1 meter). The dominating disturbance in these high precision applications is related to multipath as described by Bak and Bayard (1997). Most efforts have been in the use of GPS for attitude determination, but a similar radio frequency system for deep space missions (the autonomous formation flying sensor) was addressed by Bak (1997).

Magnetometers   Magnetometers are simple, reliable and lightweight sensors carried on most spacecraft as part of the attitude control system. The combination of three sensor elements mounted on an orthogonal base make up a vector

sensing system. A three axis magnetometer measure directly the direction and intensity of the local magnetic field expressed in the sensor frame. The use of magnetometers for attitude determination is limited to regions with a strong and well known field, e.g. Low Earth orbits. The attitude is determined from magnetometer by comparing the measured geomagnetic field with a reference field determined by a reference model.

The accuracy of magnetometers is not as good as that of star or horizon references due to factors such as:

– Disturbance fields due to spacecraft electronics,

– Model errors in the reference field model,

– External disturbances such as ionospheric currents.

The magnetic field at any location near the Earth can be attributed to a combination of sources located respectively in the Earth's core and crust, and in the Earth's ionosphere and beyond. By far the largest in magnitude is the field from the core, or the *main* field. Near dipolar in nature, the strength of the main field is approximately 60.000 nT (nano Tesla) at the poles and approximately 30.000 nT at the equator.

The field model most often used is the International Geomagnetic Reference Field (IGRF) (Langel (1987)) which is the empirical representation of the Earth's main magnetic field recommended for scientific use by the International Association of Geomagnetism and Aeronomy (IAGA). The IGRF models represent the main field without external sources and they are established as the weighted mean of models developed by a number of agencies. According to Primdahl and Jensen (1984) the field is predicted to within approximately 100 nT. A representation of the IGRF field model is given in Figure 2.1. For a discussion of the field model, see Section B.3.

The temporal variations of the field are slow, with a maximum of about 1% per year. External current systems are time-varying on a scale of seconds up to days, and the resulting near-Earth fields can vary in magnitude from fractions of a nT to thousands of nT. The external current systems are located in the magnetosphere, and in the Earth's ionosphere. The strength and location of these currents vary considerably between magnetically quiet and disturbed times.

The main geomagnetic field has direction as well as magnitude. Given that the main field is curl free, allows a representation of $\boldsymbol{B}$ as the gradient of a scalar
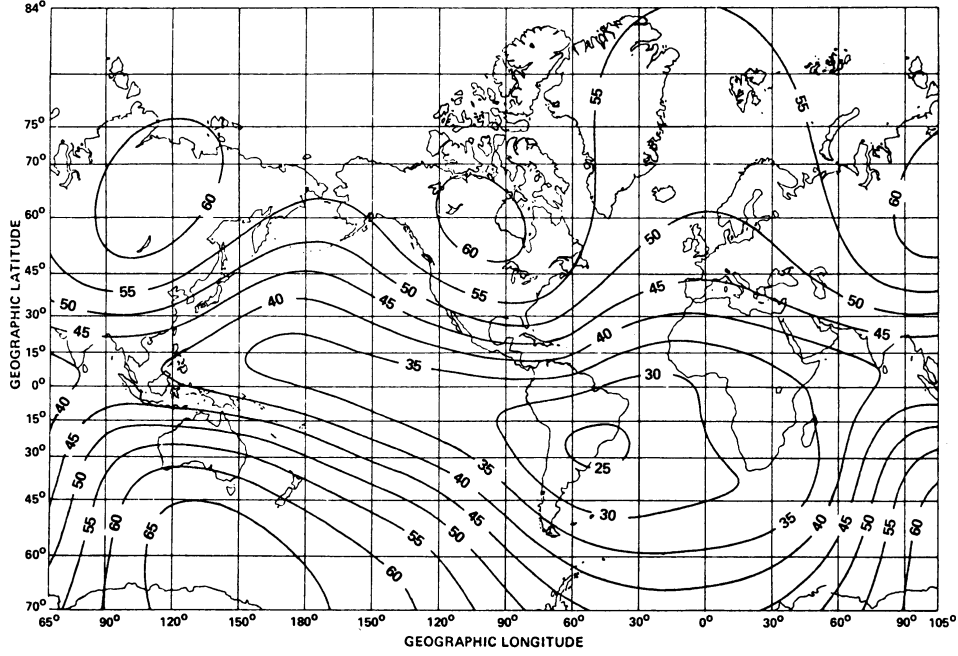
Figure 2.1: *The reference models of the Earth magnetic field represent the main (core) field without external sources. Magnetic field intensity at the Earth's surface in nT based on International Geomagnetic Reference Field (IGRF) model to order 10 for the year 1995.*

potential, V

$$\boldsymbol{B} = -\nabla V \qquad (2.1)$$

It is, however, known that currents flow within the ionosphere and into and out of the ionosphere along magnetic field lines so that, strictly speaking, Equation (2.1) is not valid in the region above about 95 kilometers, where satellite data are acquired. If we write

$$\boldsymbol{B} = \boldsymbol{B}_i + \boldsymbol{B}_e + \boldsymbol{B}_j \qquad (2.2)$$

where $\boldsymbol{B}_i$ is from sources strictly internal to the Earth, $\boldsymbol{B}_e$, is from sources strictly external to the region where data are acquired, and $\boldsymbol{B}_j$ is from sources

within the region where data are acquired, then $\boldsymbol{B}_i + \boldsymbol{B}_e$, can be represented by a scalar potential. In practice, the data used to determine $\boldsymbol{V}$ are selected so as to minimize $\boldsymbol{B}_j$ and the resulting $\boldsymbol{V}$ is assumed to be a good representation of $\boldsymbol{B}_i + \boldsymbol{B}_e$.

External disturbances to the core field, are mainly a problem in the outer magnetosphere and in the polar regions where field aligned currents (Birkeland currents) and ionospheric currents produce magnetic fields perpendicular to the core field (Langel (1987)).

For the Ørsted mission a magnetometer was developed and built by the Department of Automation at the Technical University of Denmark. The instrument is a high performance three axis ringcore fluxgate magnetometer based on a high mu metallic glass sensor. As the Ørsted magnetometer is part of the science mission the accuracy is estimated to 0.5 nT peak-to-peak.

The measurements of the fluxgate sensor are based on an excitation of the core in the sensor by a symmetric current waveform. If no external field is present, the core is driven symmetrically into saturation and the magnetic flux generated in the core contains only odd harmonics. If, however, an external field is present, the magnetic flux generated in the core will be non-symmetrical and even harmonics are generated. In a linear sensor the size of the even harmonics is proportional the external field. A pick-up coil surrounding the excitation coil makes it possible to measure the generated flux and hence measure the magnetic field by detection the contents of second- or higher even harmonics (see Primdahl and Jensen (1984)). The fluxgate ringcore sensor is the preferred design in modern magnetometer design.

2.1.3   Sensor Summary

The choice of attitude sensors for a specific mission is likely to depend mainly on the required orientation of the spacecraft and the required accuracy. Other factors include the given financial resources, the requirements to mass, redundancy, fault tolerance, and data rates. Typical performance and physical characteristics are summarized in Table 2.1.

For full three-axis single point attitude knowledge, at least two reference vector measurements are required. Sensors like GPS and star camera generally provide two or more reference vector measurements at any one time instance.

Frequently, the sensor measurements are made in frames other than the frame of interest for the control system (e.g. local vertical local horizontal (LVLH)),

Table 2.1: *Summary of typical attitude determination sensors. Performance, weight, power and characteristics are listed (based data extracted from ISSD (1999)).*

Sensor	Performance	Weight [Kg]	Power [Watt]	Characteristics
Inertial sensors				
Gyroscopes	Drift: 0.002 deg/hr – 1 deg/hr	3–25	10–200	Normal use involves periodically resetting the reference position to avoid the effects of drift
Reference sensors				
Horizon sensors	0.05 deg – 1 deg (LEO)	2–5	0.3-10	Horizon uncertainties dominate accuracy. High accuracy units use scanning.
Sun sensors	0.005 deg – 4 deg	0.5–2	0–3	Typical field of view 60 deg, coarse sensor uncertainty dominated by Albedo
Star sensors	1 arc sec – 1 arc min	3–7	4–20	Typical field of view 15 deg, limited angular rates
Magnetometers	0.5 deg–5 deg	0.6–1.2	<1	Magnetic field uncertainty is the dominating error source.
GPS	0.5 deg–1 deg	3	3.5–10	Main uncertainty due to multipath and errors in carrier phase tracking.

and the spacecraft ephemerides data are required in order to convert measurements to the desired frame. The data is usually up-linked to the spacecraft from ground tracking, but with the advent of GPS, autonomous navigation systems are increasingly used on satellites.

Table 2.1 indicates the low accuracy of magnetometers relative to high precision sensors such as star sensors. The magnetometer, however, still has an important role to play in attitude determination problems where accuracy requirements are limited. Magnetometers are reliable and almost always available for attitude determination without additional cost.

2.2 Attitude Determination Methods

During the last three decades considerable research effort has been put into the problem of spacecraft attitude determination and numerous solutions to the prob-

lem have been established. In general the solutions fall into two groups:

- Deterministic (point-by-point) solutions, where the attitude is found based on two or more vector observations from a single point in time,

- Filters, recursive stochastic estimators that statistically combine measurements from several sensors and often dynamic and/or kinematic models in order to achieve an estimate of the attitude.

2.2.1 Deterministic (point-by-point) solutions

Three-axis point-by-point solutions, that is, solutions that utilize *only* the vector measurements obtained at a single time point, are widely used in spacecraft application.

The TRIAD algorithm (Lerner (1978)) provides a simple deterministic solution for the attitude. The solutions are based on two vector observations given in two different coordinate systems. TRIAD only accommodates two vector observations at any one time instance. The simplicity of the solution make the TRIAD method interesting for on-board implementations (see Flatley *et al.* (1990)). Bar-Itzhack and Harman (1997) has presented an optimized TRIAD algorithm which provides a weighted result of two TRIAD solutions which is more accurate than the best of the two individual TRIAD solutions that are the basis of the algorithm.

In Wahba (1965), the point estimation problem was posed as the constrained minimization of a loss function

$$J(\boldsymbol{A}) \triangleq \frac{1}{2} \sum_{j=1}^{n} a_j \|\boldsymbol{b}_j - \boldsymbol{A}\boldsymbol{r}_j\|^2 \quad j \geq 2 \tag{2.3}$$

where $\boldsymbol{A} \in SO(3)$ (see Section 3.1 for an explanation of $SO(3)$) is a proper orthogonal rotation matrix and a_j are weights assigned to each vector set. The unit vectors $\boldsymbol{r}_j \in \mathbb{R}^3$ are given in the reference frame, and the unit vectors $\boldsymbol{b}_j \in \mathbb{R}^3$ are the corresponding vectors in the body frame. If the vectors are noise free and the true attitude matrix $\boldsymbol{A}_{true}$ is assumed invariant, then $\boldsymbol{A}_{true}\boldsymbol{r}_j = \boldsymbol{b}_j$ for all j and the loss function is zero.

Equation (2.3) may be transformed into

$$J(\boldsymbol{A}) = \frac{1}{2} \sum_{j=1}^{n} a_j - \text{tr}(\boldsymbol{A}\boldsymbol{B}^T), \text{ where } \boldsymbol{B} = \sum_{j=1}^{n} a_j \boldsymbol{b}_j \boldsymbol{r}_j^T \tag{2.4}$$

It is clear that $J(\boldsymbol{A})$ may be minimized by maximizing $\mathrm{tr}(\boldsymbol{A}\boldsymbol{B}^T)$ under an orthogonality constraint on the attitude matrix.

Numerous methods of attitude determination have developed over the last three decades based on minimizing the Wahba loss function. These point estimation algorithms do, however, require at least two vector measurements, and therefore fail when only one vector measurement is available, or when the observations are parallel. As these solutions are relative simple and as most spacecraft have at least two reference vector measurements available, single frame solutions are widely used. They are, however, not easily adapted to handle faults or periods of poor observability. Some of the more widely used solutions to Wahba's problem are discussed in the following.

Davenport's *q-method* parameterize the rotation matrix by a quaternion and Equation (2.4) may be rewritten as an eigenvalue problem. The optimal quaternion may be found as the eigenvector corresponding to the largest eigenvalue (Wertz (1978)). Several robust (but also complex) general eigenvalue routines exists for solving this problem. The algorithm provides a solution to the minimization problem if such a solution exists.

Methods also exist that compute the attitude matrix $\boldsymbol{A}$ directly. One of these is the Singular Value Decomposition (SVD) Method that was proposed in Markley (1988). The matrix $\boldsymbol{B}$ is Equation (2.4) is decomposed into singular values, leading directly to an optimal attitude solution. Given a robust and effective SVD routine, the SVD method provides a simple solution to the problem. Both eigenvalue and SVD routines are relative complex but robust numerical algorithms exist for implementation.

The QUEST (QUaternion ESTimator) algorithm (Shuster and Oh (1981)) is a fast and popular implementation of the q-method which avoids solving the eigenvalue problem explicitly. In QUEST the eigenvalue problem is reformulated as a problem of solving a characteristic equation. The solution is normally found using Newton-Raphson iteration. The QUEST algorithm was first used for the MAGSAT mission in 1978. A modified recursive algorithm, Filter QUEST (Shuster (1989)) and REQUEST (Bar-Itzhack (1996)) are attempts to include all past measurements in a propagation of the $\boldsymbol{B}$ matrix. Filter QUEST and REQUEST are not really point estimation solutions as they use information form past measurements in the solution. Both Filter QUEST and REQUEST require exact knowledge of the angular velocity and therefore rely on the exactness of a gyro based rate estimate or a dynamic model.

Another alternative is the Fast Optimal Attitude Matrix (FOAM) solution

(Markley (1993)), which provides an iterated solution that avoids the explicit solution of the eigenvalue problem. Instead Newton's method for solving the eigenvalue problem is employed. In contrast to QUEST, FOAM solves for the attitude matrix directly. The comparison study in Markley (1993) compare the efficiency of QUEST and FOAM. The efficiency of the two algorithms is comparable, but FOAM is more robust in some of the cases investigated. In addition FOAM has fewer tuning parameters, which is important in practical implementations.

All of the solutions above provide relatively efficient point solutions to Wahba's problem. In an attempt to extend the methods to situations with only one vector measurement at any given time instance, Challa *et al.* (1997) presented an approach utilizing batches of magnetometer observations and the time derivative of these as the basis for a TRIAD solution. With unknown angular velocity the solution must be supplemented by dynamic equations. The algorithm has been applied to data from the SAMPEX satellite and the accuracy was found to be around 5 deg. (Natanson (1993)). The algorithm is sensitive to errors in the dynamical model and to high spacecraft rates.

The single point estimation algorithms discussed above are summarized in Table 2.2.

Table 2.2: *Summary of common point estimation attitude algorithms.*

Methods	Characteristics
TRIAD	Geometric method, require two non-collinear vector measurements
Q-method	Closed form robust solution based on eigenvalues. May be rather slow due to the required eigenvalue solution.
SVD	Robust solution based on SVD. May be rather slow due to the required SVD solution.
QUEST	An iterated solution that avoids explicitly to solve for the eigenvalues as in the q-method.
FOAM	An iterated solution that avoids explicitly to solve for the eigenvalues as in the q-method.
Filter QUEST, REQUEST	Filtered versions of the quest method. Both methods require exact knowledge of the angular velocity.

2.2.2   Recursive Estimation Algorithms

While many of the above point solutions provide efficient algorithms for on-board implementation, there are a number of shortcomings. First of all, they all require at least two reference vector measurements. Alternatively they need noise sensitive temporal derivatives combined with measurements from a single sensor reading.

Secondly, they do not provide complete state information. Most practical implementations of satellite attitude control systems rely on rate estimates, which, in combination with the point estimation algorithms, may be obtained from gyroscopes. Recent advance in sensor technology and the need for reliable, inexpensive, and lightweight systems for small satellites, however, call for gyroless configurations.

The third shortcoming is that the point estimation algorithms (filter QUEST and REQUEST exempted) only utilize the vector measurements obtained at a single time point to determine the attitude at that time point, and thereby information contained in past measurements is lost. A final shortcoming is that the point estimation algorithms do not provide a consistent setting for estimating stochastic disturbances, biases on gyros etc..

When these shortcomings are undesirable, the increased computational burden and complexity, imposed by estimation algorithms, generally has to be accepted. Recursive estimation algorithms for attitude determination have therefore been investigated intensely.

Kalman Filtering   A frequently used technique in attitude estimation is the Kalman filter (Kalman (1960)). The Kalman filter utilizes an internal state-space model of the system combined with a statistically model of the error associated with the internal model and the measurements. The noise is assumed to be modeled by zero-mean Gaussian processes with known covariance. The Kalman filter minimizes the trace of the error covariance between the estimated and true state. The measurements are processed sequentially and retain the information content of past measurements and thereby effectively filter noisy measurements.

Kalman filters in various forms have proved useful for attitude estimation using a combination of reference vectors and gyro measurements (see the survey paper by Lefferts *et al.* (1982)). In Bar-Itzhack and Oshman (1985) a variant of the Kalman filter was used to estimate the attitude assuming an additive correction.

Under the right circumstances the attitude can be determined without rate

measurements. This approach has been used in a Real-Time Sequential Filter (RTSF) algorithm which propagates state estimates and error covariances using dynamic models (Challa (1993)). High bandwidth star tracker measurements were used in Gai *et al.* (1985) to drive the estimation of attitude and attitude rates. In Fisher *et al.* (1989) a Kalman filter was designed that takes attitude input computed by the QUEST algorithm.

One of the main problems in relation to the Kalman filter is the need for accurate models, process and measurement models as well as stochastic models. Spacecraft parameters e.g. moments of inertia, external disturbance torques and momentum wheel dynamics are typically uncertain and the problem has been addressed by several authors. In Psiaki *et al.* (1990) attitude and attitude rate were determined using only one set of vector measurements. The attitude was propagated using an accurate dynamic model augmented by external torques modeled as a random walk process.

Batch estimators and smoothers based on a Minimum Model Error (MME) approach have recently been proposed by Crassidis and Markley (1997*a*). This approach requires no a priori statistics on the model error as this is determined as part of the solution. Another approach was addressed in Crassidis and Markley (1997*b*), named Predictive Filtering. This approach allows real-time filtering while avoiding the Gaussian state noise assumptions of the Kalman filter. Similar to the MME approach, the predictive filter determines the model-error trajectory as part of the solution.

Nonlinear observers have in recent years received a lot of research interest, see Nijmeijer and Fossen (1999). The main advantage of nonlinear observer theory is that global convergence and stability can be established via Lyapunov techniques for particular classes of nonlinear systems. A large variety of open problems concerning nonlinear observers, however, still exist.

2.3 Summary

This chapter addressed the problem of attitude determination. The basis for any attitude determination is the sensor suite given on the spacecraft. Section 2.1 presented a wide range of sensors commonly used in attitude determination systems. Special focus was given to a presentation of the magnetometer. Finally, Section 2.2 briefly introduced a number of point estimation and recursive attitude determination techniques developed over the last three decades.

Chapter 3

Attitude and Spacecraft Motion Models

In order to describe the motion of a rigid body in space it is convenient to start with a description of its possible orientations. Unlike position, orientation is relatively hard to represent, and a large number of representations are available. This chapter starts by addressing the subject of orthogonal transformations and the fundamental properties of rotations are outlined. Section 3.2 gives are brief review of some of the most commonly used representations. Section 3.3 focuses on the quaternion representation which is used throughout this thesis. An exponential map is introduced that will later be applied in approximations of the spacecraft dynamics. Finally, Section 3.4 presents a description of satellite motion models commonly used in attitude estimation.

3.1   Rotations and Orthogonal Matrices

The development of attitude representations can be found in many books on classical mechanics and on attitude control including Hughes (1986), Wertz (1978), and Shuster (1993).

The objective is to describe rotations of a rigid body in $\mathbb{R}^3$ which has one fixed point but is otherwise free to rotate about any axis through the fixed point. A rigid body is by definition a configuration of points for which the mutual distances are preserved during movement and a rotation of a rigid body must therefore *preserve distance*. Intuitively, rotations must also *preserve the natural orientation* of $\mathbb{R}^3$, i.e. right-handed coordinate systems must be transformed into

right-handed coordinate systems.

Consider a set of three mutually orthogonal vectors (e_1, e_2, e_3) that are of unit length fixed in the point p of a rigid body. As these three vectors span the vector space $\mathbb{R}^3$ and are linear independent, they form a basis or a coordinate system. Given three other vectors (e_1^b, e_2^b, e_3^b) originating at p and fixed in the body. The basic problem of attitude determination is to process vectors represented in these two frames and then solve for the transformation between the two coordinate systems. This is illustrated in Figure 3.1.
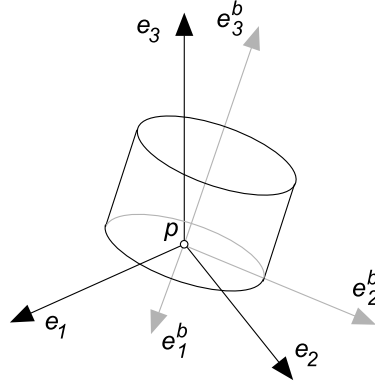
Figure 3.1: *The attitude representation problem: Solve for the transformation between the reference coordinate system (e_1, e_2, e_3) and the body fixed coordinate system defined by the vectors (e_1^b, e_2^b, e_3^b).*

Orthogonal transformations are defined as the group of linear invertible transformations (Jakubczyk and Respondek (1999))

$$T : \mathbb{R}^3 \mapsto \mathbb{R}^3 \tag{3.1}$$

that preserve the standard scalar product

$$\langle T\boldsymbol{v}, T\boldsymbol{w} \rangle = \langle \boldsymbol{v}, \boldsymbol{w} \rangle \tag{3.2}$$

for any $\boldsymbol{v}$, $\boldsymbol{w} \in \mathbb{R}^3$. As the standard scalar product[1] induces distance in $\mathbb{R}^3$, orthogonal transformations preserve the distance between any two points. Equation (3.2) also implies that an orthonormal basis remains orthonormal under

---

[1]$\mathbb{R}^3$ with the standard scalar product, $\langle \boldsymbol{v}, \boldsymbol{w} \rangle = \boldsymbol{v}^T \boldsymbol{w}$ defined is in fact an Euclidian space

transformation. *Rotations* are now defined as those orthogonal transformations that also preserve the orientation of $\mathbb{R}^3$.

The body fixed basis vectors (e_1^b, e_2^b, e_3^b) in Figure 3.1 may now be expressed in the reference frame using coordinates (which is also orthonormal and thereby satisfying the invariance condition in Equation (3.2))

$$T e_i^b = \sum_{j=1}^{3} a_{ij} e_j, \quad i = 1, 2, 3 \tag{3.3}$$

The transformation T is therefore uniquely described by the 3×3 rotation matrix

$$\boldsymbol{A} = \begin{bmatrix} \boldsymbol{a}_1 & \boldsymbol{a}_2 & \boldsymbol{a}_3 \end{bmatrix} \tag{3.4}$$

where $\boldsymbol{a}_j = [a_{1j}, \, a_{2j}, \, a_{3j}]^T$ are column vectors. As the vectors are orthonormal the matrix $\boldsymbol{A}$ satisfies the following conditions

$$\boldsymbol{a}_i^T \boldsymbol{a}_j = \delta_{ij}, \quad i, j = 1, 2, 3 \tag{3.5}$$

where $\delta_{ij} = 1$ for $i = j$, and $\delta_{ij} = 0$ otherwise. These conditions can be reformulated in the form

$$\boldsymbol{A}^T \boldsymbol{A} = \boldsymbol{1} \tag{3.6}$$

where $\boldsymbol{1}$ is the identity matrix. From Equation (3.6) it follows that

$$\det(\boldsymbol{A}^T) \det(\boldsymbol{A}) = \det(\boldsymbol{A})^2 = 1$$

and by that $\det(\boldsymbol{A}) = \pm 1$. Preservation of orientation leads to the following additional condition

$$\det(\boldsymbol{A}) = 1 \tag{3.7}$$

The space of matrices satisfying Equations (3.6) and (3.7) is called the *special orthogonal group* and is denoted by $SO(3)$.

Equation (3.5) implies six constraints on $\boldsymbol{A}$ matrix leaving at most three degrees of freedom. This means that there are six redundant elements among the nine components of matrix $\boldsymbol{A}$. A number of alternative representations are therefore frequently used to parameterize the rotation matrix.

At the beginning of this section, it was stated that physical rotations intuitively would have to preserve distance as well as natural orientation. Using the scalar product on two column vectors $\boldsymbol{v}, \boldsymbol{w} \in \mathbb{R}^3$

$$\langle \boldsymbol{A}\boldsymbol{v}, \boldsymbol{A}\boldsymbol{w} \rangle = (\boldsymbol{A}\boldsymbol{v})^T \boldsymbol{A}\boldsymbol{w} = \boldsymbol{v}^T \boldsymbol{A}^T \boldsymbol{A}\boldsymbol{w} = \boldsymbol{v}^T \boldsymbol{w} = \langle \boldsymbol{v}, \boldsymbol{w} \rangle \tag{3.8}$$

it is clear that applying a rotation matrix to a vector does not change its length. In addition, Equation (3.8) says that the angles between vectors does not change under rotation. To verify the preservation of orientation the following vector product relation is true

$$(\boldsymbol{A}\boldsymbol{v}) \times (\boldsymbol{A}\boldsymbol{w}) = \boldsymbol{A}\,(\boldsymbol{v} \times \boldsymbol{w}) \tag{3.9}$$

The basis for a more physical understanding of rotation is Euler's theorem that states that: *the general displacement of a rigid body with one point fixed is a rotation about an axis through that point* (Goldstein (1950)). The concept is illustrated in Figure 3.2. The rotation angle is θ, and the axis of rotation is given by the unit vector $\boldsymbol{n}$ in three-dimensional space.
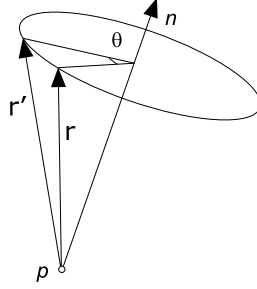
Figure 3.2: *The general displacement of a rigid body with one point fixed is a rotation (θ) about an axis ($\boldsymbol{n}$) through that point.*

With the help of vector algebra it is possible to derive a transformation that describe the rotation in Figure 3.2. The result is the *rotation formula* (Goldstein (1950))

$$\boldsymbol{r}' = \cos(\theta)\boldsymbol{r} + (1 - \cos(\theta))\boldsymbol{n}\boldsymbol{n}^T\boldsymbol{r} - \sin(\theta)\boldsymbol{n} \times \boldsymbol{r} \tag{3.10}$$

which transforms $\boldsymbol{r}$ into $\boldsymbol{r}'$.

Now define the skew symmetric matrix

$$[\boldsymbol{v}\times] \triangleq \begin{bmatrix} 0 & -v_3 & v_2 \\ v_3 & 0 & -v_1 \\ -v_2 & v_1 & 0 \end{bmatrix} \tag{3.11}$$

Applied to a vector it yields the same result as the standard vector cross product, i.e. $[\boldsymbol{v}\times]\boldsymbol{w} = \boldsymbol{v} \times \boldsymbol{w}$. The transformation in Equation (3.10) may hence be written in terms of the rotation matrix defined by

$$\boldsymbol{A}(\theta\boldsymbol{n}) = \cos(\theta)\boldsymbol{1} + (1 - \cos(\theta))\boldsymbol{n}\boldsymbol{n}^T - \sin(\theta)[\boldsymbol{n}\times] \qquad (3.12)$$

where the notation $\boldsymbol{A}(\theta\boldsymbol{n})$ represents the fact that the rotation matrix is parameterized in terms of θ and $\boldsymbol{n}$.

The result in Equation (3.12) may also be expressed in terms of an exponential map as defined by Chevalley (1946). Any orthonormal matrix $\boldsymbol{A} \in SO(3)$ may be expressed in terms of a series of 3×3 skew symmetric matrices defined in Equation (3.11)

$$\boldsymbol{A}(\theta\boldsymbol{n}) = \exp([\theta\boldsymbol{n}\times]) = \sum_{p=0}^{\infty} \frac{1}{p!}[\theta\boldsymbol{n}\times]^p \qquad (3.13)$$

After some tedious manipulation of the power series, Equation (3.13) may in fact be brought into the form in Equation (3.12).

3.2 Attitude Representations

The problem of parameterizing $SO(3)$ has been of interest since 1776, when Euler first showed that $SO(3)$ only has dimension three (Stuelpnagel (1964)). Representations involving more than three parameters are therefore subject to constraints. It was, however, demonstrated by Stuelpnagel (1964) that *no three-parameter set can be both global and nonsingular*. In order to specify any global attitude at least four parameters are needed.

The attitude representations most commonly used besides the rotation matrix are vectors of three and four components. Table 3.1 gives a partial list of the most common parameters and provides a quick comparison of the various means of representing rotations.

The rotation matrix composition follows standard matrix multiplication and represents attitude without any singularities. Apart from analytical studies and for transforming vectors, this representation is little used due to its high dimension and problems in maintaining orthogonality.

The Euler angles, because of their minimum dimension and clear physical interpretations are often convenient for describing or analyzing local motion of

Table 3.1: *Parameterization of the rotation group $SO(3)$. Common parameters used in attitude control systems.*

Representation	Par.	Characteristics	Applications
Rotation matrix	9	– Inherently nonsingular – Intuitive representation – Difficult to maintain orthogonality – Expensive to store – Six redundant parameters	Analytical studies and transformation of vectors.
Euler angles	3	– Minimal set – Clear physical interpretation – Trigonometric functions in rotation matrix – No simple composition rule – Singular for certain rotations – Trigonometric functions in kinematic relation	Theoretical physics, spinning spacecraft and attitude maneuvers. Used in analytical studies
Axis-azimuth	3	– Minimal set – Clear physical interpretation – Often computed directly from observations – No simple composition rule – Computation of rotation matrix very difficult – Singular for certain rotations – Trigonometric functions in kinematic relation	Primarily spinning spacecraft.
Rodriguez (Gibbs)	3	– Minimal set – Clear composition rule – Singular for rotations near $\theta = \pm\pi$ – Simple kinematic relation	Often interpreted as the incremental rotation vector.
Quaternions	4	– Easy orthogonality of rotation matrix – Bilinear composition rule – Not singular at any rotation – Linear kinematic equations – No clear physical interpretation – One redundant parameter – Simple kinematic relation	Widely used in simulations and data processing. Preferred attitude representation for attitude control systems.

a body. Nonlinear composition rules and singularities when representing global attitude limit their usefulness.

The axis-azimuth representation has been used primarily for spinning spacecraft as the parameters can often be computed directly from observations. This representation is similar to the Euler angles, and experiences many of the same problems.

The Rodriguez parameters (Gibbs vector) finds little use and may can be seen as an intermediate step before the quaternion.

The quaternion representation is widely used in simulation, since its kinematic equations are linear and offer none of the analytical problems (singularities) of representations of smaller dimensions. The parameterization of $SO(3)$ is simple as it only involves quadratic terms of the quaternion components, and the quaternion unit norm provides an easy way of maintaining orthogonality of the rotation matrix. Composite rotations are expressed in terms of quaternion multiplication. Quaternions are therefore the preferred parameterization for many modern attitude control systems.

3.3   Quaternions

In this section the representation of rotations in terms of quaternions is discussed. Such a representation is not just concise and elegant but also yields a very efficient way of handling compositions of rotations. The mathematical theory of quaternions was first developed by Hamilton (1866). Quaternions are also known as hypercomplex numbers and denoted by $\mathbb{H}$. Two different representation of quaternions are used in this thesis.

First it is convenient to think of quaternions as complex numbers with a scalar real part, q, and a three-dimensional imaginary part, $\boldsymbol{q}$[2]. Now define a quaternion by

$$\mathbf{q} = q + q_1 \boldsymbol{i} + q_2 \boldsymbol{j} + q_3 \boldsymbol{k} \tag{3.14}$$

where $\boldsymbol{i}, \boldsymbol{j}, \boldsymbol{k}$ are mutually perpendicular unit vectors spanning the space orthogonal to the real part q. For short we write

$$\mathbf{q} = (q + \boldsymbol{q}) \tag{3.15}$$

---

[2]Note that the imaginary part is written in bold italic, whereas the full quaternion is written using upright boldface.

In fact the real part, q, is the projection onto a unit vector $\boldsymbol{e}$ in four dimensional Euclidian space $\mathbb{E}^4$, and the vectors $\boldsymbol{i}, \boldsymbol{j}, \boldsymbol{k}$ are unit vectors in $\mathbb{E}$, the orthogonal complement to the vector space spanned by $\boldsymbol{e}$. In this way quaternions are an extension of the imaginary numbers.

The second representation is suitable for applications of matrix algebra. Quaternions are expressed simply as a four-dimensional column vector

$$\mathbf{q} = \begin{bmatrix} \boldsymbol{q} \\ q \end{bmatrix} \tag{3.16}$$

A quaternion with a null real part ($q = 0$) will be used to represent three dimensional vector in $\mathbb{R}^3$. Likewise, we identify a scalar with a quaternion having vanishing vector part.

Define a left and right operator acting on the quaternion $\mathbf{p}$

$$\boldsymbol{\Lambda}_{\mathbf{p}} \triangleq \begin{bmatrix} p\mathbf{1} - [\boldsymbol{p}\times] & \boldsymbol{p} \\ -\boldsymbol{p}^T & p \end{bmatrix} \quad \text{and} \quad \boldsymbol{\Xi}_{\mathbf{p}} \triangleq \begin{bmatrix} p\mathbf{1} + [\boldsymbol{p}\times] & \boldsymbol{p} \\ -\boldsymbol{p}^T & p \end{bmatrix} \tag{3.17}$$

The quaternion product operation is then defined as

$$\mathbf{p}\mathbf{q} \triangleq \boldsymbol{\Lambda}_{\mathbf{p}}\mathbf{q} \quad \text{or} \quad \mathbf{p}\mathbf{q} \triangleq \boldsymbol{\Xi}_{\mathbf{q}}\mathbf{p} \tag{3.18}$$

where $\mathbf{p}, \mathbf{q} \in \mathbb{H}$ and the multiplication on the left hand side is a quaternion product, whereas the right hand side multiplication is a normal matrix product. It is obvious from Equation (3.18) that the quaternion product rule is only commutative when the vector parts for the two quaternions are parallel so that the cross product in Equation (3.18) vanish. However, multiplication by a purely scalar quaternion ($\mathbf{q} = q + \mathbf{0}$) is always commutative.

The quaternion conjugate is defined similar to the complex numbers as $\mathbf{p}^* = (p - \boldsymbol{p})$ or alternatively in vector notation $\mathbf{p}^* = [-\boldsymbol{p}^T \; p]^T$. The quaternion norm is defined as

$$\|\mathbf{p}\|^2 = pp + \boldsymbol{p}^T\boldsymbol{p} = \mathbf{p}^*\mathbf{p} \tag{3.19}$$

which is analogous to the Euclidean vector norm. A unit quaternion is a quaternion with norm 1, which may be interpreted geometrically as points on the unit 3-sphere, S^3. The normalization is easily enforced using

$$\mathbf{p}_n = (\mathbf{p}^*\mathbf{p})^{-1/2}\mathbf{p}$$

The remainder of this section will focus on the representation of rotation by the unit quaternion. The symmetric operation on a vector represented as a quaternion with zero real part, $\mathbf{v} \in \mathbb{H}$ by

$$\mathbf{v}' = \mathbf{q}\mathbf{v}\mathbf{q}^* \tag{3.20}$$

where $\mathbf{q}$ is a unit quaternion defines the orthogonal transformation of the vector $\boldsymbol{v}$ as represented by the quaternion $\mathbf{v}$.

By applying successive quaternion product operations (Equation (3.18)), the vector $\boldsymbol{v}$ is transformed into

$$\boldsymbol{v}' = (q^2 - \boldsymbol{q}^T\boldsymbol{q})\boldsymbol{v} + 2\boldsymbol{q}(\boldsymbol{q}^T\boldsymbol{v}) - 2q\boldsymbol{q} \times \boldsymbol{v} \tag{3.21}$$

The correspondence between the quaternion and the rotation matrix $\boldsymbol{A}$ is therefore

$$\boldsymbol{A}(\mathbf{q}) = (q^2 - \boldsymbol{q}^T\boldsymbol{q})\mathbf{1} + 2\boldsymbol{q}\boldsymbol{q}^T - 2q[\boldsymbol{q}\times] \tag{3.22}$$

It is clear that for any quaternion representation of a point in $SO(3)$, $\boldsymbol{A}(\mathbf{q}) = \boldsymbol{A}(-\mathbf{q})$, that is, two antipodal points $\mathbf{q}$ and $-\mathbf{q}$ in S^3 represents the same rotation in $SO(3)$.

By comparison of the result in Equation (3.22) with the result in Equation (3.12) it is clear that the quaternion may be expressed as

$$\mathbf{q} = \cos(\theta/2) + \sin(\theta/2)\boldsymbol{n} \tag{3.23}$$

where $\boldsymbol{n}$ is a unit vector representing the axis of rotation, and θ is the rotation angle. $\cos(\theta/2)$ represents the real part of the quaternion, and $\sin(\theta/2)\boldsymbol{n}$ is the imaginary (vector) part. The division by two in the angle of rotation reflects the fact that $\mathbf{q}$ appears twice in Equation (3.20).

Similar to the rotation matrix in Equation (3.13) the quaternion may also be expressed in terms of an exponential map. Given a rotation by an angle of 2θ about the vector $\boldsymbol{n}$, the quaternion exponential is defined as

$$\mathbf{q}(\theta, \boldsymbol{n}) = \exp(\theta\boldsymbol{n}) = \sum_{p=0}^{\infty} \frac{1}{p!}(\theta\boldsymbol{n})^p \tag{3.24}$$

where $\theta\boldsymbol{n}$ on the right hand side is interpreted as a quaternion with zero scalar part. Note that, as a quaternion product, $\boldsymbol{n}^2 = -1$. By manipulation of the

power series, we find

$$
\begin{aligned}
\exp(\theta\boldsymbol{n}) &= \sum_{p=0}^{\infty} \frac{1}{(2p)!}(\theta\boldsymbol{n})^{2p} + \sum_{p=0}^{\infty} \frac{1}{(2p+1)!}(\theta\boldsymbol{n})^{2p+1} \\
&= \sum_{p=0}^{\infty} \frac{1}{(2p)!}(-\theta^2)^p + \sum_{p=0}^{\infty} \frac{1}{(2p+1)!}(-\theta^2)^p(\theta\boldsymbol{n}) \\
&= \sum_{p=0}^{\infty} \frac{(-1)^p}{(2p)!}\theta^{2p} + \sum_{p=0}^{\infty} \frac{(-1)^p}{(2p+1)!}\theta^{2p+1}\boldsymbol{n} \\
&= \cos(\theta) + \sin(\theta)\boldsymbol{n} \tag{3.25}
\end{aligned}
$$

This is the same result that was achieved in Equation (3.23). The exponential map associated with the attitude matrix was given by a series of 3×3 of skew symmetric matrices in Equation (3.13). The quaternion map in Equation (3.24) is very similar in that it represents a series 4×4 skew symmetric matrices when the quaternion product rule is interpreted in terms of Equation (3.18). This understanding of the quaternions is used in the next section to formulate the kinematic equation for the quaternion.

3.4   Equations of Motion

Thus far, we have examined the general properties of rotations and identified several possibilities for representing them. The next problem to be addressed is rotations that evolve over time, that is a curve on $SO(3)$ representing the various orientations. In the following the equations of motion are presented. The kinematic equations provide the relations between the time derivative of the attitude representation and the angular velocity, while the dynamics (or kinetics) describe the development of angular velocities under influence of external moments.

This section makes use of body (principal) and inertial frames. For a detailed definition of the coordinate frames see Appendix A.

3.4.1   Attitude Kinematics

Before discussing attitude kinematics the useful concept of infinitesimal rotations must be introduced. Infinitesimal rotations are rotations by an infinitesimal small angle of rotation, ϵ, about a unit vector, $\boldsymbol{n}$. Using the exponential map

from Equation (3.24) the corresponding quaternion is given by

$$\mathbf{q}(\frac{1}{2}\epsilon, \boldsymbol{n}) = 1 + \frac{1}{2}\epsilon\boldsymbol{n} - \frac{1}{8}\epsilon^2 + \ldots \tag{3.26}$$

When composed with a quaternion as $\mathbf{q}(\frac{1}{2}\epsilon, \boldsymbol{n})\mathbf{q}$ the series may be understood as a sum of quaternion products alternatively as a series of products with skew symmetric matrices parameterized by the parameters in the sum, and defined by the composition rule, Equation (3.18). As we will see in the following this is in good agreement with an understanding of the tangent plane being a space of 4×4 skew symmetric matrices.

If the attitude is changing with time, then $\mathbf{q}(t + \Delta t)$, the quaternion at time $t + \Delta t$, will differ from $\mathbf{q}(t)$, the quaternion at time t, and

$$\mathbf{q}(t + \Delta t) = \mathbf{q}(\frac{1}{2}\epsilon(t), \boldsymbol{n}(t))\mathbf{q}(t) \tag{3.27}$$

Under the assumption that the rotation is small, the series in Equation (3.26) is truncated to first order, which results in

$$
\begin{aligned}
\frac{1}{\Delta t}\mathbf{q}(t + \Delta t) &= \frac{1}{\Delta t}\left(1 + \frac{1}{2}\epsilon(t)\boldsymbol{n}(t)\right)\mathbf{q}(t) + \mathcal{O}(\|\epsilon\boldsymbol{n}\|^2) \\
&= \frac{1}{\Delta t}\left(\mathbf{1} + \frac{1}{2}\begin{bmatrix} -\epsilon(t)[\boldsymbol{n}(t)\times] & \epsilon(t)\boldsymbol{n}(t) \\ -\epsilon(t)\boldsymbol{n}(t)^T & 0 \end{bmatrix}\right)\mathbf{q}(t) \\
&\quad + \mathcal{O}(\|\epsilon\boldsymbol{n}\|^2)
\end{aligned}
\tag{3.28}
$$

where the main product in the first line is a quaternion product and the second line product is the equivalent matrix product.

Defining the angular velocity $\boldsymbol{\omega}(t)$ as

$$\boldsymbol{\omega}(t) \triangleq \lim_{\Delta t \to 0} \frac{\epsilon(t)\boldsymbol{n}(t)}{\Delta t} \tag{3.29}$$

and taking the limit as $\Delta t \to 0$ Equation (3.28) results in

$$\frac{d}{dt}\mathbf{q}(t) = \frac{1}{2}\boldsymbol{\Omega}(t)\mathbf{q}(t) \tag{3.30}$$

where $\boldsymbol{\Omega}(t)$ is a skew symmetric 4×4 matrix defined as

$$\boldsymbol{\Omega}(t) \triangleq \begin{bmatrix} -[\boldsymbol{\omega}\times] & \boldsymbol{\omega} \\ -\boldsymbol{\omega}^T & 0 \end{bmatrix}, \tag{3.31}$$

These equations are the basis for the integration of attitude. They imply that if we know the history of the angular velocity $\boldsymbol{\omega}(t)$, we may integrate and find $\mathbf{q}(t)$, that is, the attitude history given some initial value of $\mathbf{q}(t_0)$.

The transformation described by the quaternion above determines the interpretation of the angular velocity as defined in Equation (3.29). Given a quaternion describing the rotation from an inertial to a body frame, the angular velocity will necessarily be defined in the body frame as the infinitesimal rotation $\epsilon\boldsymbol{n}$ is defined as the rotation from the body frame at time t to the body frame at time $t + \Delta t$.

Using similar reasoning on the rotation matrix leads to the following kinematic equation

$$\frac{d}{dt}\boldsymbol{A}(t) = -[\boldsymbol{\omega}(t)\times]\boldsymbol{A}(t), \tag{3.32}$$

which is useful when looking at the rate of change of vectors in rotation coordinate systems.

3.4.1.1 Differentiation of Rotating Vectors

The rate of change of a vector as seen by two observers in different reference frames generally differ. Using the product rule for differentiation on $\boldsymbol{v} = \boldsymbol{A}\boldsymbol{v}'$ yields

$$\frac{d\boldsymbol{v}(t)}{dt} = \frac{d\boldsymbol{A}(t)}{dt}\boldsymbol{v}'(t) + \boldsymbol{A}(t)\frac{d\boldsymbol{v}'(t)}{dt} \tag{3.33}$$

Applying the result from Equation (3.32), we have

$$\frac{d\boldsymbol{v}(t)}{dt} = -\boldsymbol{\omega}(t) \times \boldsymbol{v}(t) + \boldsymbol{A}(t)\frac{d\boldsymbol{v}'(t)}{dt} \tag{3.34}$$

3.4.2 Dynamics

The total system angular momentum $\boldsymbol{h}_b(t) \in \mathbb{R}^3$ of a rigid body with respect to its center of mass is given by (see Kane *et al.* (1983)):

$$\boldsymbol{h}_b(t) = \int \boldsymbol{r}_b(t) \times \boldsymbol{v}_b(t)\,dm = \boldsymbol{I}\,\boldsymbol{\omega}_b(t), \tag{3.35}$$

where $\boldsymbol{I} \in \mathbb{R}^{3\times3}$ is the moment of inertia matrix of the body about its center of mass. The vectors $\boldsymbol{r}_b$ and $\boldsymbol{v}_b$ are the position and velocity of a point mass. All vectors are given with respect to the body frame as indicated by the subscript b.

Suppose the rigid body is subject to external torques. If $\boldsymbol{h}_i(t) \in \mathbb{R}^3$ denotes the angular momentum in the inertial frame and $\boldsymbol{n}_i$ the external torques in the inertial frame, then the momentum balance equation yields

$$\frac{d}{dt}\boldsymbol{h}_i(t) = \boldsymbol{n}_i(t)$$

Using the results from Equation (3.34) this equation is transformed to the body frame resulting in

$$\frac{d}{dt}\boldsymbol{h}_b(t) = -\boldsymbol{\omega}(t) \times \boldsymbol{h}_b(t) + \boldsymbol{n}_b(t), \tag{3.36}$$

or

$$\boldsymbol{I}\frac{d}{dt}\boldsymbol{\omega}_b(t) = -\boldsymbol{\omega}_b(t) \times (\boldsymbol{I}\boldsymbol{\omega}_b(t)) + \boldsymbol{n}_b(t) \tag{3.37}$$

which is the well–known Euler equation (Goldstein (1950)). The term $\boldsymbol{n}_b$ is the total of control and external torques.

3.4.3 External Torques

The torque input in Equation (3.37) is dominated by control torques, aerodynamic drag torques, gravity gradient torques, and torques due to residual magnetic dipole moments. Apart from control torques which generally are well described, the latter two dominates in low Earth orbits as seen in Figure 3.3.

For very low orbits the interaction between the aerodynamic drag torques and gravity gradient torques become interesting as described in Bak and Wisniewski (1996) and Bak *et al.* (1996*b*).

Control Input and Residual Magnetic Moment The control torque input on Ørsted is generated by electromagnetic coils (magnetorquers) and the control input torque is hence given by

$$\boldsymbol{n}_{ctrl}(t) = \boldsymbol{m}(t) \times \boldsymbol{b}(t) \tag{3.38}$$

where $\boldsymbol{m}(t)$ is the magnetic moment generated by current in the torquers, and $\boldsymbol{b}(t)$ is the local magnetic field in the body frame. A residual magnetic moments enters into the dynamics in the same way as the control torque, but is not controlled actively.
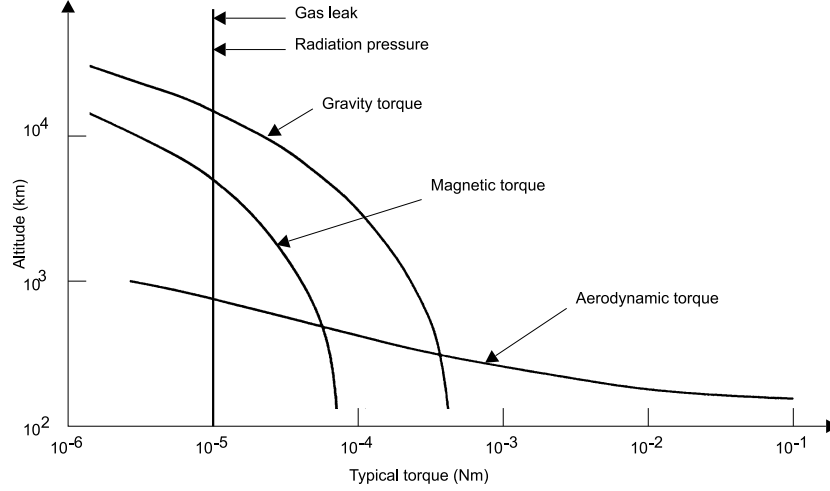
Figure 3.3: *Typical torques on a small spacecraft as a function of orbital altitude above Earth's surface (Bryson (1994)).*

Gravity Gradient   One of the dominating external torques acting on a spacecraft in low earth orbit is the gravity gradient. This torque can be explicitly modeled as (see Wertz (1978))

$$\boldsymbol{n}_{gg}(t) = \frac{3\mu}{r(t)^3}\left(\,\boldsymbol{\eta}_b(t) \times \boldsymbol{I}\,\boldsymbol{\eta}_b(t)\,\right) \tag{3.39}$$

where $\boldsymbol{\eta}_b \in \mathbb{R}^3$ is the unit zenith vector in the body frame, r is the distance to the Earth center and μ is the Earth gravitational constant.

Aerodynamic Drag   Aerodynamic drag is caused by the impact of the atmosphere molecules on the satellite's surfaces. They induces forces and torques about the center of mass. Assuming that the energy of the molecules is totally absorbed on impact the force $d\boldsymbol{f}_{aero}$ acting on one surface element dA is described by (see Wertz (1978)):

$$d\mathbf{f}_{aero} = -\frac{1}{2}C_D\rho v^2(\hat{\mathbf{n}} \cdot \hat{\mathbf{v}}_b)\hat{\mathbf{v}}_b dA \tag{3.40}$$

where dA is a surface element, $\hat{\boldsymbol{n}}$ is an outward normal to the surface, $\hat{\boldsymbol{v}}_b$ is a unit vector in the direction of the translational velocity in the body frame. The ρ is

the atmospheric density, and C_D is the drag coefficient. The total aerodynamic force is determined by integrating over the spacecraft surface.

By approximating the a satellite structure by a collection of simple geometrical elements the aerodynamic torque can be found as the vector sum of the torques on the individual elements composing the satellite surface

$$\boldsymbol{n}_{aero} = \sum_{i=1}^{k} \boldsymbol{r}_i \times \boldsymbol{F}_i, \qquad (3.41)$$

where $\boldsymbol{r}_i$ is the vector from the spacecraft center of mass (CM) to the center of pressure (CP) of the i*th* element. The $\boldsymbol{F}_i$ results from an integration of Equation. (3.40) over the individual elements.

To simplify the expression in Equation. (3.41) assume that the satellite is modeled as a number of plane surfaces. Equation (3.41) then becomes

$$\boldsymbol{n}_{aero} = \frac{1}{2} C_D \rho v^2 \sum_{i=1}^{k} A_i (\hat{\boldsymbol{n}}_i \cdot \hat{\boldsymbol{v}}_b) \hat{\boldsymbol{v}}_b \times \boldsymbol{r}_i \qquad (3.42)$$

where A_i is the surface areas.

In the absence of modeling errors and unknown disturbances, Equations (3.30) and (3.37) propagate the vehicle attitude perfectly for all time (assuming that the initial conditions are known).

3.5 Summary

This chapter focused on the representation and description of the motion of a rigid body in space. Section 3.1 described the subject of orthogonal transformations and addressed some of the fundamental properties of rotations. Section 3.2 reviewed some of the most commonly used representations of rotations. Section 3.3 focused on the quaternion, which provides a globally nonsingular representation of the rotation group $SO(3)$. An overview of the properties of quaternion algebra was given and an exponential map was presented that may be used in approximations. Based on a quaternion attitude representation, the equations of motion for a rigid spacecraft were derived in Section 3.4.

Chapter 4

Attitude Estimation

This chapter considers nonlinear estimation based on Kalman filtering. Attitude determination is an estimation problem, and the estimation algorithm determines how the states are estimated from the sensor information. The attitude determination algorithms in this thesis are based on the Kalman filter. The Kalman filter is based on a structure where predictions made using a model of the system are adjusted using available measurements. This requires accurate models. On the other hand it allows a temporal fusion of data, which is required in order to avoid local observability problems when using magnetometers as the only reference sensor.

The basic assumptions behind the Kalman filter are discussed in Section 4.1 and Section 4.2 give an overview of the filter structure and operation. The application of the filter to nonlinear systems is examined in Section 4.3. This leads to the extended Kalman filter (EKF), which is the most widely used extension of the linear Kalman filter to nonlinear problems.

In Section 4.4 the tradeoff between accurate measurements and an accurate process model is addressed. It is shown how predictions and observations are treated equally in the Kalman filter and an approach to model selection is proposed. It is argued that most practical estimators require approximations. The quantitative effects of errors in the process and noise statistics are discussed in detail.

Section 4.6 addresses the issue of preserving the norm of the quaternion in the Kalman filter as well as covariance singularity problems related to a full state estimator. Finally, Section 4.7 presents a quaternion based Kalman filtering solution, which is later applied in Chapters 5 and 7.

4.1 The Kalman Filter

The Kalman filter has been one of the most widely used estimation algorithms since it was first introduced in Kalman (1960). It has successfully been applied to numerous applications. Given a linear system and observation models as well as a statistical description of the uncertainties associated with these, the Kalman filter is the optimal linear minimum mean-square-error estimator.

The popularity of the Kalman filter arises from a number of important and well-known properties. These include (Grewal and Andrews (1993); Jazwinski (1970); Maybeck (1979a)):

- *Optimality.* The filter is an unbiased, optimal (in the sense of minimum estimation error covariance) estimator for linear systems driven by Gaussian noise.

- *Recursiveness.* The filter combines all available measurements in a recursive data processing algorithm, which allow estimates to be made on-line.

- *Covariance Modeling.* Uncertainties are explicitly modeled using stochastic processes. This provides a technique to deal with uncertainty in the sensors and models, and provides a confidence measure in the estimates.
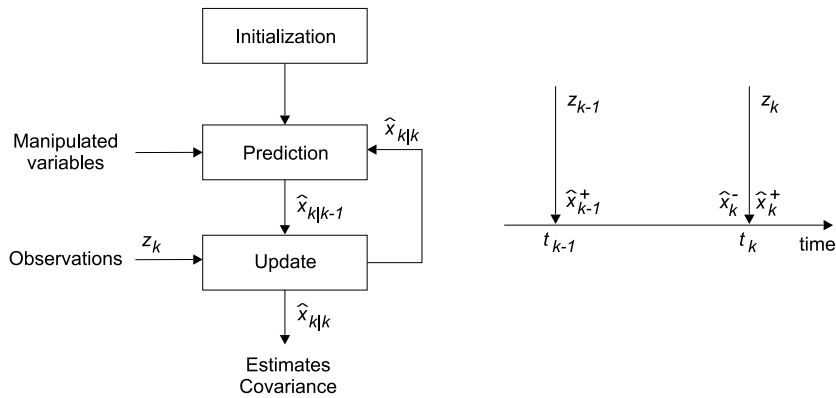
Figure 4.1: *Kalman filter flow. Measurements, z_{k-1} are used to update the estimate $\hat{x}_{k-1|k-1}$. An a priori estimate, $\hat{x}_{k|k-1}$, for the next measurement instance is found based on a process model .*

Figure 4.1 shows the basic operation of the filter. It is first *initialized*— an initial state of the system and an associated covariance matrix are specified. The filter then operates recursively. Each iteration consists of two stages: *prediction* in time followed by measurement *update*. With a new measurement at t_{k-1}, the state estimate is updated to $\hat{\boldsymbol{x}}_{k-1|k-1}$ (the a posteriori estimate). The prediction stage then calculates the a priori estimate for the next sample instance $\hat{\boldsymbol{x}}_{k|k-1}$. The prediction is based on a process model describing the evolution of the system. At time t_k a new estimate is formed as a weighted linear combination of the a priori state and a correction based on the measurement. The weights are found such that the mean-squared estimation error is minimized.

4.1.1   Process and Observation Models

The background for the Kalman filter formulation is a state space description of the system. The state of the system at any time t is expressed using a n dimensional state space vector $\boldsymbol{x}(t)$. The components of this vector may for example include the attitude and velocity of the spacecraft, and possibly relevant parameters to be estimated. Uncertain parameters include environmental torques, components of the inertia tensor for the satellite and possibly sensor calibration coefficients. The state of the spacecraft changes through time due to its dynamics, which are described using a continuous-time stochastic differential equation

$$d\boldsymbol{x}(t) = \boldsymbol{f}\left(\boldsymbol{x}(t), \boldsymbol{u}(t), t\right) dt + d\boldsymbol{\beta}(t) \tag{4.1}$$

where $\boldsymbol{u}(t)$ is a vector of deterministic control inputs, and $\boldsymbol{\beta}(t)$ is a Brownian motion with diffusion $\boldsymbol{Q}(t)$. The current time t is included in the process model to allow it to be time-varying.

This equation may also be written in the less rigorous but for most engineers more familiar (white noise) notation,

$$\frac{d}{dt}\boldsymbol{x}(t) = \boldsymbol{f}\left(\boldsymbol{x}(t), \boldsymbol{u}(t), t\right) + \boldsymbol{v}(t) \tag{4.2}$$

where $\boldsymbol{v}(t)$ is a vector of stochastic disturbances and contains all perturbations, which act on the system that are not described deterministically by the process model. The $\boldsymbol{v}(t)$ is assumed to be a zero mean Gaussian noise process with intensity

$$E\{\boldsymbol{v}(t)\} = \boldsymbol{0}, \quad E\{\boldsymbol{v}(t)\boldsymbol{v}^T(t + \tau)\} = \boldsymbol{Q}(t)\delta(\tau) \tag{4.3}$$

where $\boldsymbol{Q}(t)$ is a positive semi definite matrix and $\delta(t)$ is the delta function. The initial conditions from Equation (4.2), $\boldsymbol{x}_0$ is assumed to be Gaussian with mean $\hat{\boldsymbol{x}}_0$ and covariance $\boldsymbol{P}_0$.

The measurements are acquired at discrete time points, t_k, and are aggregated into a m-dimensional observation vector $\boldsymbol{z}_k$. The values are related to the state of the system according to the sensor model

$$\boldsymbol{z}_k = \boldsymbol{h}\left(\boldsymbol{x}_k, t_k\right) + \boldsymbol{w}_k \tag{4.4}$$

where the observation noise $\boldsymbol{w}_k$ encompasses all the unmodeled effects, which act on the observations, but not on the underlying state of the system itself. The noise term is assumed to be a white Gaussian discrete-time sequence with

$$E\{\boldsymbol{w}_i\} = \boldsymbol{0}, \qquad E\{\boldsymbol{w}_i \boldsymbol{w}_j^T\} = \boldsymbol{R}(i)\delta_{ij} \tag{4.5}$$

where δ_{ij} is the Kronecker delta function. For simplicity is will also be assumed that $\boldsymbol{w}_k$ is independent of the process noise $\boldsymbol{v}(t)$.

4.2   Operation of the Filter

The filter estimates the state by combining measurements taken from the actual system with information embedded in the system model and the statistical description of uncertainty. Let Z_j be a sequence of observations ($Z_j = \{\boldsymbol{z}_1, \boldsymbol{z}_2, \ldots \boldsymbol{z}_j\}$) and define $\hat{\boldsymbol{x}}_{i|j}$ and $\boldsymbol{P}_{i|j}$ to be the conditional mean and covariance, respectively

$$\hat{\boldsymbol{x}}_{i|j} \quad \triangleq \quad E\{\boldsymbol{x}_i | Z_j\} \tag{4.6}$$

$$\boldsymbol{P}_{i|j} \quad \triangleq \quad E\{(\boldsymbol{x}_i - \hat{\boldsymbol{x}}_{i|j})(\boldsymbol{x}_i - \hat{\boldsymbol{x}}_{i|j})^T | Z_j\} \tag{4.7}$$

Consider a single iteration, which propagates an estimate from time step t_{k-1} to time step t_k. At t_{k-1} the estimate of the system state is $\hat{\boldsymbol{x}}_{k-1|k-1}$ with covariance $\boldsymbol{P}_{k-1|k-1}$. The new estimate is $\hat{\boldsymbol{x}}_{k|k}$ with covariance $\boldsymbol{P}_{k|k}$. The change in the state during the interval between t_{k-1} and t_k is modeled by the process model in Equation (4.2), which is integrated to predict the state forward in time. The a priori state vector at time t_k is $\hat{\boldsymbol{x}}_{k|k-1}$. The error in the prediction is defined by

$$\tilde{\boldsymbol{x}}_{k|k-1} \triangleq \boldsymbol{x}_k - \hat{\boldsymbol{x}}_{k|k-1} \tag{4.8}$$

and the covariance of the prediction is

$$\boldsymbol{P}_{k|k-1} = E\{\tilde{\boldsymbol{x}}_{k|k-1}\tilde{\boldsymbol{x}}_{k|k-1}^T|Z_{k-1}\} \tag{4.9}$$

The predicted observation is defined by

$$\hat{\boldsymbol{z}}_{k|k-1} = E\{\boldsymbol{z}_k|Z_{k-1}\} \tag{4.10}$$

which leads to a definition of the innovation given by

$$\boldsymbol{\nu}_k \triangleq \boldsymbol{z}_k - \hat{\boldsymbol{z}}_{k|k-1} \tag{4.11}$$

and as measurements become available at time t_k they are incorporated into the predicted state by finding the weighted sum of the a priori estimate, $\hat{\boldsymbol{x}}_{k|k-1}$ and the innovation vector,

$$\hat{\boldsymbol{x}}_{k|k} = \hat{\boldsymbol{x}}_{k|k-1} + \boldsymbol{K}_k\boldsymbol{\nu}_k \tag{4.12}$$

where $\boldsymbol{K}_k$ is the filter gain matrix (*Kalman gain*). The error in the observation updated estimate is

$$\begin{aligned} \tilde{\boldsymbol{x}}_{k|k} &= \boldsymbol{x}_k - \hat{\boldsymbol{x}}_{k|k} \\ &= \boldsymbol{x}_k - \left(\hat{\boldsymbol{x}}_{k|k-1} + \boldsymbol{K}_k\boldsymbol{\nu}_k\right) \tag{4.13} \\ &= \tilde{\boldsymbol{x}}_{k|k-1} - \boldsymbol{K}_k\boldsymbol{\nu}_k \tag{4.14} \end{aligned}$$

Taking outer products and expectations we get the a posteriori covariance,

$$\boldsymbol{P}_{k|k} = \boldsymbol{P}_{k|k-1} - \boldsymbol{P}_k^{x\nu}\boldsymbol{K}_k^T - \boldsymbol{K}_k\boldsymbol{P}_k^{\nu x} + \boldsymbol{K}_k\boldsymbol{P}_k^{\nu\nu}\boldsymbol{K}_k^T \tag{4.15}$$

where the superscripts on $\boldsymbol{P}$ indicate the cross-covariance matrices.

The weighting matrix $\boldsymbol{K}_k$, is chosen so that the trace of $\boldsymbol{P}_{k|k}$ (the mean squared error) is minimized. The solution was first given by Kalman (1960),

$$\boldsymbol{K}_k = \boldsymbol{P}_k^{x\nu}(\boldsymbol{P}_k^{\nu\nu})^{-1} \tag{4.16}$$

By using the computed gain in Equation (4.16) we get the Kalman update equations

$$\begin{aligned} \hat{\boldsymbol{x}}_{k|k} &= \hat{\boldsymbol{x}}_{k|k-1} + \boldsymbol{K}_k\left(\boldsymbol{z}_k - \hat{\boldsymbol{z}}_{k|k-1}\right) \\ \boldsymbol{P}_{k|k} &= \boldsymbol{P}_{k|k-1} - \boldsymbol{K}_k\boldsymbol{P}_k^{\nu\nu}\boldsymbol{K}_k^T \end{aligned}$$

The covariance prediction from Equation (4.9) determines how information from previous measurements is incorporated into the new estimate.

4.2.1   Linear Models

When the system and observation models are linear, there is an exact closed form solution to the problem. This solution is generally referred to as the Kalman filter. The Kalman filter exists in both continuous, discrete, and continuous/discrete versions. The latter is based on a continuous linear process model and a discrete observation model

$$\frac{d}{dt}\boldsymbol{x}(t) \;=\; \boldsymbol{F}(t)\boldsymbol{x}(t) + \boldsymbol{v}(t) \tag{4.17}$$

$$\boldsymbol{z}_k \;=\; \boldsymbol{H}_k\boldsymbol{x}_k + \boldsymbol{w}_k \tag{4.18}$$

The Kalman filter prediction equations are then given by (Maybeck (1979*a*))

$$\frac{d}{dt}\hat{\boldsymbol{x}}(t) \;=\; \boldsymbol{F}(t)\hat{\boldsymbol{x}}(t) \tag{4.19}$$

$$\frac{d}{dt}\boldsymbol{P}(t) \;=\; \boldsymbol{F}(t)\boldsymbol{P}(t) + \boldsymbol{P}(t)\boldsymbol{F}^T(t) + \boldsymbol{Q}(t) \tag{4.20}$$

The cross-covariances matrices are given by

$$\boldsymbol{P}_k^{\nu\nu} \;=\; \boldsymbol{H}_k\boldsymbol{P}_{k|k-1}\boldsymbol{H}_k^T + \boldsymbol{R}(k) \tag{4.21}$$

$$\boldsymbol{P}_k^{x\nu} \;=\; \boldsymbol{P}_{k|k-1}\boldsymbol{H}_k^T$$

which leads to the familiar observational update equations

$$\boldsymbol{K}_k \;=\; \boldsymbol{P}_{k|k-1}\boldsymbol{H}_k^T \left(\boldsymbol{H}_k\boldsymbol{P}_{k|k-1}\boldsymbol{H}_k^T + \boldsymbol{R}(k)\right)^{-1} \tag{4.22}$$

$$\hat{\boldsymbol{x}}_{k|k} \;=\; \hat{\boldsymbol{x}}_{k|k-1} + \boldsymbol{K}_k \left(\boldsymbol{z}_k - \boldsymbol{H}_k\hat{\boldsymbol{x}}_{k|k-1}\right) \tag{4.23}$$

$$\boldsymbol{P}_{k|k} \;=\; \boldsymbol{P}_{k|k-1} - \boldsymbol{K}_k\boldsymbol{H}_k\boldsymbol{P}_{k|k-1} \tag{4.24}$$

4.3   Estimators for Nonlinear Systems

For nonlinear systems or non-Gaussian noise, the optimal estimator can only be calculated if the entire density function for the state conditioned on the observed measurements is known (Maybeck (1979*b*)). Since it has no general form, an infinite number of parameters are required. In practice high order nonlinear filters are difficult to realize, and virtually all filters, which have been implemented use approximations of some kind. The simplest and most widely used approach is the extended Kalman filter (EKF) (Jazwinski (1970)).

4.3.1   The Extended Kalman Filter

The basic assumption behind the EKF is that the process and observation models are linear on the scale of the error in the estimated state. By re-linearization about each new estimate, the validity of the linearity assumption is less likely to be violated.

Consider a Taylor series expansion of Equation (4.2) about a nominal trajectory defined by $\boldsymbol{x}_n(t)$

$$\dot{\boldsymbol{x}}(t) - \dot{\boldsymbol{x}}_n(t) = \left. \frac{\partial \boldsymbol{f}(\boldsymbol{x}(t), \boldsymbol{u}(t), t)}{\partial \boldsymbol{x}} \right|_{\boldsymbol{x}=\boldsymbol{x}_n(t)} (\boldsymbol{x}(t) - \boldsymbol{x}_n(t)) \qquad (4.25)$$
$$+ \text{ h.o.t. } + \boldsymbol{v}(t)$$

where "h.o.t." are terms of powers greater than one in $(\boldsymbol{x}(t) - \boldsymbol{x}_n(t))$. The result is a first order linear approximation to Equation (4.25)

$$\frac{d}{dt}\Delta\boldsymbol{x}(t) = \boldsymbol{F}\left(\boldsymbol{x}_n(t), \boldsymbol{u}(t), t\right)\Delta\boldsymbol{x}(t) + \boldsymbol{v}(t) \qquad (4.26)$$

where $\Delta\boldsymbol{x}$ is a first order approximation to the state perturbation, and $\boldsymbol{F}(\cdot)$ is the matrix of partial derivatives of $\boldsymbol{f}(\cdot)$ with respect to the state (Jacobian matrix), evaluated along the nominal state and input variables. Truncation of the series introduces second and higher-order errors but, by assumption, the effect of this approximation is negligible (the strength of $\boldsymbol{v}(t)$ may be increased to account for this assumption).

In a similar way the measurement perturbation model is defined by

$$\Delta\boldsymbol{z}_{k|k} = \boldsymbol{H}(\hat{\boldsymbol{x}}_{k|k}, t_k)\Delta\boldsymbol{x}_{k|k} + \boldsymbol{w}_k \qquad (4.27)$$

where $\boldsymbol{H}(\cdot)$ is the Jacobian of $\boldsymbol{h}(\cdot)$, evaluated along the estimated state.

Comparing Equations (4.26) and (4.27) with Equations (4.17) and (4.18), it is clear that the linear filter is applicable to the linearized system provided the Jacobian matrices exist. The output of such a filter would be the optimal estimate of $\Delta\boldsymbol{x}_{k|k}$ denoted $\widehat{\Delta\boldsymbol{x}}_{k|k}$. This estimate is combined with the propagated full state estimate $\hat{\boldsymbol{x}}_{k|k-1}$ to establish an estimate of the total state

$$\hat{\boldsymbol{x}}_{k|k} = \hat{\boldsymbol{x}}_{k|k-1} + \widehat{\Delta\boldsymbol{x}}_{k|k} \qquad (4.28)$$

After the incorporation of the estimated perturbation in the full state estimate the process and measurement models are re-linearized about the new full state.

The perturbation $\widehat{\Delta x}_{k|k}$ is reset to zero, and the *predicted* perturbation $\widehat{\Delta x}_{k+1|k}$ is thus also identically zero.

The best estimate of the state between observations is the full state, which is propagated using the original nonlinear function starting from the initial condition $\hat{x}_{k|k}$ with $v(t) = 0$. The new a priori estimate is then used to re-linearize the filter at time t_{k+1}, which is used in the measurement update equations.

The covariance prediction follows the linear Kalman filter covariance propagation in Equation (4.20) based on process and observation models linearized about the estimate $\hat{x}_{k|k}$.

Given $\widehat{\Delta x}_{k+1|k} = \mathbf{0}$, the extended Kalman filters *measurement update* incorporates the measurements by means of

$$\widehat{\Delta x}_{k+1|k+1} = K_{k+1} \left(z_{k+1} - h(\hat{x}_{k+1|k}, t_{k+1}) \right) \tag{4.29}$$

where K_{k+1} is computed using $P_{k+1|k}$ and H_{k+1} evaluated along the propagated full state estimate. The full state is then determined by Equation (4.28).

The basic operation of the EKF is summarized as follows. The filter is supplied with initial information, including the measurement error covariance, and estimates of the initial state and associated error. These are used to calculate a gain matrix. The error between the state estimate and the measured data is determined and multiplied by the gain matrix to update the state estimate and covariance. The updated covariance and state are used as input to a nonlinear model of the spacecraft dynamics, to predict the projected covariance and state at the next time instance.

Initially, when the state is only a rough estimate, the gain matrix ensures that the measurement data is highly influential in estimating the state. Then, as confidence in the accuracy of the state grows with each iteration, the gain matrix values decrease, causing the influence of the measurement data in updating the state and associated errors to lessen.

Problems Associated with the EKF   The EKF allows us to incorporate nonlinearities in the filter process and observation models while still exploiting linear estimation techniques. However, there are a number of significant problems with the EKF

- The assumption that the second and higher order errors might not be negligible and linearization can introduce significant errors. In practice the

inconsistency is often resolved by introducing additional stabilizing noise terms, which increase the size of the transformed covariance.

– The need to evaluate analytically the Jacobian matrices of the process and observation models. The Jacobian is not guaranteed to exist and there may be considerable implementation difficulties when the system is composed of many states and is highly nonlinear.

– The properties of optimality and stability of linear Kalman filters is not guaranteed for EKF. The modeling errors may cause a filter failure mode in which the filter covariance estimates become inconsistent, which may lead to filter divergence.

A number of higher order analytical and numerical filters have been developed. Many analytical methods achieve greater accuracy by explicitly including more terms in the expansion of Equation (4.25). Second Order Gauss filters (Maybeck (1979*b*)), for example, assume that the system is locally quadratic and includes both first and second order terms. However, the implementation of these filters for even simple systems can be very difficult because it is necessary to calculate the Hessian as well as the Jacobian. Jazwinski (1970) presents a local iteration schemes. The measurement state update is iterated until there is no significant change in consecutive iterates. The iterated solution may reduce the effects on the performance of the EKF due to measurement nonlinearities. Higher order filters and iterated solutions are only considered in cases of extreme system nonlinearities as they are computational more complex than the standard EKF.

Numerical methods are able to address both the performance and implementation difficulties. Rather than approximate the model by arbitrary terms in the Taylor Series, they approximate the prior distribution of $\boldsymbol{x}_{k-1}$ by choosing a number of samples drawn at random. The model is applied to each sample, and the statistics of the transformed samples are used. One approach is Monte Carlo methods as demonstrated by Handschin (1970). The convergence rates are, however, very slow and a large number of samples are required. In Schei (1997) a new linearization method based on a central point finite-difference approximation was presented. This method avoids explicit evaluation of the Jacobian.

The last problem manifests itself as an inconsistency in the covariance estimate

$$\boldsymbol{P}_{i|j} - E\{\tilde{\boldsymbol{x}}_{i|j}\tilde{\boldsymbol{x}}_{i|j}^T|Z_j\} < 0 \tag{4.30}$$

where $\boldsymbol{P}_{i|j}$ is the covariance maintained by the filter, whereas the error vector $\tilde{\boldsymbol{x}}_{i|j}$ is the actual mean-squared error. The inequality in Equation (4.30) is understood as a negative definite difference. In other words, the filter *believes* that it knows the state more accurately than it really does. As a consequence the gain is lower than appropriate. When propagated across over time this may result in an estimation error that becomes progressively worse.

This type of error is often compensated for by modifying the process noise. Increasing $\boldsymbol{Q}(t)$ will increase the gain, and thereby reduce the effect of modeling errors. It will, however, increase the sensitivity to errors in the sensor modeling and the sensor noise. Selecting $\boldsymbol{Q}(t)$ so that the estimated covariance remains high, but at the same time low enough to ensure proper filtering is far from easy. The issue is discussed in further detail in Section 4.5.1.

Ljung (1979) discusses the convergence properties of parameter estimation for linear discrete stochastic systems. An EKF is applied to the problem of estimating states in a linear system model as well as parameters. The reason for divergence is shown to be that the effect on the Kalman gain from parameter changes is not handled properly. Ljung (1979) shows that global convergence of the EKF as a parameter estimator may be achieved by including an extra term in the cross coupling between parameters and states. The term included in the cross coupling is the partial derivative of the Kalman gain with respect to the parameters times the innovations. It is also proposed to parameterize the steady state Kalman gain directly in the filter, rather than the covariance matrices, which leads to the *innovations* representation.

In Zhou and Blanke (1989) the innovations representation is extended to identifying parameters and states of nonlinear state space system models. Second–order terms (bias correction terms) are used in the state expectation and state predictions in order to allow significant nonlinearities. Both discrete and continuous–discrete versions of the algorithm are investigated.

Given these problems with the EKF, it is, however, well–known that extended Kalman filters can be made to operate properly in many practical systems.

4.4   Temporal Fusion of Data

The process model is used to predict the future state of the system. Using the process model the prediction summarizes all the previous observation information.

The estimate at t_k is thus not restricted to using the information contained in z_k. The prediction allow temporal fusion with data from all past measurements.

The temporal fusion of data is best appreciated by considering the information form (Maybeck (1979a)) of the prediction. The amount of information maintained in an estimate $\hat{x}$ is defined to be the inverse of its covariance matrix. The covariance prediction in Equation (4.24) may be rewritten as

$$\boldsymbol{P}_{k|k} = \boldsymbol{P}_{k|k-1} - \boldsymbol{K}_k \boldsymbol{H}_k \boldsymbol{P}_{k|k-1} \tag{4.31}$$

$$\boldsymbol{P}_{k|k} \boldsymbol{P}_{k|k-1}^{-1} = 1 - \boldsymbol{K}_k \boldsymbol{H}_k \tag{4.32}$$

Using this result in combination with the Kalman gain in terms of the predicted covariance, (Maybeck (1979a))

$$\boldsymbol{K}_k = \boldsymbol{P}_{k|k} \boldsymbol{H}_k^T \boldsymbol{R}(k)^{-1} \tag{4.33}$$

the state measurement update may be written as

$$\hat{\boldsymbol{x}}_{k|k} = \boldsymbol{P}_{k|k} \left[\boldsymbol{P}_{k|k-1}^{-1} \hat{\boldsymbol{x}}_{k|k-1} + \boldsymbol{H}_k^T \boldsymbol{R}(k)^{-1} \boldsymbol{z}_k \right] \tag{4.34}$$

A similar expression can be found for the predicted information matrix

$$\boldsymbol{P}_{k|k}^{-1} = \boldsymbol{P}_{k|k-1}^{-1} + \boldsymbol{H}_k^T \boldsymbol{R}(k)^{-1} \boldsymbol{H}_k \tag{4.35}$$

The estimate in Equation (4.34) is therefore a weighted average of the prediction and the observation. Intuitively the weights must be inversely proportional to their respective covariances. Seen in the light of Equation (4.34) predictions and observations are treated equally by the Kalman filter. It is therefore possible to consider the prediction as an observation, $\hat{\boldsymbol{x}}_{k|k-1}$ with covariance $\boldsymbol{P}_{k|k-1}^{-1}$.

Since the prediction and the observation are equivalent, there is a tradeoff between the propagation model and the sensors. The importance of the temporal fusion is demonstrated by the problem of observability in the magnetometer situation. Although the system is not observable about the magnetic field measurements at any single point in time the filter is able to estimate the orientation of the spacecraft due to an accurate prediction of the system state.

4.4.1   Information Flow

Theoretically the Kalman filter forms its estimates from the total amount of collected observation information, Z_k. As the state of the system evolves over time
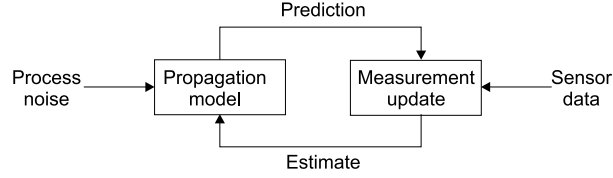
Figure 4.2: *Kalman filter information flow schematic.*

earlier measurements, however, provides less information about the current state of the system. Process noise enter, and uncertainties in the estimates increase through time.

Figure 4.2 depicts a single iteration of the Kalman filter and the flow of information which occurs. On the left, the current estimate is used to predict the future state of the system. As the future state is predicted noise enters the system in two ways

- *Diffusion.* Previous information tends to become diffused over time. For example, if there is some uncertainty in the rate of the satellite then predictions of the future attitude of the spacecraft must include this uncertainty.

- *Process noise.* The system does not evolve according to the deterministic system model, the discrepancy is process noise.

These two effects can be clearly seen in the (linearized) covariance prediction

$$\boldsymbol{P}_{k|k-1} = \boldsymbol{\Phi}(t_{k+1}, t_k)\boldsymbol{P}_{k-1|k-1}\boldsymbol{\Phi}(t_{k+1}, t_k)^T + \boldsymbol{Q}(k) \qquad (4.36)$$

The first term corresponds to information diffusion while the second term is the contribution of process noise. A good process model makes an accurate prediction and looses very little information. This is reflected by the fact that the prediction covariance is small. However, a poor dynamic model makes inaccurate predictions, leading to a larger covariance.

After the prediction has been made, the estimate is determined through the update. This is an injection of new, current information into the filter. From Equation (4.35) it can be shown that for a given amount of sensor information, the updated covariance is minimized if the prediction covariance is minimized. Therefore, optimal performance is only achieved if the information in the prediction is maximized.

4.5 Model Selection

The analysis in the previous section shows that the dynamic model should be chosen to maximize the information in the prediction. Intuitively it must closely approximate the way that the true system behaves. The order of the true system is, however, generally high and the system may sometimes not be described by a finite dimension.

The true system takes account of all the effects, which act on the spacecraft. These include states, which are directly relevant to attitude determination (such as attitude and angular velocity), states, which are indirectly related (for example, changing atmospheric density) and states, which have only a very slight relevance (for example, vibration modes in the boom).

Even if the dynamic model were perfectly known and could be described with sufficiently few states that it could be implemented, there is an additional problem, known as the bias/variance tradeoff. As a model becomes more complex, it becomes a better description of the true system, and the bias becomes progressively smaller. However, a more complex model includes more states. Given that there is only a finite amount of noisy data, the result is that the information has to be spread between the states and the variance on the estimates of all of the states increase.

These problems mean that the core issue in designing an attitude estimator is to find a suitable balance between a detailed dynamic model and an accurate sensor suite. The guiding principle is that the dynamic model should be the least complex model (parsimonious (Ljung (1987))), which is capable of describing the most significant features of the true system .

4.5.1 Modeling Errors

As mentioned above most practical estimators cannot use a model which describes the true system precisely. Approximations must be made in order to achieve a computational efficient algorithm. This section analyze the problem of approximate system models in greater detail and the effects of modeling errors is quantified. The effect of an approximate system model in the covariance prediction context is first analyzed and next the effect of incorrect noise statistics is examined.

4.5.1.1   Covariance Prediction

As discussed in Section 4.3.1 modeling errors are often compensated for in the EKF by increasing the process noise, $\boldsymbol{Q}(t)$. The objective in the following is to set up a bound on the minimum value of the process noise that takes modeling errors into account.

For simplicity, we assume that the process noise is additive and that there is no control input. The true system then evolves according to the stochastic differential equation

$$d\boldsymbol{x}_T(t) = \boldsymbol{f}_T(\boldsymbol{x}_T(t))dt + d\boldsymbol{\beta}_T(t) \tag{4.37}$$

where $\boldsymbol{x}_T(t)$ is the state of the true system, $d\boldsymbol{\beta}_T(t)$ is the process noise, and $\boldsymbol{f}_T(\cdot)$ is the true system model.

Given the true state vector at time t_k, $\boldsymbol{x}_T(t_k)$. The true system may be of high order, and approximations are therefore made in the estimator design. It is assumed that there is a structural relationship between the states of the approximate system and the true system given by the projection of the true system state $\boldsymbol{x}_T(t_k)$ onto the approximate system state space

$$\bar{\boldsymbol{x}}(t_k) \triangleq \boldsymbol{g}(\boldsymbol{x}_T(t_k)) \tag{4.38}$$

where $\bar{\boldsymbol{x}}(t_k)$ is the projection of the true state onto the approximate state space. The projection into the approximate state space, $\bar{\boldsymbol{x}}(t_k)$ represents the true system, but in approximate state space. In the case of zero estimation error, $\bar{\boldsymbol{x}}(t_k)$ would be our estimate of the true state. The dimension of the approximate system state space may be smaller than the dimension of the true state space. In the analysis here, $\boldsymbol{g}(\cdot)$ need not be explicitly defined unless exact optimum results are required.

The actual prediction error of the approximate system at time t_k is then given by

$$\tilde{\boldsymbol{x}}(t_k) \triangleq \bar{\boldsymbol{x}}(t_k) - \hat{\boldsymbol{x}}_{k|k-1} \tag{4.39}$$

and the actual mean-squared error prediction error is thus given by

$$\bar{\boldsymbol{P}}_{k|k-1} = E\{\tilde{\boldsymbol{x}}(t_k)\tilde{\boldsymbol{x}}^T(t_k)|Z_{k-1}\} \tag{4.40}$$

To ensure consistency of the estimator, the process noise parameters $\boldsymbol{Q}$ must be selected such that

$$\boldsymbol{P}_{k|k-1} \geq \bar{\boldsymbol{P}}_{k|k-1} \tag{4.41}$$

which means that the predicted error estimate is larger than the actual error.

Based on Equation (4.37) the projection of the true system is governed by the stochastic differential equation

$$d\bar{\boldsymbol{x}}(t) = \boldsymbol{G}(t)\boldsymbol{f}_T(\boldsymbol{x}_T(t))dt + \boldsymbol{G}(t)d\boldsymbol{\beta}_T(t) \qquad (4.42)$$

where the $\boldsymbol{G}(t)$ and $\boldsymbol{G}(t)$ is the Jacobian of $\boldsymbol{g}(\cdot)$ with respect to $\boldsymbol{x}_T(t)$. The model $\boldsymbol{f}_T(\cdot)$ describe the evolution of the true system, and $d\boldsymbol{\beta}_T(t)$ is the true additive process noise.

The first term in Equation (4.42) describe the evolution of the true system state without noise, which is projected onto the approximate system space. It is assumed that this may also be written as the evolution of $\bar{\boldsymbol{x}}(t)$ using the approximate dynamics and an additive modeling error term, which is a function of the true state

$$d\bar{\boldsymbol{x}}(t) = \boldsymbol{f}(\bar{\boldsymbol{x}}(t))dt + \boldsymbol{G}(t)d\boldsymbol{\beta}_T(t) + \boldsymbol{\Gamma}(\boldsymbol{x}_T(t))dt \qquad (4.43)$$

where $\boldsymbol{\Gamma}(\boldsymbol{x}_T(t))$ is the modeling error, which describes the error committed by assuming the approximate dynamics

$$\boldsymbol{\Gamma}(\boldsymbol{x}_T(t))dt = \boldsymbol{G}(t)\boldsymbol{f}_T(\boldsymbol{x}_T(t))dt - \boldsymbol{f}(\bar{\boldsymbol{x}}(t))dt \qquad (4.44)$$

The estimate and error states are now substituted into Equation (4.43), which is then linearized about the estimated system state

$$\begin{aligned} d\bar{\boldsymbol{x}}(t) &= \boldsymbol{f}\left(\hat{\boldsymbol{x}}(t) + \tilde{\boldsymbol{x}}(t)\right)dt + \boldsymbol{G}(t)d\boldsymbol{\beta}_T(t) + \boldsymbol{\Gamma}(\boldsymbol{x}_T(t))dt \qquad (4.45) \\ &\simeq \boldsymbol{f}\left(\hat{\boldsymbol{x}}(t)\right)dt + \boldsymbol{F}(t)\tilde{\boldsymbol{x}}(t)dt + \boldsymbol{G}(t)d\boldsymbol{\beta}_T(t) + \boldsymbol{\Gamma}(\boldsymbol{x}_T(t))dt \end{aligned}$$

where $\boldsymbol{F}(t)$ is the Jacobian of the approximate dynamics evaluated at the state estimate $\hat{\boldsymbol{x}}(t)$. The evolution of the estimated state is controlled by

$$d\hat{\boldsymbol{x}}(t) = \boldsymbol{f}(\hat{\boldsymbol{x}}(t))dt$$

Subtracting the estimated dynamics from Equation (4.45) results in the following error dynamics

$$d\tilde{\boldsymbol{x}}(t) = \boldsymbol{F}(t)\tilde{\boldsymbol{x}}(t)dt + \boldsymbol{G}(t)d\boldsymbol{\beta}_T(t) + \boldsymbol{\Gamma}(\boldsymbol{x}_T(t))dt \qquad (4.46)$$

The first term in Equation (4.46) accounts for the propagation of estimation error whereas the second term describe the process noise. These two terms are

explicitly maintained by the Kalman filter. The third term is an additional error introduced by the approximate system modeling.

In order to arrive at a discrete covariance propagation, Equation (4.46) is integrated over the interval from t_k to t_{k+1}

$$\tilde{\boldsymbol{x}}(t_{k+1}) = \boldsymbol{\Phi}(t_{k+1}, t_k)\tilde{\boldsymbol{x}}(t_k) + \boldsymbol{v}_T(k+1) + \boldsymbol{\Gamma}_{k+1} \tag{4.47}$$

where $\boldsymbol{\Phi}(t_{k+1}, t_k)$ is the state transition matrix. The $\boldsymbol{v}_T(k+1)$ is the true discrete process noise projected onto the approximate space and given by

$$\boldsymbol{v}_T(k+1) = \int_{t_k}^{t_{k+1}} \boldsymbol{\Phi}(t_{k+1}, \tau)\boldsymbol{G}(\tau)d\boldsymbol{\beta}_T(\tau)$$

The $\boldsymbol{\Gamma}_{k+1}$ is the contribution from the modeling error and defined by

$$\boldsymbol{\Gamma}_{k+1} = \int_{t_k}^{t_{k+1}} \boldsymbol{\Phi}(t_{k+1}, \tau)\boldsymbol{\Gamma}(\boldsymbol{x}_T(\tau))d\tau$$

The prediction covariance in Equation (4.40) is now found by taking outer products and expectations of Equation (4.47)

$$\begin{aligned} \bar{\boldsymbol{P}}_{k+1|k} &= \boldsymbol{\Phi}(t_{k+1}, t_k)\bar{\boldsymbol{P}}_{k|k}\boldsymbol{\Phi}^T(t_{k+1}, t_k) + \boldsymbol{Q}_T(k) \\ &\quad + \boldsymbol{\Phi}(t_{k+1}, t_k)\boldsymbol{P}_{k|k}^{x\Gamma} + (\boldsymbol{P}_{k|k}^{x\Gamma})^T\boldsymbol{\Phi}^T(t_{k+1}, t_k) + \boldsymbol{P}_k^{\Gamma\Gamma} \end{aligned} \tag{4.48}$$

The first two terms are well known from the Kalman filter covariance prediction. The last three terms are cross correlation terms that are included as a consequence of modeling errors. The $\boldsymbol{P}_{k|k}^{x\Gamma}$ is the correlation between the error in the a posteriori state estimate and the modeling error introduced by predicting from t_k to t_{k+1}. The last covariance term is $\boldsymbol{P}_k^{\Gamma\Gamma}$, which is the mean squared value of the modeling error term. In case of a very inaccurate approximate model $\boldsymbol{P}_k^{\Gamma\Gamma}$ may not be finite and the process noise is thus unbounded.

The analysis above leads to the following condition on the selection of the process noise parameters

$$\begin{aligned} \boldsymbol{Q}(k) &\geq \boldsymbol{Q}_T(k) + \boldsymbol{\Phi}(t_{k+1}, t_k)\boldsymbol{P}_{k|k}^{x\Gamma} \\ &\quad + (\boldsymbol{P}_{k|k}^{x\Gamma})^T\boldsymbol{\Phi}^T(t_{k+1}, t_k) + \boldsymbol{P}_k^{\Gamma\Gamma} \quad \forall t_k \end{aligned} \tag{4.49}$$

This analysis has shown that using an approximate system model introduces a performance penalty. Modeling errors introduce discrepancies in the covariance prediction, which must be compensated for by increasing the process noise in order to ensure a consistent estimate. The minimum value of noise is given by Equation (4.49). In most practical systems the actual noise and the modeling error function are not known and the selection of $\boldsymbol{Q}(k)$ is not trivial.

4.5.1.2 Covariance Update

The observational update in the Kalman filter is based on the innovation, which represented in terms of the true state is given by

$$\boldsymbol{\nu}_k = \boldsymbol{h}_T(\boldsymbol{x}_T(t_k), t_k) + \boldsymbol{w}_T(k) - \boldsymbol{h}(\hat{\boldsymbol{x}}_{k|k-1}, t_k) \qquad (4.50)$$

Assuming that there are no structural errors in $\boldsymbol{h}(\cdot)$, the true observation is linearized about the estimated state

$$\boldsymbol{h}_T(\boldsymbol{x}_T(t_k), t_k) = \boldsymbol{h}(\hat{\boldsymbol{x}}_{k|k-1}, t_k) + \boldsymbol{H}_k \tilde{\boldsymbol{x}}_{k|k-1} \qquad (4.51)$$

where $\boldsymbol{H}_k$ is the Jacobian of $\boldsymbol{h}(\cdot)$ evaluated at $\hat{\boldsymbol{x}}_{k|k-1}$.

Substituting this result into Equation (4.50) and applying the Kalman observational update (Equation (4.23)) to the error state we get

$$\begin{aligned}
\tilde{\boldsymbol{x}}_{k|k} &= \boldsymbol{x}_T(t_k) - \hat{\boldsymbol{x}}_{k|k} \\
&= \boldsymbol{x}_T(t_k) - \left(\hat{\boldsymbol{x}}_{k|k-1} + \boldsymbol{K}_k \boldsymbol{\nu}_k\right) \\
&= \left(\boldsymbol{1} - \boldsymbol{K}_k \boldsymbol{H}_k\right) \tilde{\boldsymbol{x}}_{k|k-1} + \boldsymbol{K}_k \boldsymbol{w}_T(k) \qquad (4.52)
\end{aligned}$$

Taking outer products and expectations, the true mean squared error of the estimate is

$$\begin{aligned}
\bar{\boldsymbol{P}}_{k|k} = {}& \left(\boldsymbol{1} - \boldsymbol{K}_k \boldsymbol{H}_k\right) \bar{\boldsymbol{P}}_{k|k-1} \left(\boldsymbol{1} - \boldsymbol{K}_k \boldsymbol{H}_k\right)^T \\
& + \boldsymbol{K}_k \boldsymbol{R}_T(k) \boldsymbol{K}_k^T
\end{aligned} \qquad (4.53)$$

which is similar the Joseph form (Bucy and Joseph (1968)) of the normal Kalman filter covariance update. In the approximate filter knowledge about the true covariance $\bar{\boldsymbol{P}}_{k|k-1}$ or observation noise $\boldsymbol{R}_T(k)$ is not available, and the update is hence given by

$$\boldsymbol{P}_{k|k} = \left(\boldsymbol{1} - \boldsymbol{K}_k \boldsymbol{H}_k\right) \boldsymbol{P}_{k|k-1} \left(\boldsymbol{1} - \boldsymbol{K}_k \boldsymbol{H}_k\right)^T + \boldsymbol{K}_k \boldsymbol{R}(k) \boldsymbol{K}_k^T \quad \forall t_k \quad (4.54)$$

Subtracting Equation (4.54) from Equation (4.53) leads to

$$\begin{aligned}
\boldsymbol{P}_{k|k} - \bar{\boldsymbol{P}}_{k|k} = {}& \left(\boldsymbol{1} - \boldsymbol{K}_k \boldsymbol{H}_k\right) \left(\boldsymbol{P}_{k|k-1} - \bar{\boldsymbol{P}}_{k|k-1}\right) \left(\boldsymbol{1} - \boldsymbol{K}_k \boldsymbol{H}_k\right)^T \\
& + \boldsymbol{K}_k \left(\boldsymbol{R}(k) - \boldsymbol{R}_T(k)\right) \boldsymbol{K}_k^T
\end{aligned} \qquad (4.55)$$

and in order to ensure consistency we require that $\boldsymbol{P}_{k|k} - \bar{\boldsymbol{P}}_{k|k} \geq \boldsymbol{0}$. A sufficient condition to ensure that the difference is positive semi definite is (Jazwinski (1970))

$$\boldsymbol{P}_{k|k-1} - \bar{\boldsymbol{P}}_{k|k-1} \geq \boldsymbol{0} \quad \text{and} \quad \boldsymbol{R}(k) - \boldsymbol{R}_T(k) \geq \boldsymbol{0} \quad \forall t_k \qquad (4.56)$$

The two conditions state that both the covariance prediction and the observation noise statistics must be consistent. The modeling errors associated with the covariance prediction must be compensated for by increasing the process noise. A bound on the process noise was established (Equation (4.49)) but it was argued that in most practical systems the bound cannot be calculated. The second condition in Equation (4.56) states that the approximate systems observation noise must exceed the noise of the true system.

4.6   The Quaternion in the Kalman Filter

In Chapter 3 the use of quaternions to represent a rotation in $SO(3)$ was outlined.

The quaternion was chosen as the attitude representation on the Ørsted satellite. The main reasons being the nonsigularity of the representation, the easily enforced orthogonality (by preserving unit norm), which is important from an implementational point of view, and finally properties that make it ideal for controller design (see Wisniewski (1997)).

Before applying the EKF to the attitude estimation problem two problems must be addressed. Both are related to the quaternion state

– *Covariance Singularity.* The unit norm constraint on the quaternion leads to a constrained error vector, and the associated covariance matrix is therefore singular.

– *Quaternion unity.* The filter should preserve the unit norm of the attitude quaternion in order to maintain orthogonality in the rotation. The standard EKF update is based on unconstrained additive corrections, and the result is not an attitude quaternion as the quaternion has no group structure under addition.

In the following, alternative forms of the EKF are presented that are norm preserving within a linear approximation and numerical round-off, while avoiding the covariance singularity issue.

4.6.1   Covariance Singularity

As discussed previously, the Kalman filter is designed to minimize the trace of the error covariance. That is, suppose $\hat{\mathbf{q}}$ is some estimate of the quaternion, and $\mathbf{q}$ is the true attitude. The goal of the Kalman filter algorithms is then to minimize

the trace of the covariance matrix for the quaternion state, $\boldsymbol{P}_{qq}$, which is defined as a 4×4 matrix

$$\boldsymbol{P}_{qq} = E\{(\tilde{\boldsymbol{q}} - E\{\tilde{\boldsymbol{q}}\})\,(\tilde{\boldsymbol{q}} - E\{\tilde{\boldsymbol{q}}\})^T\} \tag{4.57}$$

where $\tilde{\boldsymbol{q}}$ is the difference between true and estimated attitude

$$\tilde{\boldsymbol{q}} \triangleq \mathbf{q} - \hat{\mathbf{q}} \tag{4.58}$$

Assuming that the true quaternion is in a small neighborhood of the estimated quaternion, Equation (4.58) may be rewritten using the exponential power series in terms of the rotation vector,

$$
\begin{aligned}
\tilde{\boldsymbol{q}} &= \left(1 + \frac{1}{2}\epsilon\boldsymbol{n} - \frac{1}{8}\epsilon^2 + \ldots \right) \hat{\mathbf{q}} - \hat{\mathbf{q}} \\
&= \left(\frac{1}{2}\epsilon\boldsymbol{n} - \frac{1}{8}\epsilon^2 + \ldots \right) \hat{\mathbf{q}}
\end{aligned}
\tag{4.59}
$$

and with the definition in Equation (3.18)

$$\tilde{\boldsymbol{q}} = \boldsymbol{\Xi}_{\hat{\mathbf{q}}} \begin{bmatrix} \frac{1}{2}\epsilon\boldsymbol{n} \\ 0 \end{bmatrix} + \mathcal{O}(\|\epsilon\boldsymbol{n}\|^2) \tag{4.60}$$

With $E\{\epsilon\boldsymbol{n}\} = \boldsymbol{0}$ the full quaternion covariance may to first order be approximated by

$$\boldsymbol{P}_{qq} \simeq \frac{1}{4}E\left(\boldsymbol{\Xi}_{\hat{\mathbf{q}}} \begin{bmatrix} \epsilon\boldsymbol{n} \\ 0 \end{bmatrix} \begin{bmatrix} \epsilon\boldsymbol{n}^T & 0 \end{bmatrix} \boldsymbol{\Xi}_{\hat{\mathbf{q}}}^T \right) \tag{4.61}$$

$$\simeq \frac{1}{4}\boldsymbol{\Xi}_{\hat{\mathbf{q}}} \begin{bmatrix} \boldsymbol{P}_{\epsilon\epsilon} & \boldsymbol{0} \\ \boldsymbol{0}^T & 0 \end{bmatrix} \boldsymbol{\Xi}_{\hat{\mathbf{q}}}^T \tag{4.62}$$

where $\boldsymbol{P}_{\epsilon\epsilon} = E\{\boldsymbol{\epsilon}\boldsymbol{\epsilon}^T\}$ is the attitude error covariance. It follows immediately that the 4×4 covariance matrix is singular. Preserving this singularity is numerically difficult and may lead to a inconsistent filter solutions and divergence. In order to preserve the singularity it hence necessary to take the normalization constraint into account explicitly, or reduce the problem to one of lower dimension (i.e. three).

The former approach is generally difficult as the operations performed in the standard EKF assume independent state variables and therefore do not preserve the unit norm. Several authors (Bar-Itzhack and Oshman (1985); Bar-Itzhack

et al. (1991)) have, however, performed numerical investigations and achieved good results by basically ignoring the constraint on the quaternion and using the standard EKF unconstrained update equations on all four quaternion components.

Lefferts *et al.* (1982) suggested deleting one of the quaternion components in the state error vector (the component with largest magnitude) in order to achieve a truncated covariance matrix. This approach maintains proper rank of the covariance matrix and quaternion unity, but the full state transition matrix still has to be computed each time.

Alternatively Lefferts *et al.* (1982) suggests a more efficient algorithm based on a body referenced quaternion correction. Defining the error quaternion as the correction that has to be composed with the estimated quaternion in order to get the true state the error state dimension may be reduced.

Using the exponential map from Equation (3.24) we may parameterize a neighborhood of $\hat{\mathbf{q}}$ by

$$
\begin{aligned}
\mathbf{q} &= \exp(\frac{1}{2}\theta\boldsymbol{n})\hat{\mathbf{q}} \\
&= \left(1 + \frac{1}{2}\epsilon\boldsymbol{n} - \frac{1}{8}\epsilon^2 + \dots \right)\hat{\mathbf{q}}
\end{aligned}
\tag{4.63}
$$

Assuming that the exponential correction in Equation (4.63) is small and truncating the series to first order we get

$$
\mathbf{q} \simeq \left(1 + \frac{1}{2}\epsilon\boldsymbol{n}\right)\hat{\mathbf{q}}
\tag{4.64}
$$

The estimated quaternion $\hat{\mathbf{q}}$ represents the rotation from the reference frame to the estimated body frame. The correction in Equation (4.64) then represents a rotation from the estimated to the true body frame. This is in fact equivalent to the body referenced correction described in Lefferts *et al.* (1982).

The truncated series corresponds to a quaternion with unit real part and three free variables. The basic idea is now only to estimate the three free variables, which are aggregated into a 3 vector such that $\Delta\boldsymbol{q} = \frac{1}{2}\epsilon\boldsymbol{n}$. The error state to be estimated is then given by

$$
\widehat{\Delta\boldsymbol{x}}_{k|k} = \begin{bmatrix} \widehat{\Delta\boldsymbol{q}}_{k|k} \\ \widehat{\Delta\boldsymbol{\xi}}_{k|k} \end{bmatrix}
\tag{4.65}
$$

One independent parameter has been removed from the error state. If $\boldsymbol{\xi}_k$ has dimension n, then the state error vector has dimension $(n+3)$, whereas the state

vector has dimension $(n + 4)$. The reduced representation preserves proper rank of the reduced covariance matrix while simplifying the computation.

4.6.2 Quaternion Unity

The problem of maintaining orthogonality (unit norm) of the filter attitude solution is part of all numerical attitude estimation algorithms due to round off. In the Kalman filter the problem is, that each time a new estimate is formed, by adjoining new measurements, the constraint on the quaternion must be enforced in order to stay on the quaternion 3-sphere. In Bar-Itzhack *et al.* (1991) several quaternion normalization algorithms were compared, and it was found that normalization improved filter convergence and accuracy.

With the reduced error state, the EKF full state update becomes

$$\hat{\mathbf{q}}_{k|k} = \begin{bmatrix} \widehat{\Delta \boldsymbol{q}}_{k|k} \\ 1 \end{bmatrix} \hat{\mathbf{q}}_{k|k-1} \tag{4.66}$$

which is equivalent to a traditional additive update given by

$$\hat{\mathbf{q}}_{k|k} = (1 + \widehat{\Delta \boldsymbol{q}}_{k|k}) \hat{\mathbf{q}}_{k|k-1} \tag{4.67}$$

$$= \hat{\mathbf{q}}_{k|k-1} + \begin{bmatrix} \widehat{\Delta \boldsymbol{q}}_{k|k} \\ 0 \end{bmatrix} \hat{\mathbf{q}}_{k|k-1} \tag{4.68}$$

The error state thus represents a correction in the body frame, and not a general correction to $\hat{\mathbf{q}}_{k|k-1}$ as would be the case in a traditional Kalman filter.

The multiplicative form in Equation (4.66) has the advantage that the unit norm of the correction easily is enforced by using the following altered update rule

$$\hat{\mathbf{q}}_{k|k} = \begin{bmatrix} \widehat{\Delta \boldsymbol{q}}_{k|k} \\ \sqrt{1 - \|\widehat{\Delta \boldsymbol{q}}_{k|k}\|^2} \end{bmatrix} \hat{\mathbf{q}}_{k|k-1} \tag{4.69}$$

and the unit norm of the a posteriori estimate is thus preserved in the update. This basically corresponds to estimating only the projection of the quaternion into coordinate axes in $\mathbb{R}^3$ and then using the constraint to calculate the remaining coordinate.

The error covariance update was adjusted to reflect the normalization. A first order linearization of Equation (4.69) around the estimated error state was

applied and a correction of the estimated covariance performed. The resulting covariance was then truncated to a 3×3 matrix and used in the filter prediction. As there was no significant change in the estimated covariance or the filter performance, it was decided to avoid this additional step. One may argue that the assumptions made in the linearization of the covariance prediction will prevent us from benefiting from a more accurate covariance update.

4.7   Quaternion Vector Filter

Based on the quaternion error representation discussed in Section 4.6 this section presents the background for the algorithms developed for implementation in the on-board software for the Ørsted satellite. Details of the implementation and development are left for Chapter 5.

4.7.1   Filter State

The three-dimensional quaternion error state and the update rule in Equation (4.69) are the basis for the attitude representation used in the quaternion filter. Besides the quaternion, the filter state also include the angular velocity of the spacecraft relative to the inertial coordinate system. The angular velocity is required by the controller but also enables modeling of the dynamics.

The angular velocity update is define by simple addition

$$\hat{\boldsymbol{\omega}}_{k|k} = \hat{\boldsymbol{\omega}}_{k|k-1} + \widehat{\Delta\boldsymbol{\omega}}_{k|k} \tag{4.70}$$

The perturbation and full state vectors are therefore given by

$$\Delta\boldsymbol{x}_k = \begin{bmatrix} \Delta\boldsymbol{q}_k \\ \Delta\boldsymbol{\omega}_k \end{bmatrix} \quad \text{and} \quad \boldsymbol{x}_k = \begin{bmatrix} \boldsymbol{q}_k \\ \boldsymbol{\omega}_k \end{bmatrix} \tag{4.71}$$

The state vector $\Delta\boldsymbol{x}_k$ describe perturbations to the nominal state whereas the $\boldsymbol{x}_k$ is the full state. The full state is required to represent the time evolution of the system and it is the state used in the controller feedback. The perturbation state is only an internal estimator state, which is used in the filter update and covariance equations. The state vector defined here is sufficient for the discussion in this chapter, but augmented state vectors will be treated in Chapter 5 and 7. In the Ørsted case, the quaternion state estimate must represent a rotation from the local orbit frame (LVLH) to the body frame (SCB), whereas the desired representation of the angular velocity is relative to the inertial frame (ECI). The Freja attitude is defined relative to ECI.

4.7.2 Filter Propagation

The propagation of the full filter state between measurement updates uses the kinematic and dynamic relations defined in Equations (3.30) and (3.37), which may be solved using numerical integration.

Spacecraft dynamic models are inherently uncertain and it may be argued that replacing the dynamic model by a stochastic process model would be a better approach. For satellites like Ørsted, the dominating torque input is due to gravity gradient, which is well modeled if the moments of inertia of the satellite are known. A dynamic model has hence been included in this presentation. In Chapter 5 the issue will be discussed in more detail.

The propagation of the error covariance requires a linearization of the error state kinematic and dynamic about a nominal (the a posteriori) state estimate, which in the following is denoted by a bar.

Linearized Kinematics   With the definition of the quaternion correction from Equation (4.66) the deviation from the nominal state $\bar{\mathbf{q}}(t)$ may be written as

$$\Delta\mathbf{q}(t) = \mathbf{q}(t)\bar{\mathbf{q}}(t)^* \tag{4.72}$$

By representing the angular velocity in terms of a quaternion with zero scalar part the dynamics in Equation (3.30) may be rewritten in quaternion form. Applying the chain rule, the following differential equation describes how the quaternion error evolve over time

$$\frac{d}{dt}\Delta\mathbf{q}(t) = \frac{1}{2}\omega(t)\mathbf{q}(t)\bar{\mathbf{q}}(t)^* + \mathbf{q}(t)\frac{1}{2}\left(\bar{\omega}(t)\bar{\mathbf{q}}(t)\right)^* \tag{4.73}$$

$$= \frac{1}{2}\left(\bar{\omega}(t)\Delta\mathbf{q}(t) - \Delta\mathbf{q}(t)\bar{\omega}(t)\right) + \frac{1}{2}\Delta\omega(t)\Delta\mathbf{q}(t) \tag{4.74}$$

Neglecting second order terms results in the linearized kinematic equation expressed in the quaternion error

$$\frac{d}{dt}\Delta\boldsymbol{q}(t) = -\bar{\boldsymbol{\omega}}(t) \times \Delta\boldsymbol{q}(t) + \frac{1}{2}\Delta\boldsymbol{\omega}(t) \quad \text{and} \quad \frac{d}{dt}\Delta q(t) = 0 \tag{4.75}$$

There is one final remark to Equation (4.75). The angular velocity estimated by the filter is relative to the inertial frame, whereas the angular velocity in Equation (4.75) necessarily is relative to the local orbit frame (LVLH) in the Ørsted case. The term $\bar{\boldsymbol{\omega}}(t)$ therefore has to be interpreted as the nominal angular velocity relative to LVLH. Using $\bar{\boldsymbol{\omega}}_{bo}$ as the body referenced angular velocity relative

to LVLH, $\boldsymbol{\omega}_{bi}$ the angular velocity relative to the inertial frame, and $\bar{\boldsymbol{\omega}}_{oi}$ as angular velocity of the LVLH frame relative to inertial frame, we get

$$\bar{\boldsymbol{\omega}}_{bo}(t) = \bar{\boldsymbol{\omega}}_{bi}(t) - \boldsymbol{A}(\bar{\mathbf{q}})\bar{\boldsymbol{\omega}}_{oi} \tag{4.76}$$

The angular velocity $\bar{\boldsymbol{\omega}}_{oi}$ is near constant for orbits close to circular. The influence from $\Delta\boldsymbol{\omega}(t)$ is modified according to

$$\Delta\boldsymbol{\omega}(t) = \Delta\boldsymbol{\omega}_{bi}(t) - 2[\bar{\boldsymbol{\omega}}_{oi}\times]\Delta\boldsymbol{q} \tag{4.77}$$

where $\Delta\boldsymbol{\omega}_{bi}(t)$ is the velocity correction estimated by the filter and having used that $\boldsymbol{A}(\Delta\boldsymbol{q}) = (\mathbf{1} - 2[\Delta\boldsymbol{q}\times])$ to first order. When substituting Equations (4.76) and (4.77) into the expression in Equation (4.75) the effect of changing the reference frame cancels out. The results is thus the linearized dynamics in Equation (4.75).

Linearized Dynamics   First we linearize the control input torque. The linearized version of the input torque given by Equation (3.38) is

$$\Delta\boldsymbol{n}_{ctrl}(t) = 2[\boldsymbol{m}(t)\times][\bar{\boldsymbol{b}}(t)\times]\Delta\boldsymbol{q} \tag{4.78}$$

where $\bar{\boldsymbol{b}}(t) = \boldsymbol{A}(\bar{\mathbf{q}}(t))\boldsymbol{b}(t)$ is the nominal geomagnetic field in the body frame.

The gravity gradient depend explicitly on the attitude of the spacecraft and the linearization is hence carried about the nominal quaternion. From Equation (3.39) we get

$$\boldsymbol{n}_{gg}(t) = \frac{3\mu}{r^3}\left(\boldsymbol{A}(\Delta\mathbf{q}(t))\,\bar{\boldsymbol{\eta}}(t)\times \boldsymbol{I}\,\boldsymbol{A}(\Delta\mathbf{q}(t))\,\bar{\boldsymbol{\eta}}(t)\right) \tag{4.79}$$

where $\bar{\boldsymbol{\eta}}$ is the nominal zenith vector in the body frame. Ignoring second order terms, the linearized gravity gradient is given by

$$\Delta\boldsymbol{n}_{gg}(t) \quad = \quad \frac{6\mu}{r^3}\left([\bar{\boldsymbol{\eta}}(t)\times]\boldsymbol{I}[\bar{\boldsymbol{\eta}}(t)\times] - [\bar{\boldsymbol{\eta}}(t)\times][\boldsymbol{I}\bar{\boldsymbol{\eta}}(t)\times]\right)\Delta\boldsymbol{q} \tag{4.80}$$

where it was assumed that the r^3 is approximately constant. i.e. a close to circular orbit.

The remaining part of the dynamics are found using a standard first order Taylor series and the combined dynamics are therefore

$$\frac{d}{dt}\Delta\boldsymbol{\omega}(t) \quad = \quad \boldsymbol{I}^{-1}\left([\boldsymbol{I}\bar{\boldsymbol{\omega}}(t)\times] - \bar{\boldsymbol{\omega}}(t)\times\boldsymbol{I}\right)\Delta\boldsymbol{\omega}(t) \tag{4.81}$$

$$+\boldsymbol{I}^{-1}\left(\Delta\boldsymbol{n}_{ctrol}(t) + \Delta\boldsymbol{n}_{gg}(t)\right)$$

Combined Linear Model   The combined linearized model is now a 6th order system and may be described by a matrix of sensitivities due to attitude and rate perturbations

$$\frac{d}{dt}\Delta\boldsymbol{x}(t) = \boldsymbol{F}(t)\Delta\boldsymbol{x}(t) \tag{4.82}$$

where

$$\boldsymbol{F}(t) = \begin{bmatrix} -[\bar{\boldsymbol{\omega}}(t)\times] & \frac{1}{2}\mathbf{1} \\ 2\boldsymbol{I}^{-1}\left(k\boldsymbol{F}_g(t) + [\boldsymbol{m}(t)\times][\bar{\boldsymbol{b}}(t)\times]\right) & \boldsymbol{I}^{-1}\boldsymbol{F}_e(t) \end{bmatrix} \tag{4.83}$$

where $k = 3\mu/r^3$ and $\boldsymbol{F}_g(t)$ represents the coupling in Equation (4.80) due to gravity gradient. The $\boldsymbol{F}_e(t)$ matrix represents the gyroscopic coupling from Equation (4.81).

Given body axes aligned with the principal axes (i.e. zero products of inertia the matrices) the matrices $\boldsymbol{F}_g(t)$ and $\boldsymbol{F}_e(t)$ are given by

$$\boldsymbol{F}_g(t) = \begin{bmatrix} (\bar{\eta}_2^2 - \bar{\eta}_3^2)(I_{22} - I_{33}) & -\bar{\eta}_1\bar{\eta}_2(I_{22} - I_{33}) & \bar{\eta}_2\bar{\eta}_1(I_{22} - I_{33}) \\ \bar{\eta}_1\bar{\eta}_2(I_{33} - I_{11}) & (\bar{\eta}_3^2 - \bar{\eta}_1^2)(I_{33} - I_{11}) & -\bar{\eta}_3\bar{\eta}_2(I_{33} - I_{11}) \\ -\bar{\eta}_1\bar{\eta}_3(I_{11} - I_{22}) & -\bar{\eta}_2\bar{\eta}_3(I_{11} - I_{22}) & (\bar{\eta}_1^2 - \bar{\eta}_2^2)(I_{11} - I_{22}) \end{bmatrix}$$

and

$$\boldsymbol{F}_e(t) = \begin{bmatrix} 0 & \bar{\omega}_3(I_{22} - I_{33}) & \bar{\omega}_2(I_{22} - I_{33}) \\ \bar{\omega}_3(I_{33} - I_{11}) & 0 & \bar{\omega}_1(I_{33} - I_{11}) \\ \bar{\omega}_2(I_{11} - I_{22}) & \bar{\omega}_1(I_{11} - I_{22}) & 0 \end{bmatrix}$$

where I_{11}, I_{22}, and I_{33} are principal moments of inertia. The time index is left out for simplicity.

Covariance Propagation   The covariance propagation may now be carried out by solving the Riccati equation

$$\frac{d}{dt}\boldsymbol{P}(t) = \boldsymbol{F}(t)\boldsymbol{P}(t) + \boldsymbol{P}(t)\boldsymbol{F}^T(t) + \boldsymbol{Q}(t) \tag{4.84}$$

Similar to the dynamics and kinematics propagation, the error covariance, $\boldsymbol{P}_{k|k-1}$ may be solved using numerical integration. For simple numerical implementation the discrete time equivalent of Equation (4.84) is most often used. The covariance prediction is then given by (Jazwinski (1970))

$$\boldsymbol{P}_{k|k-1} = \boldsymbol{\Phi}(t_k, t_{k-1})\boldsymbol{P}_{k|k}\boldsymbol{\Phi}^T(t_k, t_{k-1}) + \boldsymbol{Q}_{k-1} \tag{4.85}$$

where $\boldsymbol{\Phi}(t_k, t_{k-1})$ is the state transition matrix, and $\boldsymbol{Q}(k)$ is the discrete state noise covariance. The $\boldsymbol{\Phi}(t_k, t_{k-1})$ matrix is found based on the Jacobian, $\boldsymbol{F}(t)$ found above. The discrete noise in Equation (4.85) is defined by

$$\boldsymbol{Q}(k-1) = \int_{t_{k-1}}^{t_k} \boldsymbol{\Phi}(t_k, \tau)\boldsymbol{Q}(\tau)\boldsymbol{\Phi}^T(t_k, \tau)d\tau \tag{4.86}$$

4.7.3 Filter Update

In order to process the measurements in the filter, a measurement model, and a linearization about the a priori state is required.

Measurement Processing   The physical measurements are the magnetic field vector projected onto the three sensor axes. In the case of magnetometer measurements the model maintained by the filter is based on a reference field model. This takes the form

$$\begin{aligned} \boldsymbol{z}_k &= \boldsymbol{h}(\boldsymbol{x}_k, t_k) + \boldsymbol{w}_k \\ &= \boldsymbol{A}(\mathbf{q}(t_k))\boldsymbol{b}_k + \boldsymbol{w}_k \end{aligned} \tag{4.87}$$

where $\boldsymbol{A}(\mathbf{q}(t_k))$ is the rotation from the reference frame to the sensor frame, and $\boldsymbol{b}_k$ is the true local magnetic field in the reference frame. The noise term $\boldsymbol{w}_k$ accounts for effects due to e.g. thermal noise in sensor components and sampling resolution. The sensor noise is assumed to be a zero mean Gaussian discrete process, with covariance $\boldsymbol{R}_m(k)$.

The processing of the measurement observation model, requires the use of a reference field model vector generated by a magnetic field model. The reference vector is corrupted by noise due to model errors and errors in the position estimates used to derive the model vectors. To compensate for these errors additional noise is added to the noise model. The model noise is modeled as a zero mean white Gaussian sequence with covariance $\boldsymbol{R}_b(k)$ which is uncorrelated with the sensor noise. The total noise model used in relation to Equation (4.87) is hence given by

$$\boldsymbol{R}(k) = \boldsymbol{R}_m(k) + \boldsymbol{A}(\hat{\mathbf{q}}_{k|k-1})\boldsymbol{R}_b(k)\boldsymbol{A}(\hat{\mathbf{q}}_{k|k-1})^T \tag{4.88}$$

In order to process the noise models, the nonlinear measurement in Equation (4.87) is next linearized about the a priori state estimate. Using $\bar{\boldsymbol{b}}_k =$

$A(\hat{\mathbf{q}}_{k|k-1})\boldsymbol{b}_k$ as the nominal magnetic field in the body frame. The result is a measurement equation given by

$$\hat{\boldsymbol{z}}_{k|k-1} \quad = \quad \boldsymbol{H}(\hat{\boldsymbol{x}}_{k|k-1}, t_k)\widehat{\Delta\boldsymbol{x}}_{k|k-1} \tag{4.89}$$

$$= \quad \begin{bmatrix} 2[\bar{\boldsymbol{b}}_k \times] & \boldsymbol{0} \end{bmatrix} \widehat{\Delta\boldsymbol{x}}_{k|k-1} \tag{4.90}$$

The matrix $\boldsymbol{H}(\cdot)$ has only rank two, which reflects the fact that the measurement of one unit vector contains no information about rotation around that vector.

Update   Given the previous discussion, we may now turn back to the filter update stage. The estimator gain matrix is now calculated following Equation (4.22)

$$\boldsymbol{K}_k = \boldsymbol{P}_{k|k-1}\boldsymbol{H}_k^T \left(\boldsymbol{H}_k \boldsymbol{P}_{k|k-1} \boldsymbol{H}_k^T + \boldsymbol{R}(k) \right)^{-1}$$

Direct update using this result is known to be numerically unstable and numerous representations exist that overcome this problem. This issue is addressed in more detail in Chapter 6.

Finally the measurement updated estimate of the perturbation state is

$$\widehat{\Delta\boldsymbol{x}}_{k|k} = \boldsymbol{K}_k \left(\boldsymbol{z}_k - \boldsymbol{h}(\hat{\boldsymbol{x}}_{k|k-1}, t_k) \right) \tag{4.91}$$

This is used to update the full state estimate as described in the beginning of this section. After incorporating $\Delta\boldsymbol{x}_{k|k}$ into the current attitude and rate estimates, the error states are re-initialized to zero.

In summary the Kalman filter algorithm is given by Table 4.1.

4.8   Summary

This chapter has addressed problems related to the issue of estimation of spacecraft attitude using extended Kalman filtering. In Section 4.1 the basic assumptions behind a discussion of the Kalman filter were outlined. Section 4.2 separated the Kalman filter into a prediction and an update step and the equations for the linear Kalman filter were presented.

In Section 4.3 the extension of the Kalman filtering to nonlinear problems was explored. This lead to the extended Kalman filter (EKF). A number of problems associated with the use of the EKF were discussed, including inconsistency. Section 4.4 presented a formulation of the Kalman filter in terms of information

Table 4.1: *Summary of Kalman filter. Linearizations and transition matrix are defined in the text above.*

State prediction	$$\frac{d}{dt}\hat{\boldsymbol{x}}(t) = \boldsymbol{f}\left(\hat{\boldsymbol{x}}(t), \boldsymbol{u}(t), t\right)$$
Covariance prediction	$$\boldsymbol{P}_{k|k-1} = \boldsymbol{\Phi}(t_k, t_{k-1})\boldsymbol{P}_{k|k}\boldsymbol{\Phi}^T(t_k, t_{k-1}) + \boldsymbol{Q}_{k-1}$$

State update	$$\widehat{\Delta\boldsymbol{x}}_{k|k} = \boldsymbol{K}_k\left(\boldsymbol{z}_k - \boldsymbol{h}(\hat{\boldsymbol{x}}_{k|k-1}, t_k)\right)$$
	$$\hat{\mathbf{q}}_{k|k} = \left[\frac{\widehat{\Delta\boldsymbol{q}}_{k|k}}{\sqrt{1 - \|\widehat{\Delta\boldsymbol{q}}_{k|k}\|^2}}\right]\hat{\mathbf{q}}_{k|k-1}$$
	$$\hat{\boldsymbol{\omega}}_{k|k} = \hat{\boldsymbol{\omega}}_{k|k-1} + \widehat{\Delta\boldsymbol{\omega}}_{k|k}$$
Covariance update	$$\boldsymbol{P}_{k|k} = \boldsymbol{P}_{k|k-1} - \boldsymbol{K}_k\boldsymbol{H}_k\boldsymbol{P}_{k|k-1}$$
Kalman gain	$$\boldsymbol{K}_k = \boldsymbol{P}_{k|k-1}\boldsymbol{H}_k^T\left(\boldsymbol{H}_k\boldsymbol{P}_{k|k-1}\boldsymbol{H}_k^T + \boldsymbol{R}(k)\right)^{-1}$$

matrices which demonstrates the temporal fusion of data. The role of the process model was examined. It was shown that the process model allow data from previous measurements to be incorporated into the current estimate, thereby allow temporal fusion of data. It was shown how predictions and observations are treated equally in the Kalman filter, and it was argued that an accurate process model may supplement sensors. In this way local observability problems may be avoided.

In practical implementations the prediction model, always represent a compromise between accuracy and complexity. Section 4.5.1 thus analyzed the effects of approximate models. A new simple description of the errors committed by approximation was introduced, and the influence on the noise statistics was quantified.

In Section 4.6 the problems of preserving normalization of the quaternion and

covariance singularity were addressed. It was argued that a conventional EKF approach is problematic due to a covariance singularity. The covariance singularity was demonstrated using the exponential series in the quaternion, which was truncated to first order. The first order approximation was finally used in Section 4.7, which presented a filter, which avoids the covariance singularity by using a three dimensional first order approximation to the correction quaternion calculated by the Kalman filter. The correction represents a rotation in the body frame.

Chapter 5

Ørsted Attitude Estimation

The original motivation for the work presented in this thesis was given by the attitude control system (ACS) for the Ørsted small satellite. The Ørsted mission requires Earth-pointing three-axis control, which in turn demands that the spacecraft attitude determination system (ADS) provides accurate attitude of the vehicle. This chapter presents the design and evaluation of the ADS developed for Ørsted. Results from the on-board implementation are discussed in Chapter 6. The main results in this chapter have been published in Bak (1996), Bak *et al.* (1996*a*), and Bak (1998*a*).

The chapter is divided into six sections plus conclusions. Section 5.1 presents the motivation for addressing the Ørsted problem and describes the underlying problems. Section 5.2 addresses the requirements to accuracy and fault tolerance. The implications for estimator design are discussed. Section 5.3 takes the first step in the development of the ADS. A simulation model is described that simulate the motion of the satellite as accurately as possible over a set of test cases. Section 5.4 discusses the estimator design, and two different process models are presented. Section 5.5 presents the results for a set of scenarios ranging from a nominal pointing to a fault situation. Finally, Section 5.6 presents an error budget which combines the effects of a number of systematic errors into an estimate of the predicted performance of the magnetometer based ADS.

5.1 Motivation and Related Work

Low-cost launch opportunities and technological advancements make small satellites interesting for doing space experiments within an affordable cost and

schedule envelope.

Few if any small satellite missions to date have been able to demonstrate the ability to perform high profile science missions. One of the main obstacles is the lack of proper attitude determination and control. Free tumbling spacecraft have only few useful mission capabilities. Passive methods such as gravity gradient, solar and aerodynamic stabilization have successfully been used on small satellite missions but do not provide the needed accuracy to facilitate mainstream scientific missions.

The Danish Ørsted small satellite mission is the first Danish attempt to built a satellite. The plan is to conduct relevant science within a limited budget while including basic services such as attitude control. In terms of functionality and science scope the objectives are high. In order to minimize ground control the attitude control subsystem must be inherently fault tolerant and support a number of mission modes. On the other hand a simple ACS design is desired in order to keep within a low budget and limited computational resources.

For simplicity the attitude estimation is based on the available science measurement package. Traditional gyro packages are omitted relying on increased on-board processing capability for integration of the equations of motion.

5.1.1 Introduction to the Ørsted Satellite

The Ørsted satellite was launched by a Delta II launch vehicle February 23, 1999 from Vandenberg Airforce base in California, USA. The main science mission is related to a precise global mapping of the Earth's magnetic field. Science operation is planned for a period of 14 months.

The science measurements will be used to improve the existing models of the Earth's magnetic field and to determine the changes of the field. Equivalent measurements have been made by the American MAGSAT satellite (1979-80). With the new data from Ørsted it will be possible for the first time ever to obtain a global survey of the changes of the field.

Variations of the strong field from inside the Earth are included in the studies. Also the weaker, rapidly varying, field resulting from the interaction between the ion/particle streams from the Sun (the solar wind) and the Earth's magnetosphere are studied. The transfer of energy from the solar wind to the magnetosphere and further down to the lower layers of the atmosphere will also be studied. All of these studies will benefit not only from the magnetic field measurements but also from the measurements of the flow of energetic particles around the satellite.

The Ørsted budget for development and operation was 120 million Danish
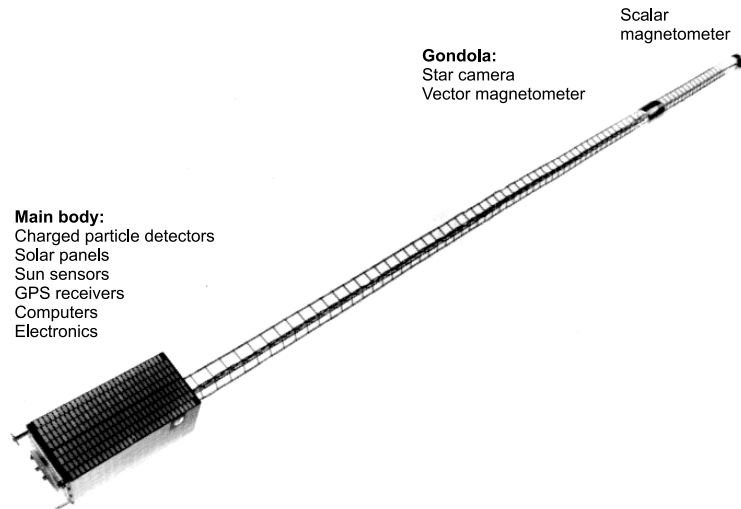
Figure 5.1: *The Ørsted satellite. The main body is 600×450×300 mm and the total weight is 62 kg. Instruments are placed on the 8 meter boom. The vector magnetometer is placed in the gondola.*

Kroner or equivalently 18 million USD (this amount exceeds typical small satellite projects because it includes a relatively large amount of basic research). The fundamental operational parameters of Ørsted are summarized in Table 5.1.

The ACS is an integrated part of the satellite bus and implemented in the general command and data handling of the satellite. Two 16 MHz 80C186 processors provide on-board data handling with partial redundancy. The ACS software is running on one of the computers and is not redundant on the other one. Attitude control actuation is provided by three perpendicular two-redundant electro-magnetic coils, called magnetorquers.

A science package consisting of a star camera and a magnetometer are mounted on an instrument boom six meters from the satellite main body. The boom is deployed after an initial detumbling phase and the three-axis attitude is maintained with the boom zenith pointing. For a more detailed discussion of the mission phases see Bak *et al.* (1996*a*).

Table 5.1: *Operational parameters of the Ørsted satellite. Ørsted was launched on February 23, 1999.*

Orbit	Inclination	96.62 deg.
	Ascending node	14:39 Local time (drifting towards noon)
	Argument of perigee	224 deg.
	Apoapsis	850 km
	Periapsis	600 km
	Nodal period	99.15 minutes
	Expected lifetime	425 days
Attitude	Stabilization	Active three-axis and gravity gradient stabilized
	Control	Magnetic
	Orientation	Aligned with local vertical, yaw reference following Sun
Mass	Total	62 kg
	Payload	13 kg (including booms and antennas)
Telemetry	Downlink stations	Copenhagen and Aalborg, Denmark
	Transmitter	S-band transmitter (2.2 GHz) and receiver (2.0 GHz)
	Downlink rate	4 or 256 kbits/sec
	Downlink time/orbit	6 minutes (average)
Power	Nominal Power	31 W provided by GaAs solar panels
	Payload usage	12 W (20.5 W with TurboRouge GPS)
Computer	Main computer	Two 80C186/16 Mhz CPUs
	On-board storage	16 Mbyte, 13 hours of science of measurements
	Software	Ada developed based on formal methods

5.1.2 Measurement Package

The attitude determination is based on the measurements from the science payload as summarized in Table 5.2.

The Ørsted science instruments are located on platforms separated from the satellite main body as seen in Figure 5.1 in order to minimize the electrical interference. The magnetometer, the star camera, and the Sun sensor are used directly in the attitude determination and are addressed in more detail below. The GPS receiver provides position fixes, which are used indirectly in updating an on-board orbit propagation model.

The Vector Magnetometer The precision magnetometer for Earth's field mapping on-board Ørsted is the Compact Spherical Coil (CSC) vector magnetometer developed at the Technical University of Denmark. The instrument consists of the spherical tri-axial sensor unit and an electronics box containing

Table 5.2: *Overview of the Ørsted Instruments package.*

Instrument	Characteristics
Vector magnetometer	Compact Spherical Coil (CSC) three-axis fluxgate type magnetometer. Stable within 0.5 nT over time spans of several days. The instrument is build at the Technical University of Denmark
Star camera	CCD based star sensor. Provides attitude with 2 arc-sec pointing accuracy and 20 arc-sec accuracy about the boresight. The sensor is build at the Technical University of Denmark.
Overhauser magnetometer	Measure the strength of the magnetic field. Accuracy < 5nT. Used for calibration of the vector magnetometer. The instrument is supplied by the French Space Agency, CNES.
Particle sensors	Measure the flux of fast electrons (0.03-1 MeV), protons (0.2-30 MeV), and alpha-particles (1-100 MeV) around the satellite. The instrument is build at the Danish Meteorological Institute.
GPS	Turbo-Rogue and Trimble GPS receivers provide position information. The Turbo-Rouge is also used scientifically to investigate the atmospheric pressure, temperature, and humidity. The Turbo-Rouge receiver is build by the Jet Propulsion Laboratory and supplied by NASA
Sun sensors	Two sets of coarse Sun-sensors provide information about the Sun direction. The sensors are build at Aalborg University.

the sensor excitation driver, the three analog magnetometer channels, sigma-delta ADC's and interface. The magnetometer has three sets of orthogonal coils, which are used to compensate the ambient field to be measured. A set of three orthogonal null field indicators sense the deviation from zero field inside the sphere. The feedback currents to the magnetometer field cancelling coils are measured with 18 bit resolution ADC's and represents the field components. The magnetometer has a linear range of $\pm$ 65.536 nT (Nielsen *et al.* (1990)). Magnetometer bias and misalignments are determined by calibration prior to launch (and also through in-flight calibration) and available for on-board processing. The predicted peak-to-peak noise is less than 0.5 nT.

The Star Camera   The star camera (the Ørsted Advanced Stellar Compass) is a low weight, low power CCD detector unit developed at the Technical University of Denmark (Liebe (1995), Jørgensen (1995)). The instrument consists of a

camera head unit with a commercial CCD detector, and a data processing unit equipped with an Intel 486 type processor. The processing unit contains two large star databases, which enable autonomous acquisition and tracking mode attitude determination. In tracking mode, the tracking is based on a spherical least squares fit between two consecutive images. The acquisition is based on pattern recognition of the stars in the field of view. Typically 65 stars in the field of view are used for tracking. The camera field of view is 16×22 deg. and the CCD has 752×582 pixels. The attitude is updated at approximately 0.8 Hz and give the attitude relative to the ECI inertial frame. The camera's limit of operation is an angular rate of 10 deg./minute. Sun/Moon/Earth exposure may also cause temporary loss of attitude information. The instrument is mounted on the boom next to the magnetometer in order to provide the highest accuracy in the magnetometer attitude relative to the star camera. The predicted accuracy is 2 arcsec (1 sigma) perpendicular to the boresight and 20 arcsec (1 sigma) about the boresight (Eisenman *et al.* (1996))

The Wide-Angle Sun Sensor   A low accuracy Sun sensor provides Sun position sensing over a near 4π steradian operating range. The instrument is build at Aalborg University. The Sun sensors are comprised of eight independent GaAs cells, each operated in short circuit mode. The cells are mounted on the main structure in two three-axis assemblies and two single axis assemblies. The mounting of the sensors overcomes the field of view limitations otherwise imposed by separation mechanism and antennas. Each of the eight Sun sensor heads has two-redundant cells and termistors for thermal compensation. Field of view limitations and Earth albedo make the Sun sensors fairly nonlinear and the expected accuracy of the calibrated sensors is about 4 deg. (1 sigma) about all three axes.

5.1.3   The Attitude Control Subsystem

The Ørsted attitude control is implemented using magnetorquers as the sole control devices. The attitude is estimated on-board using the available science sensor suite. The nominal pointing requirements are derived from power optimization as well as the operational cone and rate sensitivity of the star camera.

The control objectives of the ACS are related to

– *Detumbling.* Initially, after release from the launcher the satellite will experience a tumbling motion. The objective of the ACS is to reduce the

kinetic energy. The satellite should be aligned with the local magnetic field, ready for boom deployment.

– *Three-axis stabilization.* After detumbling the boom is deployed and the satellite should be three axes stabilized during the remainder of the mission. The reference attitude is aligned with local vertical with boom zenith pointing. The angular deviation from vertical should be maintained within a ±10 deg. (1 sigma) accuracy. The yaw reference is changing with local solar time and should be maintained within ± 20 deg. (1 sigma). The angular velocity is required below 10 deg./minute at all time.

– *Contingencies.* A number of contingency situations are foreseen, including a boom down and a high spin rate mode. The ACS should handle these cases autonomously and re-acquire the satellite.

– *Autonomy* A philosophy for the development of fault-tolerant control has been adopted in the design of the ACS (Blanke (1995)). Autonomy is achieved through development of attitude determination and control algorithms that are reconfigurable in real time. This makes it possible to accommodate changed mission phases, faults, and contingencies. An on-board supervisor (Bøgh *et al.* (1995)) monitors the spacecraft status and reconfigures ACS algorithms accordingly, to optimize the performance of the system. All on-board autonomous transitions can be controlled through up-linked, time-tagged telecommands. Further operational flexibility is provided by allowing adjustments of flight software by upload as a last resort.

A number of ACS operational modes have been identified as reflected in the Ørsted ACS architecture illustrated in Figure 5.2.

The initial rate detumbling relies entirely on the magnetometer measurement as a reference for damping the kinetic energy. After boom deployment the attitude is stabilized in three axes and three axis attitude and rate information is determined by the ADS. The available input is data from the star camera, the Sun sensor, and the magnetometer. An orbit model is dynamically updated from ground based on information from the GPS receiver. The attitude control algorithm determine a desired control torque that is used to compute the coil currents based on the measured geomagnetic field direction. A general introduction to attitude determination and control of the Ørsted satellite is provided in Bøgh *et al.* (1997). Details on the fault tolerant approach to ACS design and the atti-
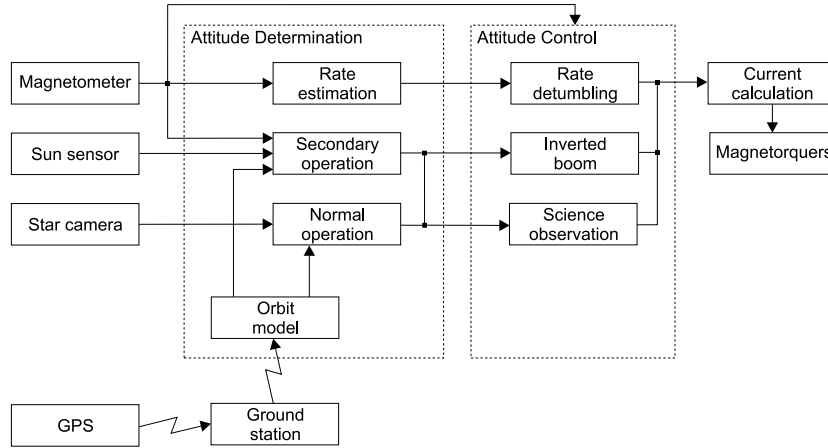
Figure 5.2: *The attitude control system configuration. The main components are sensors, attitude determination, attitude control, and actuators.*

tude control using magnetic actuation are given in the two Ph.D. theses by Bøgh (1997) and Wisniewski (1997), respectively.

5.2 The Attitude Estimation Problem

The presented system seeks to increase fault tolerance by supplementing star camera attitude estimates with attitude estimates based on magnetometer and Sun sensor data. Estimates are provided even during anomalous periods (i.e. camera blackouts, eclipse or sensor faults). Combined with detection algorithms the attitude determination algorithms introduces a significant degree of autonomy since fault can be handled without ground interaction. Derived from the control objectives three different estimation approaches are taken:

– *Rate Estimation.* The initial detumbling control law relies on the time derivative of the magnetometer measurements in order to decrease the kinetic energy of the spacecraft. The attitude estimation in this mode is hence simple estimation of the rate of change of the geomagnetic field.

– *Normal Operation.* After boom deployment and during science observation, the attitude and rates are estimated based on the star camera quaternions. In order to provide an orbit referenced attitude to the controller,

the cameras inertial attitude estimates are transformed with orbit position information into local attitude and rate estimates. The pointing requirements translate into requirements to the on-board attitude knowledge. The pitch/roll requirement is 2 deg. (1 sigma). The yaw requirement is 4 deg. (1 sigma). The error in the rate estimates should be below 0.8×10^{-4} rad/sec (1 sigma). With the star camera accuracy these modest requirements are not a problem.

– *Secondary Operation.* For contingency situations where the star camera attitude is not available, a secondary operation mode is available. Situations may include high angular rates, a boom down situation and camera blackouts due to bright objects in the field of view. The secondary operation is based on measurements from the Sun sensor and the magnetometer. The measurements are filtered by an EKF that computes attitude and rate estimates from the measured magnetic field and Sun vector together with model vectors of the geomagnetic field and the Sun direction.

After boom deployment the star camera estimates the attitude with unique accuracy provided the operational constraints of the camera are satisfied. Prior to boom deployment and in situations with faults or temporary blackout, alternative sources of information are needed to maintain adequate attitude information for control.

Rather than using sensor fusion techniques where all sensors are combined in one algorithm, the problem was separated into two parallel problems. The *normal operation* problem based on the star camera, and the *secondary operation* problem where the attitude estimates are based on the Sun sensor and magnetometer.

This decision has several consequences:

– *Reduced complexity.* In the nominal situation where the star camera is providing the attitude, the on-board computation is simplified significantly. The complex Kalman filter algorithm is only a backup.

– *Parallel development.* The two different algorithms may be developed in parallel. As design and tests of the nominal situation were scheduled prior to the different backup solutions, a simple normal operation mode was desirable.

– *Two independent on-board estimates.* Two estimates are available on-board for fault detection and integrity monitoring.

– *Decreased accuracy.* A decrease in the achievable accuracy of the secondary algorithm must be foreseen when compared to a fused solution, where the accurate star camera updates could have been used to maintain an accurate filter model.

The tradeoff has been between decreased accuracy of the attitude solution and the advantage of having two redundant algorithms.

This thesis in particular focus on the secondary operation attitude estimator, and on the situation with only magnetometer data.

5.2.1   System Design - Secondary Operation

As outlined in the previous chapters an attitude estimator based on magnetometer measurements is a complex algorithm. Besides the core estimator algorithm, a number of support functions are required as outlined in Figure 5.3.
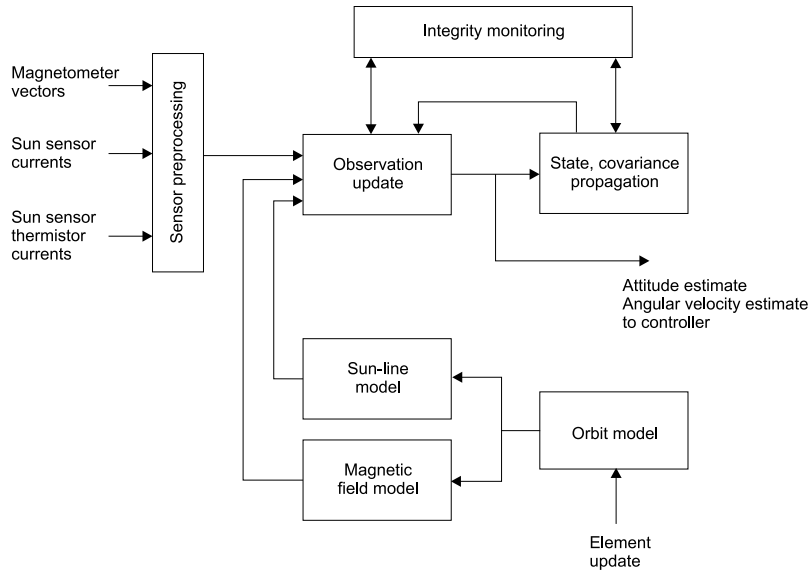

Figure 5.3: *Conceptual diagram of the Ørsted attitude estimation in secondary operation. Besides the core estimation algorithms in observational update and propagation, additional support functions are required.*

Integrity Monitoring   Faulty measurements and possible non-convergence of the filter must be detected autonomously on-board in order to achieve as high a level of autonomy as possible with simple means.

The variance of the Kalman filter innovation sequence is assumed zero mean and the variance is given by the elements of $[\boldsymbol{H}_k \boldsymbol{P}_k \boldsymbol{H}_k^T + \boldsymbol{R}(k)]$. This is exploited for the practical purposes of sensor failure detection and outlier detection of the measurement data. During operation of the filter, the innovation sequence is monitored and compared to this description. If the description is violated consistently, the filter process is declared faulty.

Innovation monitoring is also used for outlier checking of the measurements before they are processed by the filter. If a measurement residual is greater than the 3σ value computed by the filter, it is not processed. However, if this happens frequently, the cause may be either a sensor failure or a filter divergence problem. In the latter case, it is critical not to reject large residuals, since they are the only means of correcting the divergence. In the Ørsted control system, an approach has, however, been taken based on the simple 3σ in order to simplify the detector. The test levels may be modified from ground as flight experience is gained. A more elegant approach would be based on an online statistical test as outlined in Section 7.4.1.1 but this was rejected as part of a general software reduction.

Orbit Model   Ørsted is equipped with on-board GPS receivers, which, in the nominal situation, determines a state vector, consisting of position and velocity. The raw GPS measurements are osculating elements and hence not suited for simple propagation, which is based on mean elements. Test have shown that using raw GPS measurements in the orbit propagation resulted in errors of 12 km after just 16 hours (Bak (1995)).

An orbit model concept is therefore adopted based on the assumption that the GPS is not directly available for on-board ACS processing. The orbit propagation on-board is based on simple Kepler propagation with mean elements uploaded from ground every seven days. The model incorporates the primary J_2 gravitational perturbational effect on the orbit plane, which is represented by a constant drift rate for the ascending node and the apsidal line as a function of time.

The upload parameters are estimated on ground using a least square fit over seven days of propagated orbit positions from the high accuracy ground propagation model. The model provides an estimated accuracy of 15 km (1 sigma) over a seven day period (See Appendix B).

Sun-Line Model   The Sun-line reference model follows the same rational as the orbit position modeling with the Earth as an object rotating about the Sun. A unit vector pointing towards the Sun center is given in the local orbit frame. New elements may be uploaded from ground but this is not foreseen as the drift in the elements is insignificant.

Magnetic Field Model   The on-board magnetic field model is a spherical harmonics approximation to the Earth main magnetic field. The model is of order eight, based on IGRF coefficients updated to epoch 1999 (see Appendix B). As new magnetic field models become available as part of the Ørsted science mission, new parameters may be uploaded and used in the on-board field model.

Sensor Alignment and Preprocessing   The sensor measurements are preprocessed before being used in the estimator. The Sun sensors are calibrated using a five-point calibration curve to reduce nonlinearities in the sensor cosine. The calibration is based on the mean cosine error and it does not remove inaccuracies in the mounting of the detector cell on the sensor head. The result is a normalized Sun-line vector.

A linear compensation of the magnetometer is carried out that effectively removes axis non-orthogonality, sensor bias and sensitivity. The sensor preprocessing also includes outlier removal, fault detection, and alignment of the different sensor sources. A schematic overview of the instrument alignment relative to the principal frames is given in Figure 5.4.

It is clear from the figure that the alignment of the Sun sensor is relatively fixed, as it is mounted directly on the spacecraft main structure. The magnetometer, however, is mounted on the gondola, and a transformation from gondola to main body is needed. Alignment of the instruments relative to the main body is determined prior to launch within 1 deg..

An in-flight calibration of the gondola rotation relative to the main body is planned. Assuming that the gondola to body rotation is unknown, but fixed, measurements from the Sun sensor and the star camera may be used to solve for the gondola rotation. Given Sun sensor measurements with a large enough angular separation and the corresponding directions based on the star camera measurements the relative rotation of body relative to gondola may be found by solving Wahba's problem (Wahba (1965)) using eg. the SVD method.

Mass properties are calibrated prior to launch with an accuracy of 1 % (2 sigma) for the satellite configuration with the boom stowed.
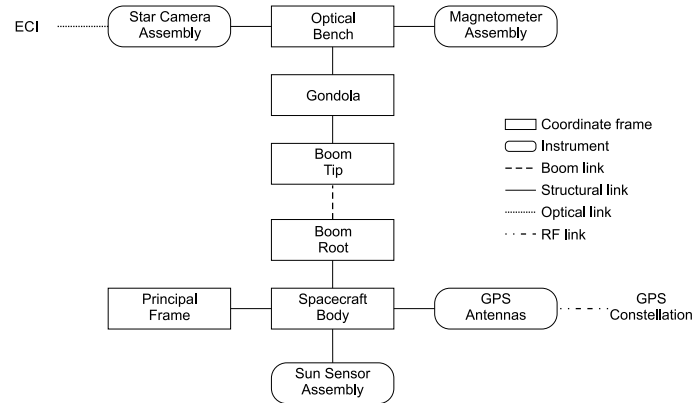
Figure 5.4: *Ørsted alignment tree.*

The next section begins the task of developing and analyzing the ADC through the identification of a *simulation model*.

5.3 Simulation Models

An accurate simulation (or truth) model is significant for the development of an ADS. The simulation model replaces the real physical system with a simulation, which realistically models the behavior of the satellite system. It yields the appropriate observations, which would be acquired by a given sensor. Within this methodology, a candidate system is designed, tuned and its performance assessed with respect to the simulation model. Since the data is simulated the true state of the spacecraft is known and the filter statistics can be easily calculated. With an accurate simulation model, the results obtained from it should apply to the actual spacecraft with a high degree of confidence.

Results from computer simulations integrating models of the sensors, the spacecraft, and its on-orbit environment are presented to demonstrate projected performance capability. Figure 5.5 gives an overview of the simulation model developed for Ørsted.

The simulation model is a powerful tool for system design only if it models the behavior of the true system with a high degree of accuracy. Sections 5.3.1 and 5.3.2 describe the properties of respectively the dynamics and sensor models. A description of the environmental models used in the simulation model are given
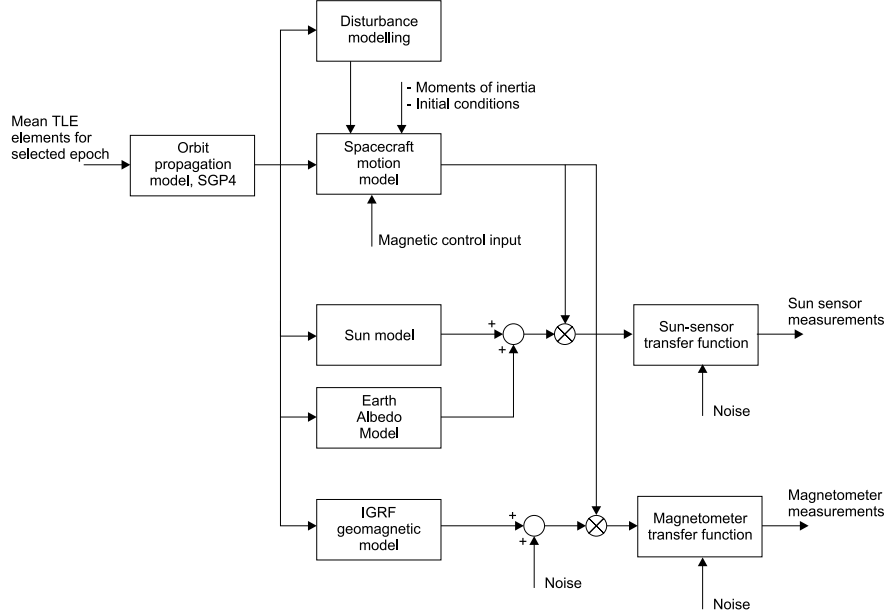
Figure 5.5: *Conceptual diagram of the Ørsted simulation model.*

in Appendix B.

5.3.1 Spacecraft Truth Model

The spacecraft simulation model includes the attitude dynamics and kinematics as described in Chapter 2. The dynamics are based on moments of inertia that may be changed in order to simulate different scenarios. The nominal (calibrated) principal inertias are given by

$$\boldsymbol{I}_{nom} = \begin{bmatrix} 219.2 & 0 & 0 \\ 0 & 219.6 & 0 \\ 0 & 0 & 1.5285 \end{bmatrix} \tag{5.1}$$

External disturbance torques include gravity gradient, magnetic disturbances, and aerodynamic drag. Moreover, control inputs are simulated. The spacecraft as a flexible body was addressed in (Bak *et al.* (1995)) and it was concluded that with a nominal boom, the lowest boom vibration mode would be 1.5 Hz. As this

is well outside the bandwidth of the ACS the satellite has been simulated as a rigid body.

Overall the modeling provides relevant disturbance torques and significant stochastic errors. The simulation model also enable tests of the effects of systematic errors in the filter model.

5.3.2 Sensor Model

The sensor simulation model simulates the observations, which are made by a sensor fitted to the spacecraft. The properties of these sensors are chosen to closely agree with the sensors used on the actual spacecraft.

The Sun vector is computed from the Sun sensor measurements where the temperature dependency has been compensated using a temperature measurement. The simulation of the Sun sensors also include the effect of Earth albedo and the nonlinearities introduced by the field of view limitations and cosine deviations of the sensor elements. The model is based on the results from the calibration that was carried out prior to launch.

The errors associated with the magnetometer are modeled using the instrument data. The star camera measurements were assumed ideal.

5.3.2.1 Geomagnetic Field Truth Model

A simulation model of the magnetic field is important for the modeling of magnetometer measurements. In order to get realistic predictions of the estimator accuracy and performance the field model must reflect the magnetic environment with a certain degree of accuracy. The issue is not so much the accuracy of the simulation model itself, but the relative accuracy of the on-board reference model and the simulation model. We want the errors in the comparison of the magnetic field measurements generated by the simulation model and the on-board reference vectors to reflect the situation in space.

An obvious first choice when selecting a simulation model would be a high order IGRF. It is, however, possible with flight data, to show that such a model does not necessarily represent the true situation.

In order to analyze the problem it is assumed that measurements from Freja (see Chapter 7) represent a situation similar to what will be experienced by Ørsted. Freja data allow us to investigate the accuracy of an on-board 8th order reference model relative to the true field. In order to avoid using attitude information, the analysis is carried out based on magnitude data. In addition to
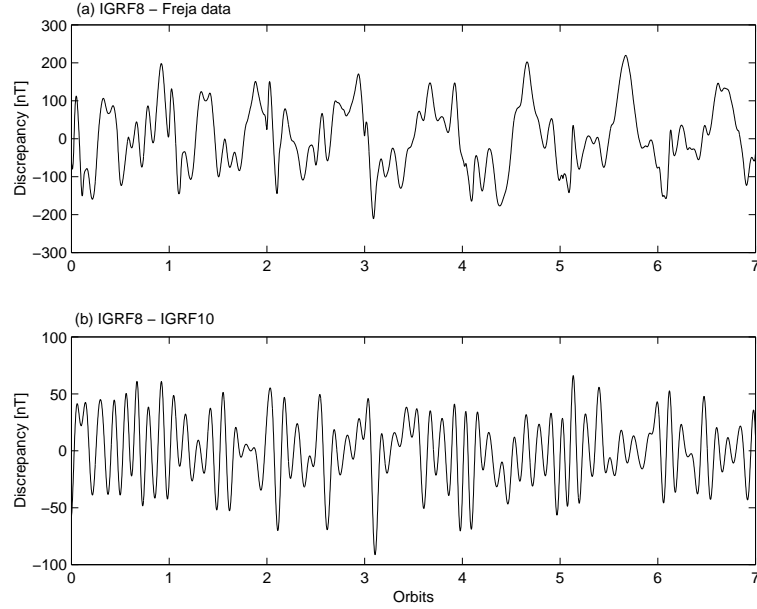
Figure 5.6: *Magnitude discrepancies between IGRF field models. (a) Freja data and results from an 8th order model. (standard deviation 86 nT). (b) Discrepancy between 8th and 10th order models (standard deviation 28 nT).*

comparing the eight order model with true data, we also make a comparison with an IGRF model of higher order (10th order) to see if such a model would be an appropriate simulation model. The results are shown in Figure 5.6.

It is clear from the discrepancies in Figure 5.6 that a higher order model not necessarily represent the best simulation model when compared to the 8th order model used in the ADS implementation. The variance of the discrepancy in Figure 5.6.a is significantly higher than the variance in Figure 5.6.b. In addition the correlation time is changed. When comparing the two results, it is important to note that in the comparison of the 8th order model with the Freja data, errors in the prediction of the orbital position is included. The comparison of the 8th order and 10th order IGRF is based on the same orbit position.

Due to the clear difference in errors, the 10th order IGRF model has not been used in the modeling of the geomagnetic field in the simulation model.

The simulation model used in the Ørsted estimator design, is based on an 8th order model, but it is augmented with a noise representation of the discrepancy in Figure 5.6.a.

To generate an error model for the results in Figure 5.6.a the errors were analyzed by looking at the auto-correlation and corresponding power spectral density (PSD). The PSD plot is shown in Figure 5.7.
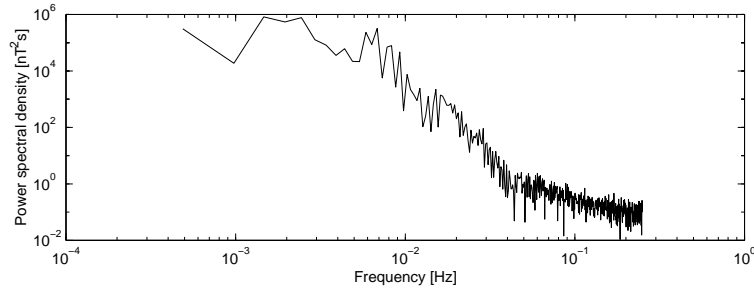
Figure 5.7: *Power spectral density plot for the magnitude error in Figure 5.6.a.*

The power spectral density curve in Figure 5.7 is approximated by a second-order Markov sequence, which provides a model of the oscillatory random phenomena in Figure 5.6.a. Data are fitted using subspace identification (Overschee and Moor (1996)). The result is a colored noise model of the form

$$\boldsymbol{x}_1(k+1) = \boldsymbol{F}_1\boldsymbol{x}_1(k) + \boldsymbol{G}_1e(k) \tag{5.2}$$

$$y_1(k) = \boldsymbol{H}_1\boldsymbol{x}_1(k) \tag{5.3}$$

where $\boldsymbol{F}_1 \in \mathbb{R}^{2\times2}$, $\boldsymbol{G}_1 \in \mathbb{R}^{2\times1}$, $\boldsymbol{H}_1 \in \mathbb{R}^{1\times2}$, and $e(k)$ is a white Gaussian noise sequence with $E\{e_i e j^T\} = \delta_{ij}$. The output of the noise model, $y_1(k)$, represents the magnitude disturbance, which must be added to the output from the field model in order to reconstruct the (magnitude) error characteristics of Freja data.

It is assumed that the magnitude errors are representative for the errors also perpendicular to the field vectors. Two additional noise sequences, $y_2(k), y_3(k)$ similar to Equation (5.2) are constructed and added perpendicular to the IGRF

field vector. The result is a field simulation model described by

$$\boldsymbol{b}_{tm}(k) = \boldsymbol{b}_i(k) + \frac{\boldsymbol{b}_i(k)}{\|\boldsymbol{b}_i(k)\|}y_1(k) + \frac{\boldsymbol{b}_i(k) \times \boldsymbol{i}}{\|\boldsymbol{b}_i(k)\|}y_2(k)$$
$$+ \frac{\boldsymbol{b}_i(k) \times \boldsymbol{b}_i(k) \times \boldsymbol{i}}{\|\boldsymbol{b}_i(k)\|^2}y_3(k) \tag{5.4}$$

where $\boldsymbol{b}_i$ is the output from the 8th order IGRF model, and $\boldsymbol{i}$ is a basis vector in the ECEF coordinate frame.

The result is a simulation model vector (Equation (5.4)) that preserve magnitude noise characteristics to first order while adding angular errors of the same magnitude and noise characteristic as the original magnitude error from Freja. Figure 5.8 shows the typical discrepancy and angular error between the simulation model vector and an 8th order model.

Figure 5.8: *Discrepancy IGRF 8th order model and simulation model. (a)-(c) x, y, z components of error in ECEF coordinates (standard deviation: 50 nT). (d) Angular error (standard deviation: 0.08 deg.).*
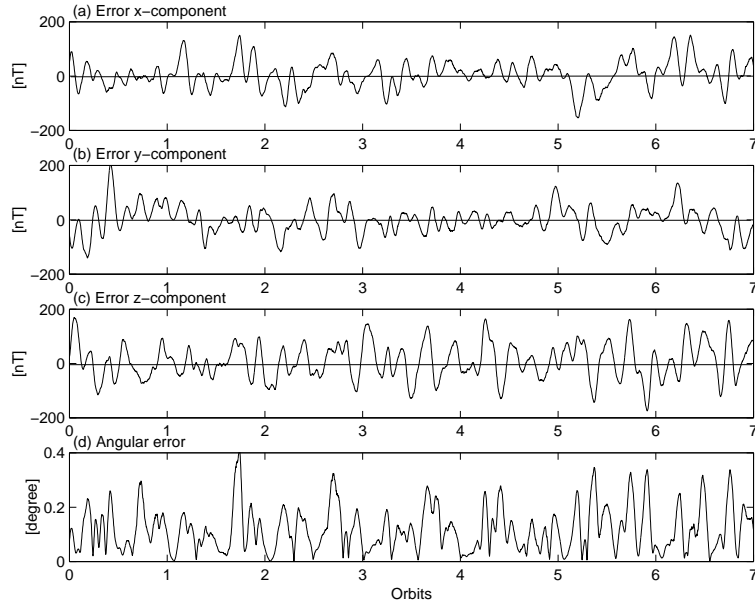
The last section has described the simulation model, which has been used to design, develop and test different ADS designs. The rest of this chapter considers

the development of the ADS. The core estimation algorithms have already been discussed and it remains to discuss the details in the implementation, and to demonstrate and test the capabilities of the attitude estimation

5.4   Estimator Design

In this section the design of the estimator is established and its performance is evaluated with respect to the simulation model. The development process is iterative and requires a large amount of simulation and evaluation of models. The presentation here, highlights some of the more important steps taken in the design

- *Process model.* Two different process models are evaluated. The process model and the corresponding noise model are treated. The tradeoff between model complexity and performance is discussed.

- *Sensor model.* The white Gaussian assumption on the sensor noise is discussed on the basis of an analysis of magnetic field models.

- *Evaluation.* The estimator designs are evaluated and the performance predicted.

The estimator design will focus on the ADS based on magnetometer measurements only. Inclusion of Sun vector measurements was discussed in Bak (1994).

5.4.1   Process Models

The model selection plays an integral role in the design of a model based estimator. The main problem is the difficulty of obtaining an accurate spacecraft dynamic model. The dynamic model presented in Chapter 3 is sensitive to uncertainty in the spacecraft moments of inertia and the external torque input. This problem has been recognized in previous work. Psiaki *et al.* (1990) suggested modeling the external torques as a random-walk process while Gai *et al.* (1985) used a first-order Markov process to model rate disturbances. In a recent paper (Oshman and Markley (1999)) the dynamic model was completely omitted, but the spacecraft angular acceleration was modeled as a first-order Markov process.

The choice of process model for Ørsted was based on the following observations

- The satellite is gravity gradient stabilized. The influence from gravity gradient may be small at the reference (zenith pointing), but when the satellite moves away from local vertical, the influence from the restoring gravity torques becomes significant. For large angular deviations from local vertical, the gravity torque is larger than the possible control torques.

- The main uncertainty associated with explicit dynamic modeling is due to the uncertainty in the moments of inertia. The inertias are calibrated prior to launch to an accuracy of 1 % (2 sigma). Only the satellite configuration with boom stowed is calibrated, and the boom deployed inertias are thus more uncertain.

- An in-flight calibration of the moments of inertia based on star camera attitude in combination with a control torque excitation is planned. The dynamic model may be adjusted accordingly in-flight.

- As Ørsted is a geomagnetic research satellite, the residual magnetic moment in the structure is tightly controlled, and the dominating external torques, after the gravity gradient, is that caused by aerodynamic drag. The uncertainty involved in modeling of the drag is significant due to the complex structure of the boom and the uncertainty of atmospheric density.

Following the observations above, the process model is designed with explicit dynamic models, which include gravity gradient. The problem remaining is to model external torques and inertia uncertainty. Selecting a filter model which yields optimal results is not a trivial process, as a more complex filter model with more states might not lead to better performance because of the bias/variance tradeoff discussed in Chapter 4. This motivates an approach where two models are examined:

- *P1 model.* This model includes the gravity gradient explicitly, but all external disturbances and inertia uncertainties are modeled as a white noise process. A purely Gaussian model of the disturbance is selected, more because of its mathematical convenience, than its ability to accurately describe the estimation errors.

- *P2 model.* In addition to explicit modeling of the gravity gradient torque, this process model includes a stochastic modeling of the external torques as a Markov process. Based on an investigation of the typical disturbance torques environment, the disturbance is modeled as an exponentially correlated process driven by zero-mean Gaussian noise.

The first of the two models is clearly an advantage from an implementation point of view, as it reduces the complexity of the filter. The penalty is that the process noise must be increased to account for unmodeled disturbances.

The P1 model   The P1 process model follows the equations of motion as described by the Equations (3.30), (3.37) and (3.39) and the perturbation state vector is given by

$$\Delta \boldsymbol{x}_{p1} = \begin{bmatrix} \Delta \boldsymbol{q} \\ \Delta \boldsymbol{\omega} \end{bmatrix} \tag{5.5}$$

No explicit modeling of the aerodynamic drag disturbance is included due to the complexity of such a model. This may lead to reduced accuracy, but the price may be acceptable as long as the results are within specifications, and the filter is consistent. The selection of process noise associated with P1 is discussed in Section 5.4.2.

The P2 model   This model augment the state vector with extra states to allow the filter to estimate the influence of the aerodynamic drag torque input. The investigation of the drag torque environment is based on a series of simulations with the simulation model. A typical example of the aerodynamic drag torque is shown in Figure 5.9. For comparison the rate influence from gravity gradient is approximately (Wertz (1978)) $\frac{3\mu}{r^3}(I_{11} - I_{33})\theta \simeq 3.8 \times 10^{-4}$ Nm at a $\theta = 10$ deg. offset from local vertical.

As the satellite body coordinate system in Figure 5.9 is approximately aligned with LVLH frame, the disturbance, n_x (pitch torque) dominates, which is not surprising as this represents the torque resulting from aerodynamic drag on the boom structure. Due to the relative low inertia about the z axis, also the torque n_z is significant. The disturbance in y is small as this axis is nominally aligned with the velocity vector. The periodic component of the signals is correlated with the orbital period and caused by the increase in atmospheric density at perigee.

The aerodynamic drag disturbance is dependent on the attitude of the satellite. Given a 90 deg. rotation in yaw, the dominating disturbance would be in y rather than x. To allow for this attitude dependence to be expressed in the model, the aerodynamic drag is modeled in the orbit frame. The aerodynamic model output is rotated to the body frame using the a posteriori estimate of the attitude prior to inclusion in the dynamic model. Allowing the attitude to distribute the drag along different axis does not include the changes in the drag
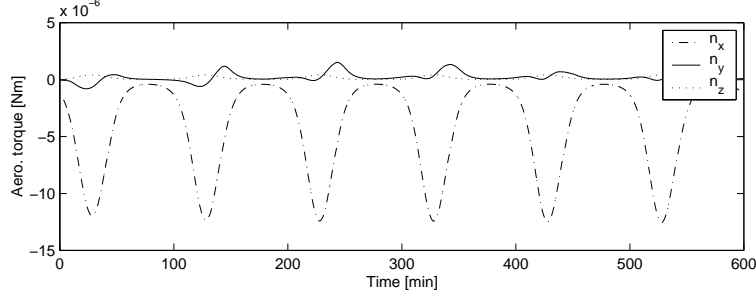
Figure 5.9: *Aerodynamic drag torque in the spacecraft body frame. The control system keeps the satellite within ±5 deg. from local vertical with a maximum yaw deviation of 20 deg.. The x axis is approximately perpendicular to the orbit plane.*

torque due to changing ram surface. The flexibility of the estimation process will allow tracking of these changes to a certain degree.

Given the low value of the torque component along the velocity vector, this component is assumed zero, and is omitted from the model.

The aerodynamic drag disturbance is clearly not Gaussian. As a first approximation the rate disturbance is modeled as a low frequency disturbance represented by an exponentially correlated process driven by zero mean Gaussian noise. Using this approach the following first-order decoupled Markov process model is established

$$\frac{d}{dt}\boldsymbol{n}_a(t) = -\boldsymbol{T}^{-1}\boldsymbol{n}_a(t) + \boldsymbol{v}_a(t) \tag{5.6}$$

where $\boldsymbol{T} \in \mathbb{R}^{2\times 2}$ is a diagonal matrix of positive time constants

$$\boldsymbol{T} \triangleq \text{diag}(T_1,\, T_2) \tag{5.7}$$

where T_i is the correlation times for the orbit referenced components of aerodynamic drag model. The $\boldsymbol{v}_a$ is a zero-mean white Gaussian noise vector with power spectral density defined by

$$\boldsymbol{Q}_a = 2\boldsymbol{\Sigma T} \tag{5.8}$$

where $\boldsymbol{\Sigma} = \text{diag}(\sigma_{a1}^2,\, \sigma_{a2}^2)$. The parameters T_i and σ_{ai} are determined based on an analysis of the autocorrelation for a number of Monte Carlo simulations of the aerodynamic drag in the orbit frame.

It is clear that for large angular deviations from local vertical, the aerodynamic torques will change significantly, and it is hence necessary to restrict the analysis to a set of scenarios, which are close (<20 deg.) to local vertical. These all represent realistic situations for the satellite in normal operation.

Different yaw references would also influence the drag model, and in such cases new parameters might be up-linked. This representation is of cause somewhat restricted and it will slowly degrade and problems may arise when large angular motion is considered.

The two states described by Equation (5.6) are augmented to the state vector and the estimates of n_a are added in the dynamic equation. The augmented state vector for the P2 model is given by

$$\Delta \boldsymbol{x}_{p2} = \begin{bmatrix} \Delta \boldsymbol{q} \\ \Delta \boldsymbol{\omega} \\ \boldsymbol{n}_a \end{bmatrix} \tag{5.9}$$

which has dimension eight. Adding two extra states adds to the complexity of the filtering process, and the tradeoff remains between accuracy and complexity. A more complex second order Markov model has been investigated, but was found not to give satisfactory results.

This section has described two different process models for the system. The P1 model assumes a simple six dimensional state space representation, which does not explicitly include aerodynamic drag. The P2 model include estimation of the aerodynamic drag influence by augmenting the state vector with two extra states.

5.4.2 Process Noise Models

Process noises take account of all the discrepancies between the nominal process model and the actual behaviour of the spacecraft. They can be classified as two different types

- Disturbances which act as input and include errors in the coil currents and aerodynamic drag.

- Noises that act on satellite parameters (in this case moments of inertia) as a result of the actual value of the parameters being unknown.

- Stabilizing noises. These are used to compensate for other unmodeled error sources like linearization. Often these noises have no clear physical basis but are required to ensure successful filter operation.

The process noise models are for the two process models are described in the following.

Input Noise   The coil currents in the torquer coils are measured directly and the measurements are assumed corrupted by additive, zero mean uncorrelated noise sources, which have a Gaussian distribution. The corruption is due to sampling and resistor tolerances. Misalignment of the coils is difficult to quantify, and is assumed negligible as the coils are an integral parts of the satellite structure.

The influence of aerodynamic drag in the P1 model is compensated for by increasing the input noise variance. In this way the simplicity obtained by not including explicit aerodynamic modeling is traded against increased process noise. The noise on the three angular velocity components is assumed uncorrelated and the spectral density given by

$$\boldsymbol{Q}_w = \text{diag}(\sigma_{w1}^2,\ \sigma_{w2}^2,\ \sigma_{w3}^2) \tag{5.10}$$

As the P2 process model include the aerodynamic drag effects explicitly, the required injection of input noise is lower as for the P1 model. Under the assumption that the aerodynamic modeling is perfect, the P2 input noise set to zero.

Parameter Noise   The second type of process noise affects the spacecraft parameters. The only parameters in the process model, which are uncertain are the moments of inertia in the dynamics, and the correlation time in the aerodynamic modeling. The modeling error due to errors in the moments of inertia has an effect on the satellite dynamics propagation. The influence is analyzed in the following.

The moments of inertia are calibrated prior to launch to an accuracy of 1% (2 sigma) in all three axes. The inertias for the satellite configuration with boom deployed is then extrapolated based on inertia information for all structural elements. It is assumed that this will result in an increase in the uncertainty to 2% (2 sigma).

Assuming that the angular velocity is represented in the principal frame, and leaving out control input, the dynamics (Equation (3.37)) may be rewritten in scalar form as

$$\dot{\omega}_1 = s_1\omega_2\omega_3 - ks_1\eta_2\eta_3 + v_{w1}$$
$$\dot{\omega}_2 = s_2\omega_3\omega_1 - ks_2\eta_3\eta_1 + v_{w2}$$
$$\dot{\omega}_3 = s_3\omega_1\omega_2 - ks_3\eta_1\eta_2 + v_{w3}$$

where v_{wi} is process noise contaminating the process, $k = 3\mu/r^3$ is the gravity constant and

$$s_1 = \frac{I_{22} - I_{33}}{I_{11}} \qquad s_2 = \frac{I_{33} - I_{11}}{I_{22}} \qquad s_3 = \frac{I_{11} - I_{22}}{I_{33}} \qquad (5.11)$$

where I_{ii} are the principal moments of inertia.

As a result of the uncertainty in the calibration of the moments of inertia, the s_i parameters used in the filter process model will deviate from the true parameters. Systematic errors like this cannot directly be modeled using Gaussian white noise processes. One possibility is to estimate them as part of an augmented state vector (see the Freja case in Chapter 7). In the Ørsted case, the systematic effects due to the s_i parameter errors are attempted compensated by increasing the variance of the process noise. Combined with a possible in-flight calibration of the inertias, this reduces the complexity of the model.

The translation from a systematic error in the inertia parameters into covariance is not really well defined. The 2% variance on the inertia matrix diagonal elements is transformed into the corresponding variance the for the σ_i parameters, and a square matrix describing the squared uncertainties in the parameters is defined by

$$\boldsymbol{Q}_\sigma = k_s \text{diag}(\Delta s_1^2,\ \Delta s_2^2,\ \Delta s_3^2) \qquad (5.12)$$

where k_s is a tuning parameter. Once the variance has been established on the inertias, the noise acting on the angular rate state is then obtained by a transformation into the state space using the noise input matrices

$$\boldsymbol{G}_e \quad = \quad \text{diag}(\omega_2\omega_3,\ \omega_3\omega_1,\ \omega_1\omega_2) \qquad (5.13)$$
$$\boldsymbol{G}_g \quad = \quad \text{diag}(-\eta_2\eta_3,\ -\eta_3\eta_1,\ -\eta_1\eta_2) \qquad (5.14)$$

The spectral density of the rate noise due to uncertainty in the inertias is then given by

$$\boldsymbol{Q}_{wi} = \boldsymbol{G}_e \boldsymbol{Q}_s \boldsymbol{G}_e^T + \boldsymbol{G}_g \boldsymbol{Q}_s \boldsymbol{G}_g^T \qquad (5.15)$$

The noise description in Equation (5.15) is dependent on the actual state of the system. Intuitively the error committed in the state propagation must be small for small rates while larger for faster motion of the satellite. This intuition is reflected in the covariance in Equation (5.15).

Stabilizing Noise   Finally it is necessary to inject additional stabilizing noise terms onto the attitude and rate states of the spacecraft. There is no physical basis for introducing a quaternion noise term, but it is included to compensate for inadequacies in the propagation of the state.

The combined noise descriptions for the P1 and P2 process models are now given by

$$
\boldsymbol{Q}_{p1} \quad = \quad \begin{bmatrix} \boldsymbol{Q}_{sq} & 0 \\ 0 & \boldsymbol{Q}_{wi} + \boldsymbol{Q}_{w} + \boldsymbol{Q}_{ws} \end{bmatrix} \tag{5.16}
$$

$$
\boldsymbol{Q}_{p2} \quad = \quad \begin{bmatrix} \boldsymbol{Q}_{sq} & 0 & 0 \\ 0 & \boldsymbol{Q}_{wi} + \boldsymbol{Q}_{ws} & 0 \\ 0 & 0 & 2\boldsymbol{\Sigma T} \end{bmatrix} \tag{5.17}
$$

where $\boldsymbol{Q}_{sq}$ and $\boldsymbol{Q}_{ws}$ are diagonal stabilizing process noise parameters. These parameters are found empirically, selected so that the ADS yields consistent estimates across a wide range of operational scenarios. The intention is to choose the minimum value of process noise such that the filter is consistent across all the scenarios produced by the simulation model (whose properties vary from low rate tumbling to stiff three-axis stabilization). The scenarios also include simulation of the systematic errors (inertia errors).

Monte Carlo simulations were set up focusing on the start of mission scenario, which restricts the orbital plane, the aerodynamic density and the reference attitude. The following systematic effects were included in the simulation model

- Inertia variations, 2% (2 sigma) variation in the simulation model inertias.

- Active control disabled/enabled.

- Initial attitude 90 yaw ± 10 deg. (1 sigma), nadir pointing ± 10 deg. (1 sigma).

- Aerodynamic drag, 10% deviations (1 sigma) from nominal atmospheric density.

- Mean anomaly and perigee was randomly chosen to allow all local geomagnetic fields and time of day to be simulated.

- Residual magnetic moment, ± 0.5 Am^2 (1 sigma).

- Control moment rotation, ± 2 deg. (1 sigma).

Different realization of the stabilizing process noise were tested on 20 Monte Carlo simulations based on the input above, and the process noise parameters were chosen that gave the best and consistent results over all 20 scenarios. The number of Monte Carlo simulations has been kept low in order to simplify the simulation time. This reduces the confidence in the results. The simulations are only are used for filter noise parameter adjustment and the number of Monte Carlo simulations reflects the confidence in the simulation model. The noise parameters may have to be adjusted according to the real flight environment.

The resulting noise parameters are summarized in Table 5.3. The focus in the selection of the noise parameters was not on initial convergence. This was addressed in separate simulations as presented below. As the process noise parameters were determined based on start of mission scenarios, re-adjustment may be required during the mission to allow for e.g. changes in the reference attitude.

5.4.3 Sensor Model

The sensor model is adopted from Section 4.7.3

$$
\begin{aligned}
\boldsymbol{z}_k &= \boldsymbol{h}(\boldsymbol{x}_k, t_k) + \boldsymbol{w}_k \\
&= \boldsymbol{A}(\mathbf{q}_k)\boldsymbol{b}_k + \boldsymbol{w}_k
\end{aligned}
\tag{5.18}
$$

The Kalman filter assumes that measurement noise is zero-mean and Gaussian. If this is not the case then a shaping filter must be constructed whose input is white noise and whose output is the observed colored noise. This filter could be obtained by experimentally obtaining a power spectral density for the measurement errors on the assumption that the true states were known.

This technique was, however, used in constructing the simulation model and using a similar technique here would most likely remove the colored noise on the measurements. It is problematic to carry the assumptions made in the simulation model over into the filter design, as this would result in a filter fitted to the simulation model. A simple approach is therefore taken that assumes zero-mean white noise on the measurements as well as on the model error. The covariances are given by the three by three diagonal matrices, $\boldsymbol{R}_m = \sigma_m^2 \mathbf{1}$, where $\sigma_m = 2\,\text{nT}$, and $\boldsymbol{R}_b = \sigma_b^2 \mathbf{1}$, where $\sigma_b = 70\,\text{nT}$. The variance on the model error is somewhat raised compared to the variance observed in Figure 5.6 to account for some of the errors introduced by the simplified white noise model.

The final noise strengths are summarized in Table 5.3.

Table 5.3: *Parameters defining the spectral densities of the process and noise for the two models P1 and P2 and the measurement noise covariance.*

P1		Parameter		Unit
i	1	2	3	
Δs_i	0.014	0.014	2.022	kgm^2
$\boldsymbol{Q}_{sq}$	1.0×10^{-9}	1.0×10^{-8}	1.0×10^{-9}	
$\boldsymbol{Q}_w$	2.0×10^{-9}	1.0×10^{-8}	2.0×10^{-13}	rad/sec^2
$\boldsymbol{Q}_{ws}$	2.0×10^{-13}	1.0×10^{-13}	2.0×10^{-15}	rad/sec^2
k_s	0.3	-	-	
$\boldsymbol{R}_m$	70^2	70^2	70^2	nT^2
$\boldsymbol{R}_b$	2^2	2^2	2^2	nT^2
P2		Parameter		Unit
Δs_i	0.014	0.014	2.022	kgm^2
$\boldsymbol{Q}_{sq}$	1.0×10^{-9}	1.0×10^{-8}	1.0×10^{-9}	
$\boldsymbol{Q}_{ws}$	2.0×10^{-13}	1.0×10^{-13}	2.0×10^{-15}	rad/sec^2
k_s	0.3	-	-	
T_i	900	900	-	sec
σ_{ai}	1.7×10^{-13}	1.7×10^{-17}	-	Nm^2
$\boldsymbol{R}_m$	70^2	70^2	70^2	nT^2
$\boldsymbol{R}_b$	2^2	2^2	2^2	nT^2

5.5   Performance Analysis for Secondary Operation

The filter described in the preceding sections was tuned so that it yields consistent estimates across the required range of operation. A number of these scenarios are presented in the following to give an indication of expected flight performance.

The presentation below focus on selected scenarios:

– *Nominal performance.* Typical nominal attitude estimation performance with satellite under control and close to nadir pointing.

– *Slow yaw spin.* A situation likely to occur whenever the active control is disabled due to aerodynamic drag torques in the z direction.

– *Convergence from large initial errors.* A typical scenario occurring during satellite commissioning and after computer resets.

– *Fault Scenario.* Scenario where the primary source of attitude information (the star camera) temporarily is unavailable.

The net effects of all modeled error sources is investigated by comparing the simulation model quantities to the corresponding estimates generated by the filter. The difference between the estimated value and its corresponding simulation model value is the actual estimation error for this quantity. As an additional check, the errors generated in this type of analysis are compared to the standard deviations predicted by the filter.

5.5.1 Nominal Attitude

The nominal attitude scenario focus on a situation where the spacecraft is under active control. The attitude is initially offset by 10 deg. in pitch. The pitch angle is gradually damped by the control system as shown in Figure 5.10.

The yaw reference in this scenario is 90 deg. (start of mission reference attitude), which results in the y axis being approximately perpendicular to the orbit plane. The angular velocities are nominally zero in x and z, while the nominal rate about the y-axis is approximately 1×10^{-3} rad/sec.

P1 Model Typical nominal attitude estimation performance for the P1 model is shown in Figure 5.11.

The error in attitude estimates, represented by pitch, yaw and roll angles as well as errors in the angular velocity are shown. Standard deviation (2 sigma) bounds are calculated by taking the square root of the diagonals of the estimated covariances and multiplying the result by two. Providing the filter is consistently tuned, the state errors should lie within these bounds at least 95 % of the time.

As a result of the tuning philosophy that focus on achieving consistent results for all scenarios, the results in Figure 5.11 do not represent the best achievable results for that specific scenario, but represents a compromise over a number of cases.

The state errors in Figure 5.11 are approximately zero mean and bounded by the two standard deviation curves and the covariance estimate is thus compatible with the actual errors. The accuracy of the yaw estimate is lower than the estimates of pitch and roll. This is due to the relative lower z-axis inertia, and the aerodynamic drag disturbance.

The periodic nature of the standard deviation profiles in Figure 5.11 are due to the periodic changes in the magnetic field vector. As an example look at the yaw errors. As the field is close to parallel to the z-axis (over pole and south pole) the system is not observable in yaw, resulting in an increase in the yaw covariance estimate, see Figure 5.12.
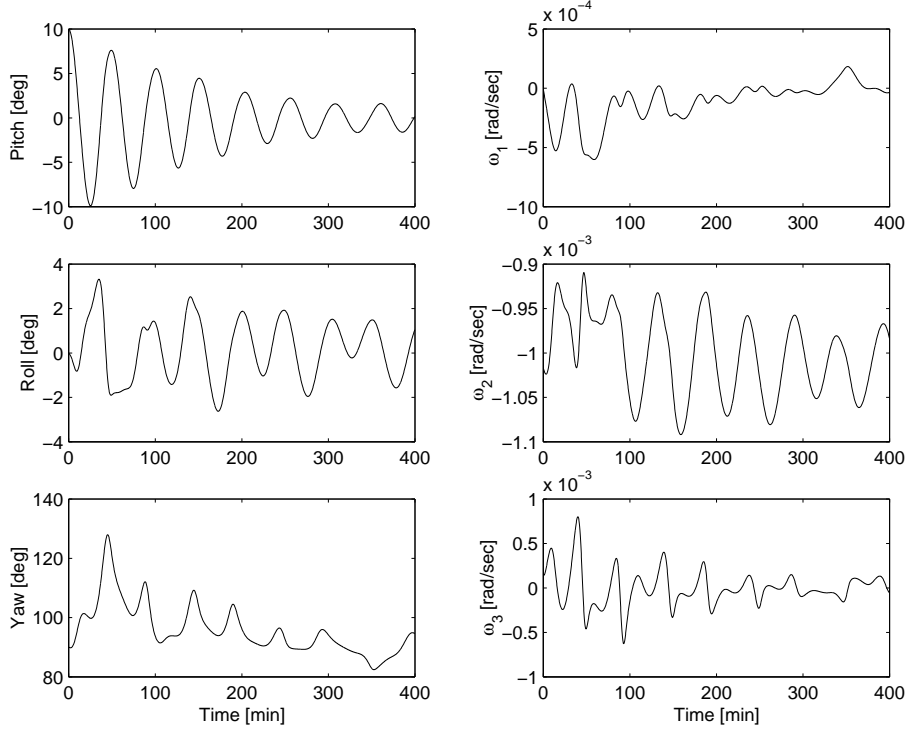
Figure 5.10: *Nominal performance – aligned with nadir by the control system. Pitch/roll/yaw relative to the local LVLH frame. Angular velocity relative to inertial frame. The nominal angular velocity in x, and z is zero, while the y component is approximately 1×10^{-3} rad/sec.*

The aerodynamic disturbance combined with poor observability drives the estimation error away from zero. The relationship between aerodynamic drag and poor observability is demonstrated in Figure 5.12. The influence of aerodynamic drag is reduced as the attitude converges towards the 90 deg. attitude reference where the outward normal to the x surface is approximately perpendicular to the translational velocity vector.

The periodic variation in covariance is not as visible in the ω_2 (pitch velocity) component as in the other two directions. This is due to the fact that the y component of the field measurements is perpendicular to the orbit plane in this attitude. As the field approximately rotates in the orbit plane, the variation in the
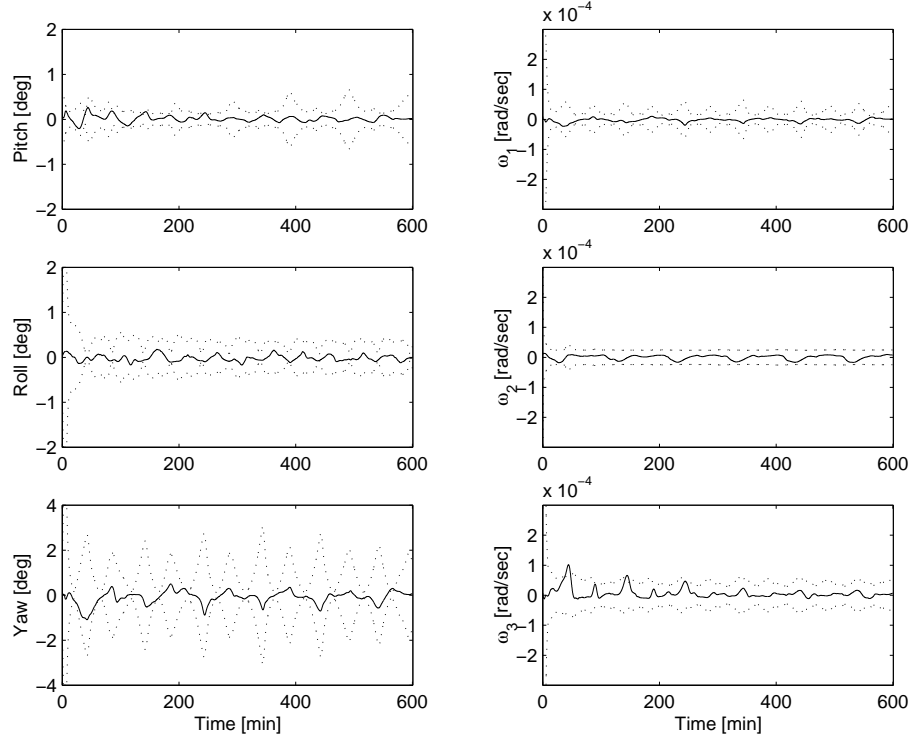
Figure 5.11: *Nominal performance. Pitch/roll/yaw and angular velocity estimation error for the P1 process model. Two standard deviation profiles are based on diagonal elements from the estimated covariance matrix (dotted lines).*

y component is not as closely coupled with the orbital period as it is the case for the x and z components of the measurements.

The accuracy of the solution presented in Figure 5.11 is approximately; pitch: 0.1 deg. (RMS), roll: 0.1 deg. (RMS) and yaw: 0.32 deg. (RMS). The angular velocity estimates deviates from the simulation model with ω_1, ω_2: 0.7×10^{-5} rad/sec (RMS), and ω_3: 1.9×10^{-5} rad/sec (RMS).

A more formal test of the consistency of the estimator is demonstrated in Figure 5.13.

Figure 5.13 shows the normalized state estimation error (Bar-Shalom and

Figure 5.12: *Nominal performance. (a) yaw error for P1 model with standard deviation envelope. (b) corresponding aerodynamic drag torque in body frame, z direction. (c) angular distance between geomagnetic field vector and the body z axis.*
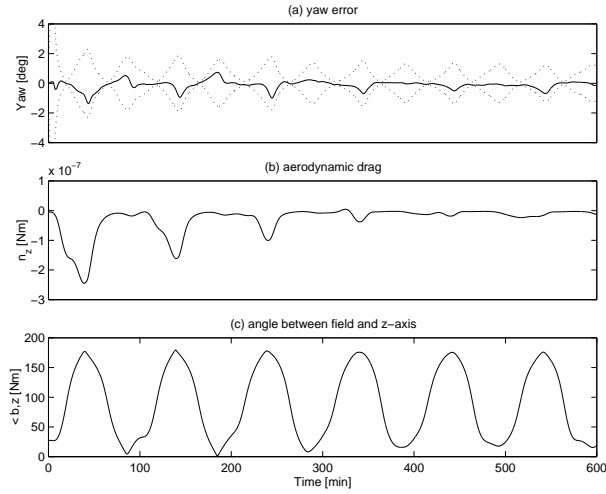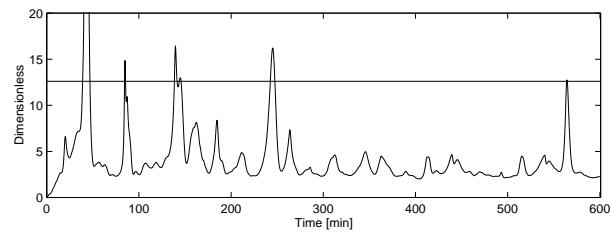

Figure 5.13: *Nominal performance. Normalized state error .*

Fortmann (1988))

$$\alpha(k) = \tilde{\boldsymbol{x}}_{k|k}^T \boldsymbol{P}_{k|k}^{-1} \tilde{\boldsymbol{x}}_{k|k} \tag{5.19}$$

where $\tilde{\boldsymbol{x}}_{k|k}$ is the error in $\hat{\boldsymbol{x}}_k$. Under the hypothesis that the estimated covariance and the true covariance match, the $\alpha(k)$ is a χ^2 distribution with n degrees of freedom. The n is the state dimension. If the filter is consistent then, by the properties of this distribution $E\{\alpha(k)\} = n$. The hypothesis is accepted with 95% confidence when the normalized error is below 12.6 since for a six degree of freedom χ^2 random variable $P\{\chi^2 \leq 12.6\} = 0.95$.

Figure 5.13 plots the normalized error for the nominal performance filter run with the P1 model. Only 2.5% of the samples are outside the confidence limit at 12.6, and it is therefore concluded that the filter is consistent.

Figure 5.13 also shows that the average value lies below the line indicating that the filter is conservative – the estimated covariance is larger than the actual mean-squared error of the estimate. This is a direct result of the tuning policy: a conservative design ensures that the filter is robust and consistent. The covariance matrix overestimates the errors and so underestimates the accuracy of the filter. However, it was found that adjusting the noise levels to make the filter more accurate in this particular case led to inconsistencies in other runs.

The innovations are plotted in Figure 5.14. They are zero mean and bounded by the standard deviations. They are clearly not white, which is a result of the simplified noise modeling. Periodic field model errors were introduced, but the noise model assumed a white noise discrepancy. The relative small y component is a result of a generally small y component of the geomagnetic field in the orbit frame.

P2 Model Results with the augmented P2 model on the same scenario are given in Figure 5.15. The errors in yaw and pitch are reduced as a result of the aerodynamic modeling. The reduced stabilizing state noise on the angular velocity results in lower variance bounds and thereby more confidence in the dynamic model.

The errors in Figure 5.15 are approximately pitch: 0.07 deg. (RMS), roll: 0.1 deg. (RMS) and yaw: 0.28 deg. (RMS). The rate errors are ω_1: 0.7×10^{-5} rad/sec (RMS), ω_2: 0.32×10^{-5} rad/sec (RMS), and ω_3: 1.4×10^{-5} rad/sec (RMS). The angular velocity error are hence reduced especially in ω_2 and ω_3, which are the two axis that are most affected by aerodynamic drag.

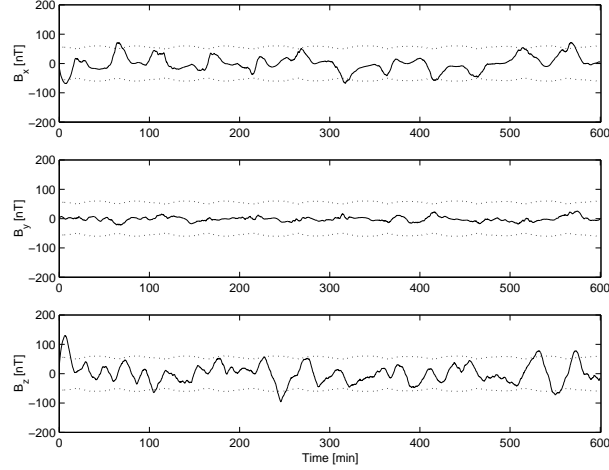The two estimated components of the aerodynamic drag in the LVLH are

Figure 5.14: *Nominal performance. Innovation sequence for the P1 process model. Standard deviation profiles are based on diagonal elements from $\boldsymbol{H}_k\boldsymbol{P}_{k|k-1}\boldsymbol{H}_k^T\boldsymbol{R}(k)$ (dotted lines).*

given in Figure 5.16. After an initial convergence the errors are approximately zero mean and bounded by the standard deviation bounds. The n_x component is negative due to the forces acting on the boom structure, which forces the boom backwards in the orbit plane. The error in n_x is 1.0×10^{-6} (RMS) and the n_z error is 2.3×10^{-7} (RMS). This corresponds to approximately 6% of the simulated peak-to-peak aerodynamic drag torque.

It is clear from the results above that the augmented P2 process model performs better in terms of accuracy than the P1 model. The model has, however, proved to be somewhat sensitive to the aerodynamic modeling. The Ørsted requirements in term of accuracy of the on-board estimator are modest, (2 deg. (1 sigma) in roll/pitch, and 4 deg. (1 sigma) in yaw), and the P1 model is within these requirements. One of the main problems associated with the on-board filter has been the complexity of the algorithm. The reasons included very limited memory space and implementation in fixed point arithmetic. It was therefore decided to proceed with the P1 model, paying the price of reduced accuracy.
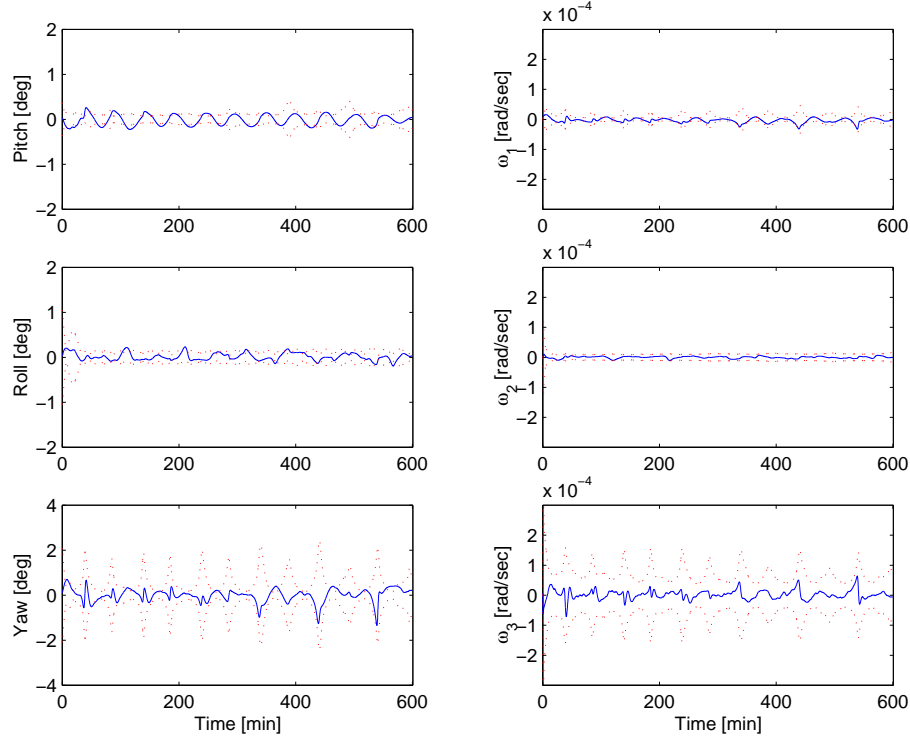
Figure 5.15: *Nominal performance. Pitch/roll/yaw and angular velocity estimation error for the P2 process model. Two standard deviation profiles are based on diagonal elements from the estimated covariance matrix (dotted lines).*

5.5.2 Slow Drift

This scenario represents a typical situation, which is expected for Ørsted. The attitude control is disabled resulting in a slow spin of the satellite about the z-axis due to the influence of aerodynamic drag.

The attitude and velocity time histories are show in Figure 5.17. The satellite is initially offset 10 deg. in pitch and rotates slowly about the boom axis with a rate of 2.9×10^{-3} rad/sec. The spin exceeds the star camera constraint, and no star camera attitude would therefore be available in such a situation.

The performance of the P1 filter, in the slow spin case is demonstrated in
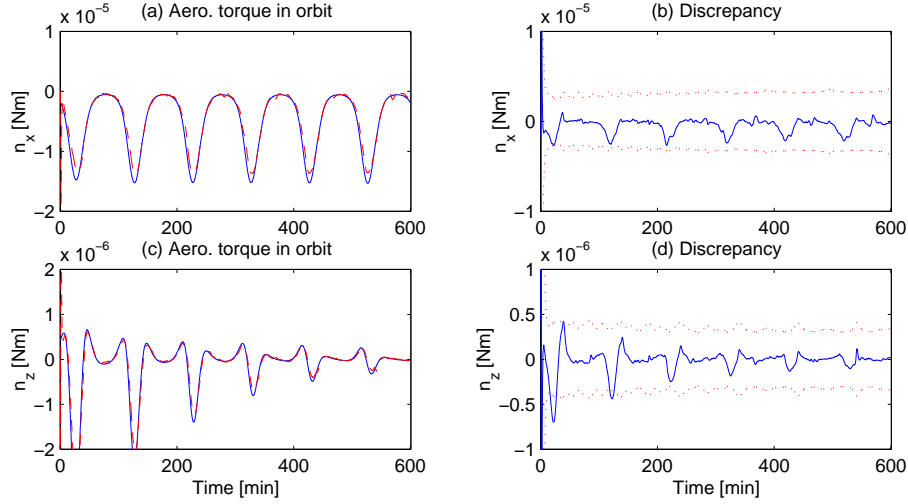
Figure 5.16: *Nominal performance. Aerodynamic drag torques in the LVLH frame. (a), (c) estimated and true n_x and n_z drag torques. (b), (d) estimation error. Standard deviation profiles are based on diagonal elements from the estimated covariance matrix (dotted lines).*

Figure 5.18, which plots the state error. The filter is clearly able to track the spinning satellite after a short convergence period. The shape of the covariance bounds change dramatically due to the spin of the spacecraft and the resulting rotation of the geomagnetic field in the body frame xy plane. A similar effect is naturally not seen in the z components.

The approximate accuracy is reduced to; pitch: 0.26 deg. (RMS), roll: 0.23 deg. (RMS) and yaw: 0.8 deg. (RMS), which may be attributed to the increase in state noise induced by the inertia uncertainty modeling. The angular rate errors are increased to ω_1, ω_2: 2.9×10^{-5} rad/sec (RMS), and ω_3: 2.7×10^{-5} rad/sec (RMS).

5.5.3 Large Initial Error

The ability of the filter to converge from large initial attitude knowledge errors was investigated. This scenario will naturally occur during commissioning of the satellite, but also during the mission whenever the ADS is temporarily disabled
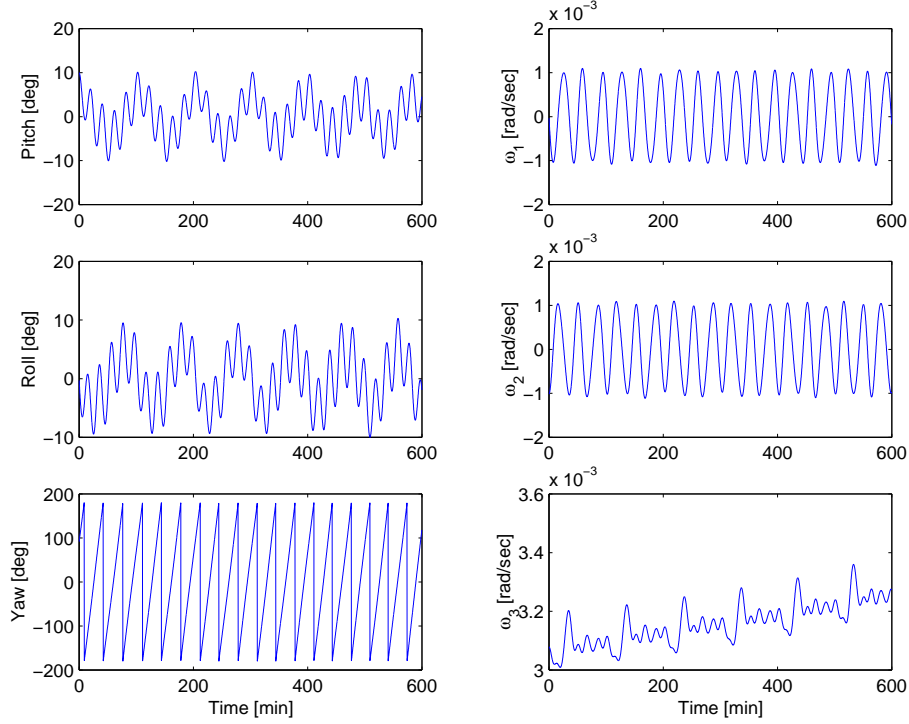
Figure 5.17: *Slow spin – the satellite spins slowly about the z-axis. Pitch/roll/yaw relative to local LVLH frame. Angular velocity relative to inertial frame.*

due to computer reset or similar events.

The initial knowledge errors were set to 40, 30 and 60 deg. in the three axes, and the rate error was 1×10^{-4} rad/sec in ω_3. The time history for attitude and rate are shown in Figure 5.19. The control system is enabled with an attitude reference of 0 deg. yaw.

The estimation results are show in Figure 5.20. After approximately half an orbit the error is within the 2 sigma bounds in attitude, while the rate convergence is a little slower. The accuracy after convergence is comparable to the accuracies achieved in the nominal attitude reference case described in Section 5.5.1.

Figure 5.20 shows errors larger than the covariance which imply that the initial covariance is too small. The initial covariances have been selected based
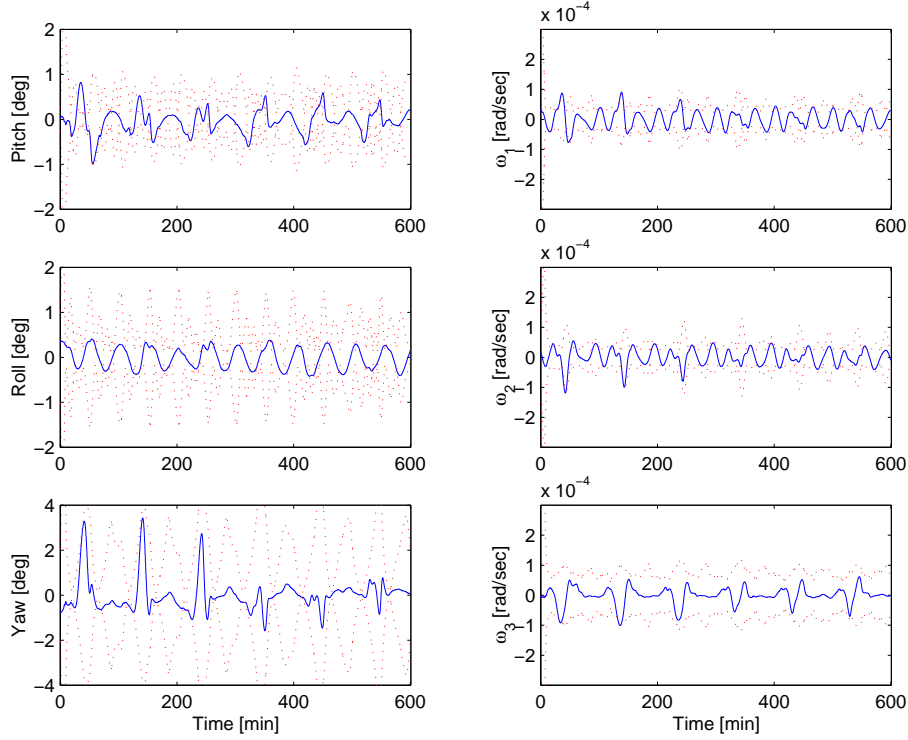
Figure 5.18: *Pitch/roll/yaw and angular velocity estimation error for the P1 process model. Two standard deviation profiles are based on diagonal elements from the estimated covariance matrix (dotted lines).*

on a χ^2 test for the individual initial estimation errors, such that

$$\tilde{x}_i(0|0)^T P_i(0|0)^{-1} \tilde{x}_i(0|0) \leq c \tag{5.20}$$

where c is a constant representing the upper limit of the 95% confidence region from the χ^2 distribution with one degree of freedom. The $\tilde{x}_i(0|0)$ is the assumed deviation from the true initial state variable i, and $P_i(0|0)$ is the associated covariance.

The simulations carried out during the filter design showed convergence problems in a few cases with angular rates above 0.05 rad/sec. This is higher than the satellite is ever expected to experience.
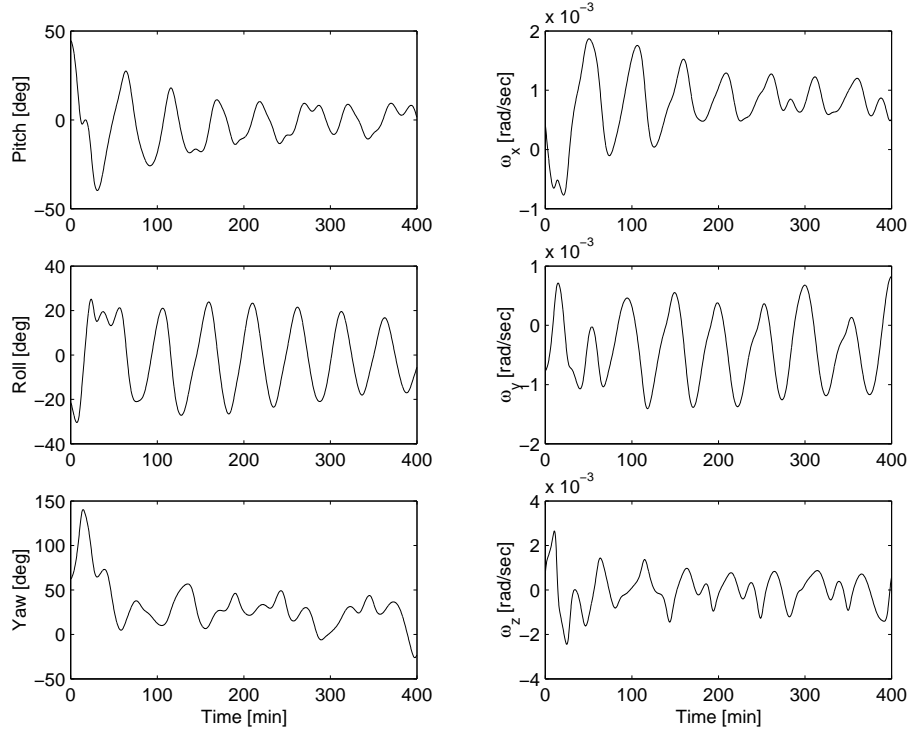
Figure 5.19: *Large initial error – the satellite is offset 40, 30 and 60 deg. in the three axes. Pitch/roll/yaw relative to local LVLH frame. Angular velocity relative to inertial frame.*

5.5.4 Fault Scenario

Numerous simulations have been performed to test a wide range of attitude- and fault conditions. As an example, combined attitude control and estimation results are shown in Figure 5.21 for a situation with star camera blackout.

The initial attitude is offset from local vertical by 15 deg. in pitch. The star camera halts after two orbits (200 min). In Figure 5.21.a the control system is reconfigured, and the magnetometer based ADS estimate is used as a basis for control. Figure 5.21.b shows the same situation but in this case no on-board reconfiguration is performed and the satellite starts rotating about the boom axis due to the aerodynamic drag. This case clearly demonstrates the ability of the
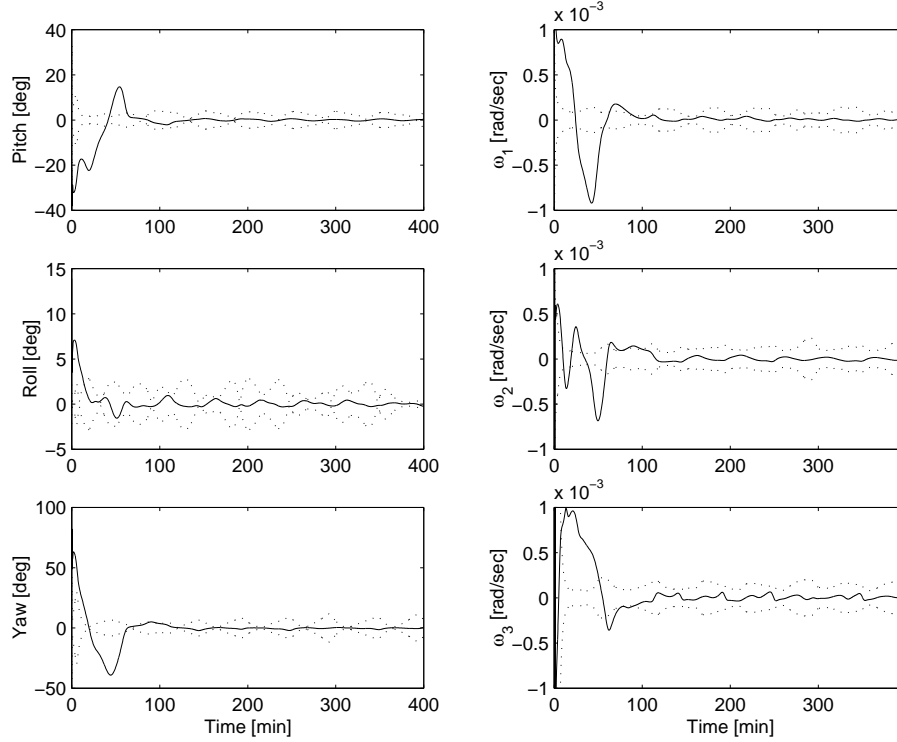
Figure 5.20: *Convergence of the P1 process model. The estimate converges from an initial knowledge error of 40, 30 and 60 deg. in the three axes. The approximate convergence time is 0.5 orbit.*

control system to reconfigure and adopt to fault situations.

5.6 Error Analysis

In order to quantify the effects of different systematic errors on the ADS performance an error budget has been established. The results are obtained by introducing a systematic error in the simulation model. All other systematic errors are set to zero. The filter is then simulated 20 times in a Monte Carlo simulation similar to the results in Figure 5.10 with varying initial state and orbital position. The RMS error is then calculated across the 20 simulations. The
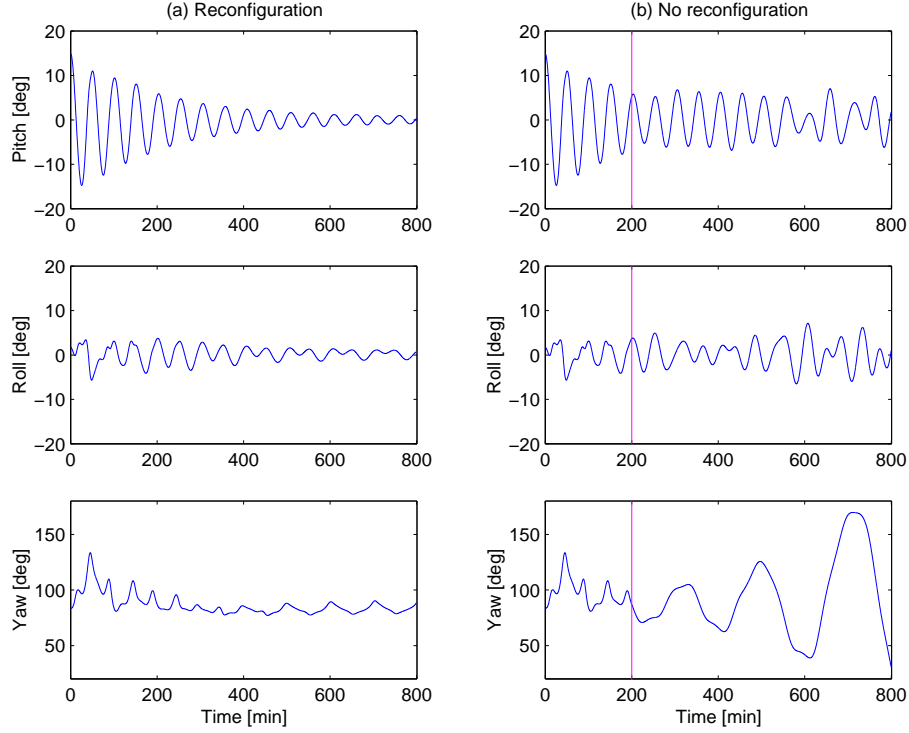
Figure 5.21: *Fault scenario - camera blackout after 200 minutes. In plot a) re-configuration is performed. In b) the attitude determination is not reconfigured.*

number of Monte Carlo simulations is again limited to 20 in order to reduce simulation time. Given that the estimated variances are normal and independently distributed, they may be assumed to follow a χ^2 distribution such that

$$\frac{1}{n}\sum_{i=1}^{n}\hat{\sigma}_i^2 \in \frac{\sigma^2}{n}\chi^2(n) \tag{5.21}$$

where n is the number of Monto Carlo simulations, $\hat{\sigma}_i^2$ is the estimated variance of each simulation, and σ^2 is the variance of the estimates variances. As the variance of the $\chi^2(n)$ is $2n$, the relative standard deviation of the estimated variance

may be found as

$$\frac{\sqrt{\frac{\sigma^4}{n^2}2n}}{\sigma^2} = \sqrt{\frac{2}{n}} \tag{5.22}$$

For $n = 20$ the result is a 30% relative standard deviation.

Table 5.4 summarizes the results from six different scenarios.

Table 5.4: *Error analysis, systematic errors in the simulation model.*

	RMS value deg.			RMS value 10^{-5}rad/sec		
Error source	Roll	Pitch	Yaw	ω_1	ω_2	ω_3
2% inertia error	0.08	0.07	0.45	0.97	0.74	1.88
Inertia axis skew 2 deg.	0.22	0.24	1.26	2.70	2.78	3.75
Atmospheric density (110%)	0.11	0.14	0.48	0.77	1.07	2.03
0.5 Am^2 residual moment	0.23	0.10	0.79	1.90	0.85	2.39
Field model error (10th)	0.09	0.08	0.44	0.86	0.82	1.92
Control moment skew 2 deg.	0.09	0.16	0.41	0.79	1.14	2.32
RSS Error	0.37	0.35	1.73	3.72	3.48	6.05

The filter is relatively insensitive to errors in the 2% error in inertias, which is attributed to the fact that the noise covariance matrix has been increased to include this error on the principal elements. The second item in Table 5.4 is a rotation of the principal axis of 2 deg.. This is the main contributor to the RSS error. Off diagonal elements in the inertia were not accounted for by the filter and hence has a large effect on the filter state propagation. In a flight application this effect may be reduced by an in-flight calibration of the inertias. The 10% increase in atmospheric density does not affect the filter performance significantly.

A 0.5 Am^2 magnetic residual moment was applied in the y axis (pitch). This has no effect on pitch accuracy as the torque lies in the xz–plane. The effect of this systematic error is observed in roll and yaw. The calibration of the Ørsted residual moment prior to launch showed that a 0.5 Am^2 residual is not likely to occur.

In order to simulate the effect of a different field reference model the simulation model was modified to a 10th order IGRF model. The use of a 10th order

model seems to have little effect on the filter performance. As it was seen in Figure 5.6 the variance of the 10th order model compared to the 8th order model is lower than the variance of the field model discrepancies used in the nominal simulation model. From this it is clear that the current measurement noise covers the systematic error introduced by using the 10th order model. The analysis shows that filter is not sensitive to the changes in frequency of the reference field model.

Finally a 2 deg. rotation was applied to the control moment vector, which only has limited effect on the accuracy. This is mainly due to the relative low magnetic control moment ($m_{ctrl} \leq 0.6 \text{Am}^2$) generated during the scenario in Figure 5.10.

The root square sum (RSS) in Table 5.4 indicate an expected accuracy of approximately 0.37 and 0.34 deg. in pitch and roll and 1.73 in yaw. The RSS errors in angular velocity are approximately 3.72×10^{-5} rad/sec in ω_1, 3.48×10^{-5} rad/sec in ω_2 and finally error is 6.05×10^{-5} rad/sec. This result is well below the specifications in angles and marginally below the specification in the angular rates. Even with the 30% relative standard deviations on the results does not violate specifications.

5.7 Summary

The objective of this chapter has been to develop an ADS for estimation of three-axis spacecraft attitude and rate information, based solely on three-axis magnetometer measurements.

A system for estimating three-axis spacecraft attitude and rates by Kalman filtering of magnetometer data has been described. The Kalman filter estimates are supplementing star camera based estimates. The two estimation algorithms operate in parallel providing fault tolerance towards Sun sensor and star camera blackouts. Combined with detection algorithms the presented attitude determination introduces a significant degree of autonomy.

Section 5.1 presented the motivation and problems associated with the ADS, which has been incorporated in the attitude control system for the Ørsted satellite. Section 5.2 addressed the requirements to the ADS while Section 5.3 described the simulation model which is the basis for tests of the estimator design. Two process models were presented in Section 5.4 and their noise parameters specified.

In Section 5.5 the simulated results of the actively controlled, zenith pointing

spacecraft demonstrated the ability of the estimation algorithm. With the system described, sufficient in-flight attitude estimation accuracy is maintained for attitude control purposes. Finally Section 5.6 presented an error budget which combines the effects of a number of systematic errors. The attitude determination based on magnetometer data only was found effective and the obtained accuracies were 0.37-0.34 deg. in pitch/roll, 1.73 deg. in yaw. The angular rate accuracies were found to be ω_1: 3.72×10^{-5} rad/sec, ω_2: 3.48×10^{-5} rad/sec, and finally ω_3: 6.05×10^{-5} rad/sec. A 30% standard deviation is estimated on these results.

Chapter 6

Implementation and Results from Ørsted

It is well–known that the Kalman filter in its original formulation is sensitive to numerical inaccuracy and the extended Kalman filter has potential instability. As the Kalman filter described in the previous chapter is developed for implementation in the on-board computer of the Ørsted satellite the numerical behaviour of the algorithm has to be addressed. Section 6.1 gives a brief description of the issues related to a fixed point Ada implementation for Ørsted. Section 6.2 presents results from the on board ADS. The results from the magnetometer based estimation of attitude are compared to star camera attitudes thereby providing an assessment of the absolute accuracy.

6.1   Implementation

Up to this point the discussion has focused on a theoretical performance of the Kalman filter using given truth models for simulations. It is, however, well–known that the Kalman filter in its original formulation may predict results that differ from observed behaviour. This difference or divergence may be caused by: modeling errors, poor state observability, and numerical inaccuracy. This section focuses on the numerical issue.

The Ørsted on-board software and thereby the control system was implemented using the Ada programming language. This choice was not necessarily wise when considering numerical intensive algorithms, but Ada provide other software engineering benefits like readability, maintainability, portability, etc.

that were important for the project development.

The Kalman filter is evaluated in the on-board processor as a real time process, implying that the filter has to perform the necessary calculations between samples. As the sampling time is relative low (10 seconds) this is not a severe constraint. The main practical constraints were caused by the fixed point arithmetic and the code size.

6.1.1   Core Numerical Algorithms

The main problem with a fixed point implementation is the reduced dynamic range imposed by the arithmetic, which may lead to divergence of the filter. The internal data flow in the Kalman filter consists basically of two estimation loops. The estimated mean (state estimate) is propagated around one loop, and the covariance in another.

– In the state estimation loop, errors in the estimated mean introduced by roundoff and noise are compensated by feedback through the weighted (Kalman gain) innovation.

– The covariance loop is not stabilized by feedback, and as a result, errors propagate and accumulate. This may lead to errors in the mean estimate and divergence of the filter. The computations involved in the covariance prediction must therefore be addressed.

Implementation methods for reducing the effects of roundoff errors in the covariance loop have been intensely studied since the numerical difficulties with the Kalman filter were first addressed in the mid seventies. The most successful and numerical stable implementations are based on the idea of propagating symmetric products of triangular factors for the covariance matrix, rather that the covariance matrix itself (Grewal and Andrews (1993)).

The Ørsted ADS employs a covariance formulation, which is based on a modified Cholesky decomposition (UD decomposition) of the covariance matrix. This formulation provides adequate covariance matrix precision with single precision fixed-point arithmetic.

The measurement update is done using Bierman's *Square Root Free* square root observational update (Bierman (1977)), and the covariance time update is based on Thornton's *modified weighted Gram-Schmidt algorithm* (Thornton (1976)). These methods belong among the most numerically stable algorithms for Kalman filter implementation (Grewal and Andrews (1993)).

6.1.1.1 Observation Update

On Ørsted, the observational update realization is based on modified Cholesky (UD) decomposition of the covariance matrix. The UD decomposition of a symmetric positive definite square matrix M is a decomposition into products of U and D such that $M = UDU^T$, where U is unit upper triangular and D is diagonal with non-negative elements.

Recall (Equation (4.24)) that the observational covariance update is given by

$$P_{k|k} = P_{k|k-1} - P_{k|k-1}H_k^T \left(H_k P_{k|k-1} H_k^T + R(k)\right)^{-1} H_k P_{k|k-1} \quad (6.1)$$

Being a symmetric positive definite square matrix, P may be factorized using the UD factorization

$$
\begin{aligned}
P_{k|k} &\triangleq U_{k|k} D_{k|k} U_k^T \\
P_{k|k-1} &\triangleq U_{k|k-1} D_{k|k-1} U_{k-1}^T
\end{aligned}
$$

With these definitions and by introducing $\lambda_k \triangleq U_{k-1}^T H_k^T$, Equation (6.1) may be rewritten as

$$
P_{k|k} = U_{k|k-1}\Bigg[D_{k|k-1} \\
- D_{k|k-1}\lambda_k \left(\lambda_k^T D_{k|k-1}\lambda_k + R(k)\right)^{-1}\lambda_k^T D_{k|k-1}\Bigg]U_{k|k-1}^T
\quad (6.2)
$$

Now regard the unfactored expression within the brackets in Equation (6.2). Bierman (1977) showed how this term may also be UD factorized in the form

$$D_{k|k-1} - D_{k|k-1}\lambda_k \left(\lambda_k^T D_{k|k-1}\lambda_k + R(k)\right)^{-1}\lambda_k^T D_{k|k-1} = \tilde{U}\tilde{D}\tilde{U}^T \quad (6.3)$$

and therefore

$$U_{k|k}D_{k|k}U_k^T = U_{k|k-1}\tilde{U}\tilde{D}\tilde{U}^T U_{k|k-1}^T$$

Since the product of unit upper triangular matrices is unit upper triangular it follows that

$$U_{k|k} = U_{k|k-1}\tilde{U} \quad \text{and} \quad D_{k|k} = \tilde{D}$$

The UD factors of the a posteriori covariance $P_{k|k}$ may thus be computed directly from the UD factors of the a priori covariance $P_{k|k-1}$ given that Equation (6.3) is factored. The algorithm of Bierman (Bierman (1977)) provide a

numerically stable and efficient method for factorization of the expression in Equation (6.3). The Bierman algorithm is surprisingly simple and does not involve square roots in the implementation. It requires little more computation than the conventional Kalman update and the Kalman gain is recoverable from partial results in the algorithms.

By performing the update through the UD factors as described above, the positive semi-definite structure of the covariance matrix is preserved. In fact the covariance is never calculated in the filter, thereby reducing the required range of the variables. The implemented version of the Bierman update uses 32 bit fixed point precision for representing the UD factored results.

Scalar Measurement Processing Recall that the measurement noise description discussed in Section 4.7.3 results in a full measurement noise covariance matrix, $\boldsymbol{R}(k)$ defined by

$$\boldsymbol{R}(k) = \boldsymbol{R}_m(k) + \boldsymbol{A}(\hat{\mathbf{q}}_{k|k-1})\boldsymbol{R}_b(k)\boldsymbol{A}(\hat{\mathbf{q}}_{k|k-1})^T \qquad (6.4)$$

where $\boldsymbol{R}_m$ and $\boldsymbol{R}_b$ describe the sensor noise and geomagnetic field model errors respectively.

Significant reduction in the computational complexity may, however, be achieved by having a diagonal (uncorrelated) observation noise covariance matrix in Equation (6.3). The vector measurement can thus be processed serially as scalars, which reduces the computational complexity significantly. This decorrelation may be achieved through UD decomposition of $\boldsymbol{R}(k)$. This redefines the measurement vector such that the components are uncorrelated.

Given the current selection of $\boldsymbol{R}_m$ and $\boldsymbol{R}_b$ as diagonal matrices, and specifically $\boldsymbol{R}_b$ as a multiple of the identity, Equation (6.4) is diagonal and sequential processing of scalars without the need for an additional UD decomposition is thus possible.

6.1.1.2 Time Update

The covariance time update is based on Thornton's modified weighted Gram-Schmidt algorithm (Thornton (1976)). By working directly on the UD factors the temporal update is ideally suited in combination with the Bierman update.

Discrete Covariance Prediction   The update works based on a discrete time covariance prediction, that is

$$\boldsymbol{P}_{k|k-1} = \boldsymbol{\Phi}(t_k, t_{k-1}) \boldsymbol{P}_{k|k} \boldsymbol{\Phi}^T(t_k, t_{k-1}) + \boldsymbol{Q}_{k-1} \tag{6.5}$$

which was defined in Equation (4.85). As the sampling interval Δt is small compared to the eigenvalues of $\boldsymbol{F}(t)$ at any given instant in time, it may adequately be represented as a constant over a sampling interval (of the filter) and the state transition matrix may approximated by a truncated matrix exponential

$$\boldsymbol{\Phi}(t_k, t_{k-1}) \simeq \boldsymbol{1} + \boldsymbol{F}(t_{k-1}) \Delta t + \frac{1}{2} \boldsymbol{F}^2(t_{k-1}) \Delta t^2 \tag{6.6}$$

As significant approximations have already been made in modeling of the process noise $\boldsymbol{Q}(t)$ the discrete equivalent is only approximated to first order

$$\boldsymbol{Q}_{k-1} \simeq \boldsymbol{Q}(t_{k-1}) \Delta t \tag{6.7}$$

Update of UD Factors   The time update uses triangularization of the $\boldsymbol{Q}_{k-1}$ matrix through an UD decomposition

$$\boldsymbol{Q}_{k-1} = \boldsymbol{U}_q(k-1) \boldsymbol{D}_q(k-1) \boldsymbol{U}_q(k-1)^T$$

where $\boldsymbol{D}_q(k-1)$ is a diagonal matrix. When the UD factors of $\boldsymbol{P}_{k|k-1}$, $\boldsymbol{P}_{k|k}$, and $\boldsymbol{Q}_k$ are introduced, the time update in Equation (4.85) may be transformed to

$$\boldsymbol{P}_{k|k-1} = \boldsymbol{A}_g^T \boldsymbol{D}_w \boldsymbol{A}_g \tag{6.8}$$

where

$$\boldsymbol{A}_g = \begin{bmatrix} \boldsymbol{U}_{k|k}^T \boldsymbol{\Phi}^T(t_k, t_{k-1}) \\ \boldsymbol{U}_q(k-1) \end{bmatrix} \quad \text{and} \quad \boldsymbol{D}_w = \begin{bmatrix} \boldsymbol{D}_{k|k} & \boldsymbol{0} \\ \boldsymbol{0} & \boldsymbol{D}_q(k-1) \end{bmatrix}$$

Weighted Gram-Schmidt orthogonalization (Grewal and Andrews (1993)) of $\boldsymbol{A}_g$ with respect to the weighting matrix $\boldsymbol{D}_w$ defines a unit lower triangular matrix $\boldsymbol{L}$ such that $\boldsymbol{A}_g = \boldsymbol{B} \boldsymbol{L}$ and

$$\boldsymbol{B}^T \boldsymbol{D}_w \boldsymbol{B} = \boldsymbol{D}_b \tag{6.9}$$

where $\boldsymbol{D}_b$ is a diagonal matrix representing the fact that the column vectors of $\boldsymbol{B}$ are orthogonal with respect to $\boldsymbol{D}_w$[1]. Using the result of the weighted Gram-Schmidt orthogonalization, Equation (6.8) may be reformulated as

$$\begin{aligned} \boldsymbol{P}_{k|k-1} &= \boldsymbol{L}^T \boldsymbol{B}^T \boldsymbol{D}_w \boldsymbol{B} \boldsymbol{L} \\ &= \boldsymbol{L}^T \boldsymbol{D}_b \boldsymbol{L} \end{aligned} \tag{6.10}$$

As UD factorization is unique, and $\boldsymbol{L}$ is unit lower triangular and $\boldsymbol{D}_b$ diagonal the temporal update of the UD factored covariance is given by

$$\boldsymbol{U}_{k|k-1} = \boldsymbol{L}^T \quad \text{and} \quad \boldsymbol{D}_{k|k-1} = \boldsymbol{D}_b \tag{6.11}$$

This is used directly in the measurement update outlined above. The covariances are thus never directly calculated in the real-time implementation. The combined covariance prediction implemented on Ørsted is shown in Figure 6.1.
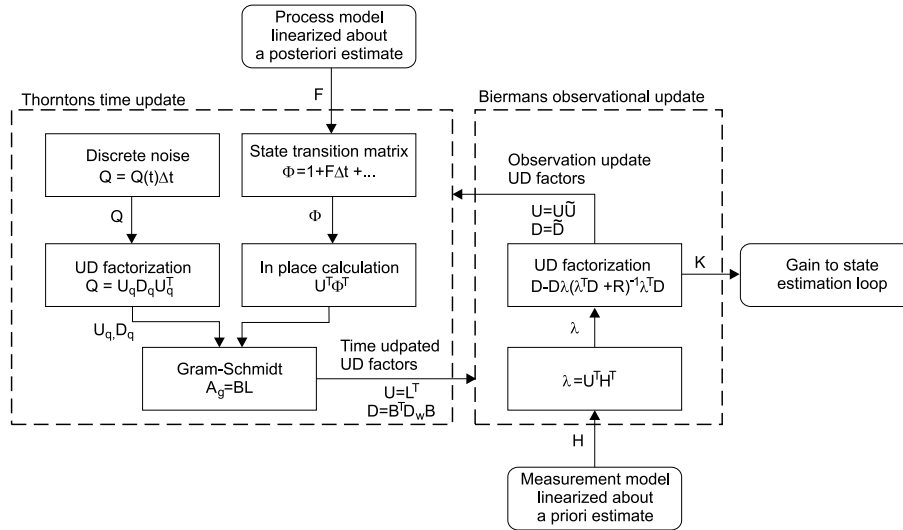

Figure 6.1: *Schematically overview of the covariance prediction implemented on Ørsted. Bierman's square root free measurement update is combined with Thornton's temporal update .*

---

[1]The vectors $\boldsymbol{x}$ and $\boldsymbol{y}$ are said to be orthogonal with respect to $\boldsymbol{D}_w$ if the weighted inner product $\boldsymbol{x}^T \boldsymbol{D}_w \boldsymbol{y} = 0$.

6.1.2 Reference Field Implementation

Another computationally complex algorithm is the IGRF reference field model required for the measurement update. A 16 bit fixed point Ada implementation was established based on a standard IGRF Fortran model. The algorithm was tested over a wide range of possible orbital positions and the results compared with results from a floating point implementation in Matlab. The errors committed by this low accuracy implementation were found to be approximately 30 nT (RMS) as shown in Figure 6.2. This is acceptable as the modeling error inherent to the IGRF model was found in Section 5.3.2.1 to be approximately 83 nT (RMS) when compared to data from Freja.
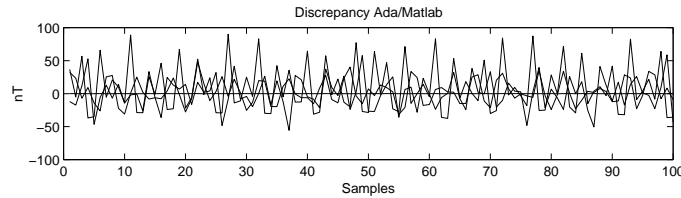
Figure 6.2: *On-board geomagnetic field model. Three components of the reference field in orbital positions distributed over 24 hours. Discrepancy between Ada fixed point implementation and Matlab 8th order model.*

6.1.3 ADS Implementation in Software

The Ørsted ADS has been implemented as a task running on one of the two on-board computers. The ADS software is executed as part of the central control level task. The interaction of the control level task with other ACS tasks is shown in Figure 6.3.

The control level task runs at a 10 second cycle that can be interrupted by a synchronous rendezvous with reconfiguration commands from a parallel running supervisor task. The preprocessed magnetometer readings are generated after an interrupt from the control level task and are transferred synchronously through rendezvous with an input dispatcher task that handles the interface to the other subsystems. The variables required for integrity monitoring and fault detection are transferred asynchronously from the control task to the supervisor task through a variable pool that is protected by a semaphore. The internal pa-
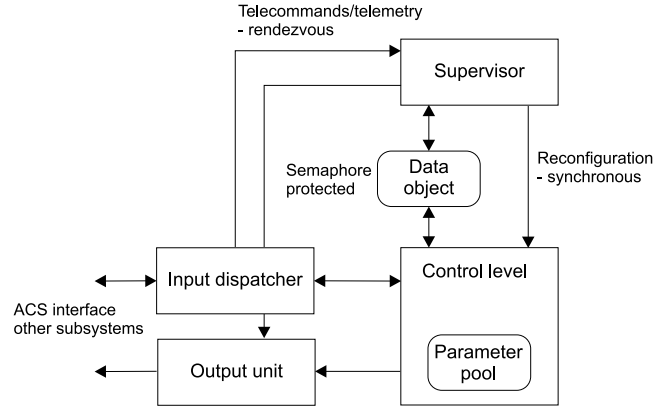
Figure 6.3: *Context diagram for the ACS main tasks.*

rameters of the ADS system are stored in a parameter pool inside the control level task and are available for modification through the supervisor.

The code size has been a major limiting factor in the development of the Ørsted ACS. Only 256 kbytes is available in a single on-board computer and only 65 kbytes were allocated for ACS. The code size of the specific modules relevant for the magnetometer based solution make up about 22% of the total ACS software as seen in Table 6.1.

Table 6.1: *Implementation - code size Ørsted ADS modules. The total magnetometer related ADS code is responsible for 22% of the total ACS code.*

Module	Code Size [kbyte]	
Attitude determination OBCS	1.46	
Observational update	2.17	
Time update	3.75	
State prediction	2.22	
Reference field model	2.24	
Utilities	2.18	
Total	14.02	22%
Total ACS software	64.60	

The module Attitude determination OBCS (Object Control Structure) executes the overall control of the ADS, which involves transitions between secondary (magnetometer) and primary sensors (star camera). The main burden is associated with the time update which involves the modules time update and state prediction. The module utilities provided services such as multiplication to the other modules. The total execution time of the ACS control task, which involve the attitude determination has been measured to 1.788 sec (Bøgh (1996). With a nominal cycle time of 10 seconds the ACS is hence responsible for about 18% of the computational load on the computer where the ACS software is running.

6.2   Results from Ørsted

With the launch of Ørsted on February 23, 1999, data are available for evaluation of the on-board estimation algorithm. Investigation are still ongoing, and the results presented here are considered preliminary.

As with most other satellites a number of difficulties have been discovered in relation to the flight configuration, many of which are yet unsolved. Of primary concern to evaluation of the ADS are the following

– *Boom distortion.* After deployment of the Ørsted boom significant discrepancy was found between the expected gondola and actual gondola orientation. A calibration based on Sun sensor and star camera data showed a 45 deg. rotation of the gondola relative to nominal. The ADS gondola to body rotation has been adjusted according to the calibration. The accuracy of the calibration is, however, limited due to the limited accuracy of the Sun sensors. This uncertainty is transferred to the ADS as uncertainty in the moments of inertia, and the control torque input. No explanation for this unexpected rotation has yet been found.

– *Boom flexibility.* When torques are applied to the satellite by the control system boom oscillations have been experienced at a frequency much lower than expected. Thermal effects also have an apparent influence. On the day side of the orbit boom oscillations are generated. Each upset of the boom (boom quake) is associated with a change in the boom stiffness, as seen on the eigenfrequency of the associated torsional vibrations (Bauer (1999)). Boom oscillations apparently cause star camera vibrations, and loss of star camera availability for a period of 20–40 sec. This phenomena may be coupled to the boom distortion and has so far not been fully

understood.

– *Star camera timing.* Timing problems with the star camera complicates the use of the star camera quaternion as a reference for evaluating the ADS. The timing problem has been solved, but data were only available for a very limited part of the mission at the time of writing. The analysis presented here is based on raw star camera attitude estimates.

– *Control system torques.* Current spikes in the magnetorquers combined with rapid changes in the current demands resulted in input torques that were problematic for the star camera. In combination with the boom oscillation phenomena the torque input caused the star camera to generate degraded estimates and eventually fall out. The problem was minimized by adjustments of star camera sensitivity and control system parameters, in particular the maximal allowed control current.

– *Unknown input torque.* The behaviour of the control system before boom deployment and during normal operation indicates some unknown disturbance torques. This assumption is supported by the analysis of the estimator performance discussed below.

The issues above all make the attitude determination task more difficult and the results presented in the next section are thus expected to be slightly worse than could be achieved. As the problems above are solved, the on-board filter will be adjusted accordingly and the errors may decrease somewhat.

6.2.1   Attitude Time Histories

Two different sets of orbits have been selected for an evaluation of the ADS performance. During the first six month of operation only approximately 30% good star camera data were available and the control of the satellite hence depended on the magnetometer based solution for a large part of the time.

The two sets presented here have been selected so that star camera data were available for comparison of the results. The first set represents a typical situation where the satellite is rotating slowly about the z axis, whereas set two represents the situation as it has been after some adjustments in late August 1999.

Orbits 2535-2538   The attitude estimated by the magnetometer based solution is compared with available star camera data. The results presented in Figure 6.4 are based on four orbits 2535-2538 (August 18 1999 UTC: 12:34:38).
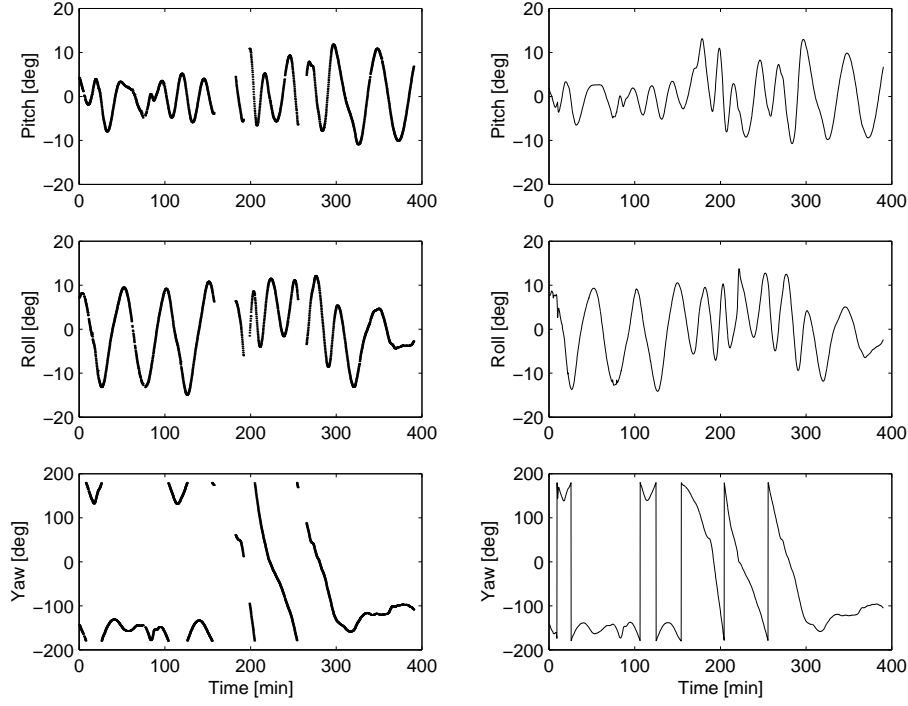
Figure 6.4: *Ørsted results from orbits 2535-2538 (August 18 1999 UTC: 12:34:38). Pitch/roll/yaw estimates from the star camera (left) and the estimates based on data from the magnetometer (right). The attitude is given relative to LVLH.*

The star cameras Sun and rate constraints are violated frequently causing gaps in the available star camera estimates. The control system converges towards the reference attitude of -90 deg. yaw. The rate of convergence may seem slow, but it is actually close to the 10 deg./min rate constraint of the star camera and clearly demonstrates the sensitivity of the star camera. The control gain in this specific case is reduced in order not to violate the star camera constraint.

The angular discrepancies between the ADS attitude and the star camera attitude associated with the attitude trajectories in Figure 6.4 are show in Figure 6.5.

The periodic components of the error trajectories are coupled to the periodic nature of the magnetic field. The errors in the three angles are determined to pitch: 1.5 deg. (RMS), roll: 1.5 deg. (RMS) and yaw: 3.7 deg. (RMS). The es-

Figure 6.5: *Ørsted results from orbits 2535-2538 (August 18 1999 UTC: 12:34:38). Pitch/roll/yaw discrepancies between star camera and magnetometer based estimates of the attitude.*

timation is thus less accurate than predicted in Chapter 5 but they are still within specifications. Some of the error is, however, attributed to the inaccuracies described above. The hope is with adjustment of the filter noise parameters to reduce the errors in the estimator. In addition, more accurate analysis of the star camera reference will be carried out in order the get a more accurate assessment of the absolute accuracy.

The satellite motion in Figure 6.4 is far from the reference and the rates are close to maximum for the star camera. From the truth model analysis in Chapter 5 we know that the error is larger, the larger the rates. The next set has therefore been selected to represent a situation where the attitude is close the reference.

Orbits 2539-2542   A typical situation, where the attitude control maintains a near -90 deg. attitude is given in Figure 6.6. The satellite pitch and roll angles are clearly within the 10 deg. specification and the z axis spin has stopped.

The corresponding error trajectories are found in Figure 6.7. The accuracy

Figure 6.6: *Ørsted results from orbits 2539-2542 (August 18 1999 UTC: 19:07:56). Pitch/roll/yaw estimates from the star camera (left) and the estimates based on data from the magnetometer (right). The attitude is given relative to LVLH.*

for this more controlled situation improves a little. The errors in the three angles are determined to pitch: 0.9 deg. (RMS), roll: 1.2 deg. (RMS) and yaw: 3.1 deg. (RMS).

The accuracy of the rate estimate has not been addressed yet, as timing problems with the star camera prevents accurate reference estimates of the star camera based rate.

Although the accuracy of the magnetometer based ADS solution is somewhat lower than anticipated it is within specifications and it has proved valuable at numerous occasions. One of the problems encountered during the first 6 month of Ørsted operation has been the sensitivity of the star camera to attitude control
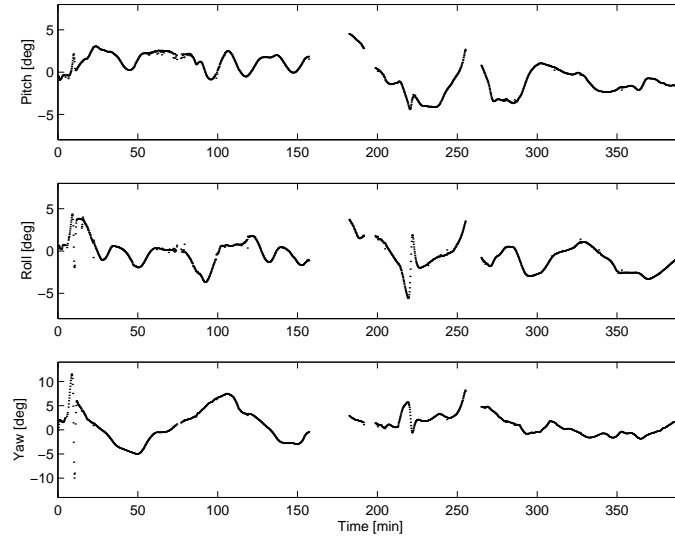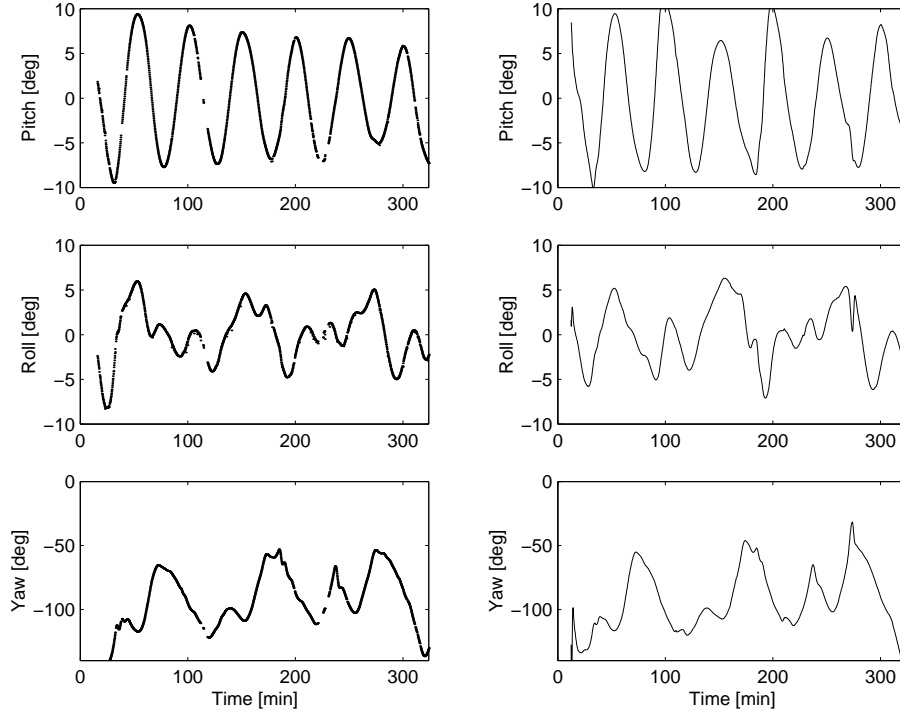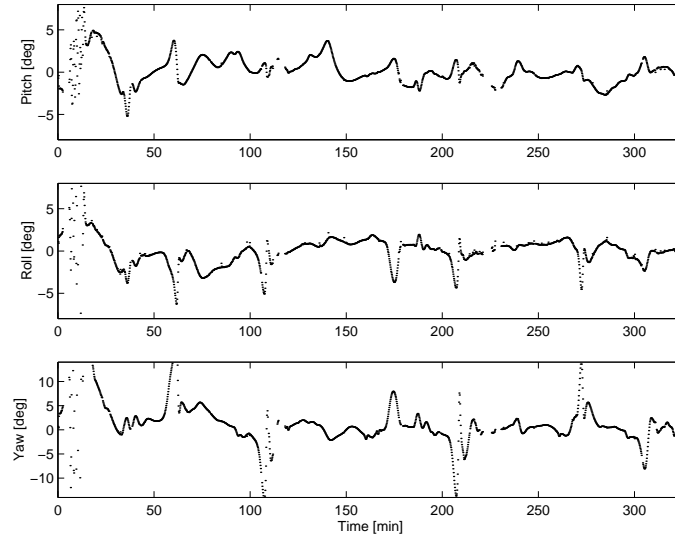
Figure 6.7: *Ørsted results from orbits 2539-2542 (August 18 1999 UTC: 19:07:56). Pitch/roll/yaw discrepancies between star camera and magnetometer based estimates of the attitude.*

action as described above. After a boom quake initiated loss of star camera data, the eventual close down and later re-activation of the ACS generated torques that resulted in a slow spin of the satellite. This has now been adjusted in the ACS. At spin rates above 10 deg./min the magnetometer based attitude estimate was the only available attitude and rate source. The controller has effectively stabilized the satellite and lowered the rates using the magnetometer based ADS estimates.

6.3 Summary

This chapter addressed the numerical implementation of the core algorithms in the Ørsted ADS and presented flight results from Ørsted. In Section 6.1 a factorized version of the Kalman filter equations was presented. The measurement update was based on Bierman's *Square Root Free* square root observational update, which was combined with Thornton's *modified weighted Gram-Schmidt algorithm* for time update. A short introduction to the software development was given. It was argued that the code directly related to the magnetometer solution

is responsible for less than 22% of ACS code.

Finally Section 6.2 presented preliminary results from the Ørsted ADS. The magnetometer based ADS was evaluated by comparison with available attitude estimates from the star camera. The accuracy was found to be lower than expected, but the hope is with adjustment of the filter noise parameters and more accurate analysis to get results that are more in line with the predicted results. The preliminary results from Ørsted do, however, meet the 2 deg. pitch/roll and 4 deg. yaw (1 sigma) error specification.

Chapter 7

Freja Attitude Estimation

The second application described in this thesis is an attitude estimation algorithm for the Freja satellite. The attitude is needed by the science mission to make off-line compensations of motion induced disturbances. At the present time only coarse, low rate attitude knowledge is available. A relatively high accuracy is required in order to fully utilize the science measurements.

This chapter presents the result of an effort to explore the use the extended Kalman filtering algorithms described in the previous chapters. The algorithms are applied to magnetometer flight data and attitude data reconstructed. A number of new issues had to be addressed in order to achieve the required accuracy. The solution presented here provides attitude estimates also during eclipse, where no reliable attitude was previously available. The results in this chapter were published in Bak (1998*b*), and Bak (1998*a*).

The chapter is divided into five sections and a summary. Section 7.1 gives the motivation for addressing the Freja problem and outlines the previous attitude estimation attempts and their limited usefulness. Section 7.2 address the required accuracy and the implications for a potential estimator design. Section 7.3 deals with the solution approach and Section 7.4 gives a brief description the filter design, batch interval selection and filter tuning. Finally, Section 7.5 discusses the perspective for attitude reconstruction applied to the satellite Astrid-2.

7.1 Motivation and Related Work

The Freja spacecraft was launched on October 6, 1992, and delivered approximately 200 megabytes of data each day until science observation ended in June

1995. The main scientific objective was related to the auroral acceleration processes. The satellite images the aurora and measures particles and fields in the upper ionosphere and lower magnetosphere (Andre (1993)). The Swedish Space Corporation (SSC) was the prime contractor to the Swedish National Space Board. The seven instruments on-board were built by groups in Sweden, Germany, Canada and the United States. Of particular interest here are the Auroral imager, the thee-axis magnetometer, the sun sensor and the electric field probe wire booms, all depicted on Figure 7.1.
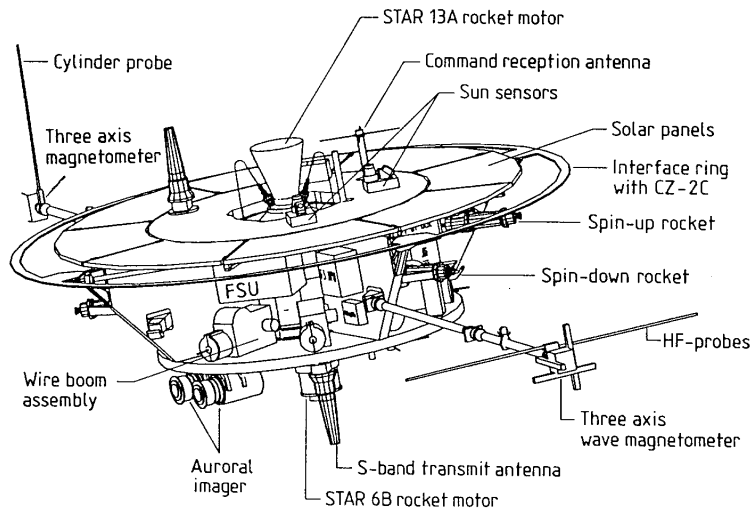
Figure 7.1: *The Freja satellite.*

The fundamental operational parameters of Freja are summarized in Table 7.1. As seen in Table 7.1 Freja is spin stabilized using the well–known quarter–orbit magnetic torquing attitude control method (Wertz (1978)) in order to track the Sun. The actuation is based on two torquer rods with a maximum dipole moment of 140 Am^2. One rod is aligned with spin axis, and the other is in the spin plane thereby allowing precession and spin control respectively. A nutation damper is used to dissipate the nutational energy, and thus reduce the nutation angle. To meet the attitude control pointing requirements (± 30 deg. Sun angle) the attitude was determined once or twice per orbit using deterministic methods based on the Sun sensor and attitude magnetometer.

Table 7.1: *Operational parameters of the Freja satellite. Freja was launched on October 7, 1992.*

Orbit	Inclination	63.0 deg.
	Apoapsis	1764 km
	Periapsis	596 km
	Epoch start date	1992.281 (07 Oct.)
	Eccentricity	0.08000
	Orbital period	109 minutes
Attitude	Stabilization	Spin stabilized
	Nominal spin period	10 RPM
	Control	Magnetic
	Orientation	Sun oriented (+/- 30 deg.)
Mass	Launch time	256 kg
	Payload	73.1 kg (including 21.6 kg booms and antennas)
Telemetry	Downlink stations	Esrange (Sweden), Prince Albert (Canada), Syowa (Antarctica)
	Downlink time/orbit	< 30 minutes at each station
	On-board storage	None
Power	Maximum power	137 W
	Payload usage	66.1 W

The attitude information was processed by the ground station and corrections to the spin vector, if necessary, were performed by telecommands. This solution proved sufficient in order to meet attitude control requirements.

7.1.1   Electric Field Experiment

The Swedish Alfvén Laboratory built the instrument measuring the electric field. The main scientific objective is related to the study the complicated phenomena of the electric fields in the ionosphere-magnetosphere transition region. Of special interest is the auroral region and in particular the night side auroral features. The basic quantity measured by the electric field experiment is the electric field, which is measured as the potential difference between opposing probes. Since the probes are in the spin plane an electric field is induced by the satellite spin. The induced electric field $\mathbf{E}_i = \mathbf{v} \times \mathbf{B}$ where $\mathbf{v}$ is the velocity of the probe, and $\mathbf{B}$ is the local magnetic field. This motion induced disturbance must be subtracted from the raw data before any analysis can be applied. In order to do so, the satellite spin axis pointing or attitude has to be known to an accuracy better than 0.2 deg. (1 sigma), (Blomberg, L. private communication, 1997).

The accuracy of the present single frame solution is unclear. More important, however, the single frame solution fails during eclipse when the Sun reference is not available. This is a major difficulty as a number of interesting phenomena in the polar ionosphere take place in the night-side auroral oval.

Determining the attitude based on interpolation of the single frame attitude solution before and after eclipse has proved problematic. The passage of the spacecraft in and out of eclipse complicates the problem. The decrease in temperature during orbit night cause the coil booms to shrink, shortening the booms radial distance to the spacecraft center of mass, thereby decreasing the moments of inertia.

An alternative solution is therefore needed that allow the estimation of a complete attitude time history during the polar cap passage. One approach that has been applied was based on the UV-imager. The ultra violet CCD camera was pointed towards the stars and a star identification algorithm combined with an attitude determination was applied. The results deviated significantly from attitude estimated for attitude control purposes. The UV-imager based attitude is, however, only available for six selected orbits.

7.1.2   A Magnetometer based Approach for Freja

Although the Freja satellite is fundamentally different from Ørsted, some of the same attitude estimation methods may still be applied. As demonstrated in the previous chapter, a single three axis magnetometer may provide us with valuable information about the spacecraft attitude state also during eclipse. Using the measured magnetic field data in an attitude solution will attribute any long periodic changes in the observed field to changes in the attitude of the spacecraft. As the main scientific interest is related to short periodic structures, the use of the same data for attitude estimation will not significantly affect the science measurements.

7.1.2.1   The Magnetic Field Experiment

Freja also flies a magnetic field experiment. The magnetometer is a triaxial core fluxgate sensor (Ballard and Hayes (1992) and Andre (1993)) mounted on a 2 meter boom, seen on the left in Figure 7.1.

The fluxgate type instrument senses all three components of the magnetic field with range of ± 65.000 nT and provides a resolution of 2 nT. The magnetic field vector is sampled at 128 Hz. Data is already part of the post processing of

the electric field measurements and thus available for attitude estimation.

A number of issues are new in the Freja problem compared to what was described in Chapter 5. The main challenge is the need for accuracy (0.2 deg. (1 sigma)) over the entire science observation interval. This accuracy requirement changes some of the issues discussed in relation to the Ørsted design and a number of the assumptions have to be re-addressed.

7.2 The Attitude Problem

The Freja problem is to estimate the three-axis attitude time history $\mathbf{q}(t)$ during science observation. The attitude quaternion parameterizes the transformation from inertial coordinates to spacecraft body coordinates. The basic input is the science magnetometer measurement. As science data is investigated off-line in batches, the attitude estimation may be treated as a smoothing problem. The attitude estimate at a given instant can hence be based on data that fall both before and after that time.

7.2.1 Magnetometer Calibration

Calibration of the magnetometer may possibly be carried out directly as part of the estimation process, but off-line parameter identification of sensor sensitivity, bias, orthogonality, misalignment may help simplify the estimator design significantly. Moreover all these issues have previously been addressed in the as part of the magnetic field experiment (Luehr (1997)) and we could take advantage of these earlier results.

Magnetometers are inherently nonlinear devices and an accurate calibration of the magnetometer is required to get to the specified accuracy (Freja 2 nT). The calibration converts the raw engineering units measured by the instruments into field components in nT along three orthogonal Cartesian coordinate axes. The calibration may be carried out in a coil facility prior to launch. Stress during launch and operation in the space environment may, however, significantly change the instrument transfer function, and an in-flight calibration is therefore normally required.

Luehr (1997) has showed that a complex non-linear in-flight calibration of the magnetometer is necessary in order to get to the 2 nT noise level. This noise level is well below the 0.2 deg. accuracy requirement and a simple linear

approach has been taken. The result is a calibration according to

$$\mathbf{B} = \mathbf{M}(\boldsymbol{EU} + \mathbf{b}) \tag{7.1}$$

where $\boldsymbol{B}$ is the measured field in nT, $\boldsymbol{M}$ is the 3×3 orthogonality and sensitivity correction matrix, $\boldsymbol{EU}$ is the raw measurement vector in engineering units, and $\boldsymbol{b}$ is a bias vector in engineering units. All parameters are estimate based on a least square fitting.

The magnetic field vector measurement is made in the magnetometer assembly coordinate system, where the z-axis was designed to be parallel to the satellite spin axis and the other two axes lie in the spin plane. It was found, however, that a correction on the order of a few tenths of a deg. was necessary for the alignment of the instrument.

This correction was implemented as follows: First, the x- and y- axis measurements were fitted with a sinusoidal wave with a shifted baseline and a linearly-varying envelop. The satellite spin period is determined from the oscillation period of these two components, whereas the cross-component phase lag gives the information about the angle between the x and y axes. The ratio between the x/y-component offset to the z-component measurement provides an inclination of the z-axis from the satellite spin axis.

Based on those results the measured magnetic field vector is rotated from the instrument assembly frame to the spacecraft body frame.

7.2.2 Reference Model Accuracy

While the calibration is carried out off-line and thereby simplifying the estimator design, the accuracy of the reference model has to be addressed directly in the estimator design.

One of the science objectives of Freja and of the electric field experiment in particular is the investigation of field aligned currents that are present in the auroral region. The field aligned currents results in magnetic perturbations perpendicular to the main field. As the Freja orbit goes through the auroral oval these perturbations may significantly vary in magnitude from fractions of a nT to thousands of nT Langel (1987). When using the magnetometer data in an attitude solution, periods with large perturbations must be avoided as these perturbations would otherwise influence the attitude estimates. As it will be shown later in this chapter, perturbations in the order of 300 nT may occur, which if attributed to attitude changes, would result in attitude errors as large as $\mathrm{arctan}(300/30.000) = 0.6$ deg..

In order to avoid this *contamination* of the attitude estimation, these perturbations to the field must be detected by the attitude determination system and the measurements must be rejected or corrected before being applied in the attitude estimator. When measurements are rejected the propagation will have to be based on an accurate dynamic model between measurement updates as no gyros are available.

7.2.3 Accuracy of Dynamic Model

The need for 0.2 deg. accuracy combined with possible propagation over contaminated data gaps emphasizes the need for an accurate dynamic model. Passage of the spacecraft in and out of eclipse further complicates the problem. Presumably the temperature change cause the coil booms to shrink when they cool down during orbit night shortening the booms radial distance to the spacecraft center of mass, thereby decreasing the moments of inertia. An simple propagation of the spin frequency through the day/night transition will hence not work. Assuming zero torques on the spacecraft, the angular momentum is known to be constant during such a transition, and any change in spin frequency may be referred to the a change in the moments of inertia about the spin axis.

An additional effect to shrinking of the booms, is that heat dissipation in the booms due to bending will cause the system to lose energy. This drift is, assumed negligible during the relative short time intervals considered here.

The inherent magnetic residual in the spacecraft was minimized during design, to reduce disturbances on the measurements. Magnetically induced torques are therefore assumed negligible.

7.3 Estimator Design

The attitude reconstruction problem has been solved using an estimator similar to the one developed for Ørsted. The estimator maintains an accurate dynamic model of the spacecraft, which is used to propagate the attitude and angular velocity estimates through the data gap. The dynamic model propagation is based on estimates of the on-orbit spacecraft inertias. The thermally induced changes in the moments of inertia are estimated through a parameter in the filter, thereby conserving angular momentum. Updates of the model are performed whenever *reliable* magnetometer data are available. The data gaps are identified using the a residual monitoring algorithm described below.

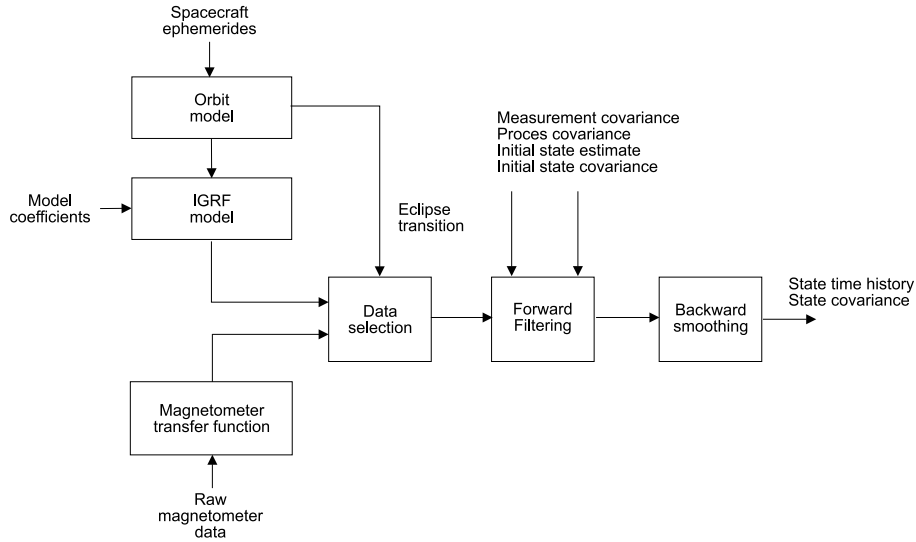The general outline of the solution is given in Figure 7.2.

Figure 7.2: *Attitude determination solution. Inertial magnetic field vectors from the IGRF model are combined with measured vectors in a forward filtering pass. The state estimate is improved by backward smoothing of the covariance and state.*

The spacecraft position is estimated using ephemerides data from standard NORAD two line elements. The IGRF model provides an estimate of the Earth's magnetic field given the satellite position in the ECEF frame. An IGRF main field model of order 10 was used, for the year as given in the navigational data.

Forward filtering was performed on the reference and measurement data combined with estimates of the measurement covariances, the process noise and initial states. The filter also uses input about eclipse transition in order to control the inertia estimation. Data is subsequently run through a smoothing algorithm.

7.3.1 Smoothing

The smoothing problem consists of the construction of the best estimate of the state of the satellite over a time period using all reliable measurements in that interval.

Let an estimate of the initial state at t_0 be given and denote it by $\hat{\boldsymbol{x}}_0$. The error in this initial estimate is assumed to be Gaussian with zero mean and co-variance $\boldsymbol{P}_0$. The filtered estimate at time t_j is designated by $\boldsymbol{x}_j^F$. Given is a set of discrete measurements $\{\boldsymbol{z}_k \mid k = 1, ...N\}$, we process the measurements se-quentially forward in time and produce the sequence $\{\hat{\boldsymbol{x}}_k^F, \boldsymbol{P}_k^F, k = 1, \ldots, N\}$. The smoothing algorithm produces the sequence $\{\hat{\boldsymbol{x}}_k^S, \boldsymbol{P}_k^S, k = N, \ldots, 1\}$, with the initial smoothed estimate at N being provided by the filtered estimate at N.

Forward Filtering Pass   The magnetic field observations are processed in a forward pass using the Kalman filter described in Chapter 4.

The thermally induced variations in moments of inertia are known to be cor-related with the day/night and night/day transitions. In order to allow the filter to track these inertia changes, the noise model is synchronized with the eclipse transitions. After an eclipse transition, the inertia covariance is reset to its origi-nal value and a new constant bias is estimated.

Backward Smoothing   The smoothing algorithm is based on the Rauch-Tung-Striebel (R-T-S) fixed interval smoothing algorithm (Rauch *et al.* (1965)).

During the forward filtering the intermediate results $\hat{\boldsymbol{x}}_{k|k}$, $\boldsymbol{P}_{k|k}$, $\hat{\boldsymbol{x}}_{k|k-1}$, $\boldsymbol{P}_{k|k-1}$ and $\boldsymbol{\Phi}^T(t_k, t_{k-1})$ are stored at each time t_k. The smoothing pass runs backward in time from the time t_N of the last measurement, computing the smoothed state estimate from the intermediate results. The smoothed state esti-mate and its covariance are initialized with the a posteriori values

$$\hat{\boldsymbol{x}}_N^s \;=\; \hat{\boldsymbol{x}}_{N|N} \tag{7.2}$$

$$\boldsymbol{P}_N^s \;=\; \boldsymbol{P}_{N|N} \tag{7.3}$$

The smoothed estimates are then computed recursively using

$$\boldsymbol{K}_k \;=\; \boldsymbol{P}_{k|k}\boldsymbol{\Phi}^T(t_k, t_{k-1})\boldsymbol{P}_{k+1|k}^{-1} \tag{7.4}$$

$$\hat{\boldsymbol{x}}_k^s \;=\; \hat{\boldsymbol{x}}_{k|k} + \boldsymbol{K}_k\left(\boldsymbol{x}_{k+1}^s - \hat{\boldsymbol{x}}_{k+1|k}\right) \tag{7.5}$$

7.3.2   Process Model

The filter error state vector is composed of the vector part of the inertial to body attitude quaternions and the three angular rate corrections. To account for ther-mally induced perturbation to the maximum moment of inertia, a perturbation to the spin axis moment of inertia is included in the state vector

The result is a 7 dimensional perturbational state vector

$$\Delta \boldsymbol{x}_f = \begin{bmatrix} \Delta \boldsymbol{q}^T \ \Delta \boldsymbol{\omega}^T \ I_3 \end{bmatrix}^T \tag{7.6}$$

where $\boldsymbol{\omega}$ are the inertial body rates represented in the body frame. The full quaternion $\boldsymbol{q}$ parameterize the rotation from inertial to the body frame. I_3 is the maximum (spin axis) moment of inertia. The perturbation to the maximum principal moment of inertia is used to model the thermally induced inertia variations. Such a model automatically conserve angular momentum and it was found to be required in order to propagate the attitude and rate estimates accurately through data gaps.

The vehicle attitude process model follows the equations derived in Chapter 3 with small modifications due to the inclusion of the extra inertia state and the fact that the Freja attitude is given relative to inertial space.

The variable I_3 is estimated using a bias model that is a random constant generated as the output of an integrator with no input, thus

$$\frac{d}{dt} I_3(t) = 0 \tag{7.7}$$

The initial condition is specified by the mean I_{30} and the variance P_{i0}. The selection of this kind of model is based on the assumption that the inertia is unknown but constant over the interval under investigation. The filter will use initial data to estimate the constant and eventually disregard all later measurements. After an eclipse transition, the filter is reset, and the filter will use the new measurements to converge to a new constant value, which hopefully represents the modified moment of inertia. The measurement formulation follows the Ørsted measurement model.

The initial full state estimates are derived from the coarse attitude data available in the present attitude history files, and is set equal to

$$\boldsymbol{q}_0 = [-0.4629,\ 0.0873,\ -0.7739,\ 0.4233]^T \tag{7.8}$$

$$\boldsymbol{\omega}_0 = [0,\ 0,\ 1.0811]^T \tag{7.9}$$

$$\boldsymbol{I}_0 = \begin{bmatrix} 95.392 & 0 & 0 \\ 0 & 81.335 & 0 \\ 0 & 0 & 159.679 \end{bmatrix} \tag{7.10}$$

The measurement noise model has been addressed previously in Section 5.3.2.1 while the process noise intensity were found empirically to obtain

filter/smoother measurement residuals that are consistent with the sensor accuracies. The Ørsted P1 process noise model (see Section 5.4.1) has been adopted, while omitting the inertia uncertainty. In this case the inertias are calibrated inflight. The final noise strengths and parameters defining the Freja process and measurement models are summarized in Table 7.2.

Table 7.2: *Parameters defining the spectral densities of the process noise as well as the measurement noise covariance for Freja.*

	Parameter			**Unit**
i	1	2	3	
$\boldsymbol{Q}_q$	0.5×10^{-8}	0.5×10^{-8}	2.0×10^{-8}	
$\boldsymbol{Q}_w$	1.7×10^{-13}	1.7×10^{-13}	1.2×10^{-16}	rad/sec^2
P_{i0}	1.0	-	-	kgm^2
$\boldsymbol{R}_m$	20^2	20^2	20^2	nT^2
$\boldsymbol{R}_b$	2^2	2^2	2^2	nT^2

7.4   Performance Analysis

The starting point for analysis of the Freja data is raw magnetometer data from an orbit interval. The interval was selected by the researchers at Alfvú laboratory as especially interesting. The measurements are collected during a passage through the auroral oval, as seen in by the ground track plot in Figure 7.3.

Data available from this specific pass are illustrated in Figure 7.4. Data is preprocessed as part of a magnetometer calibration described above.

In orbit 7281, the spacecraft attitude is nicely aligned with the spin axis, perpendicular to the field lines. The field vector hence rotates in the spacecraft xy plane. During this specific data interval the satellite is in eclipse, while the latest deterministic attitude was estimated in the Sun. The spin inertia is thus expected to have decreased, resulting in a faster satellite spin than estimated in the attitude files.

Figure 7.4 indicates some of the problems when using the magnetic field as a reference vector. The field is clearly disturbed in the part of the orbit from approximately 05:17 to 05:22. The phenomenon is caused by field aligned currents that generate a perturbation to the field perpendicular to the main field (Luehr (1997)). The field strength is clearly not influenced. Freja first encounters a downward current associated when it enters the auroral region at approximately
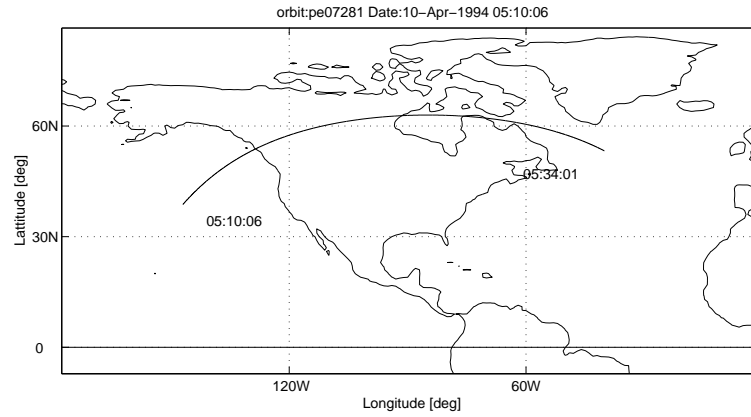
Figure 7.3: *Freja passage over the auroral oval. Orbit 7281, data from Prince Albert and Esrange ground stations.*
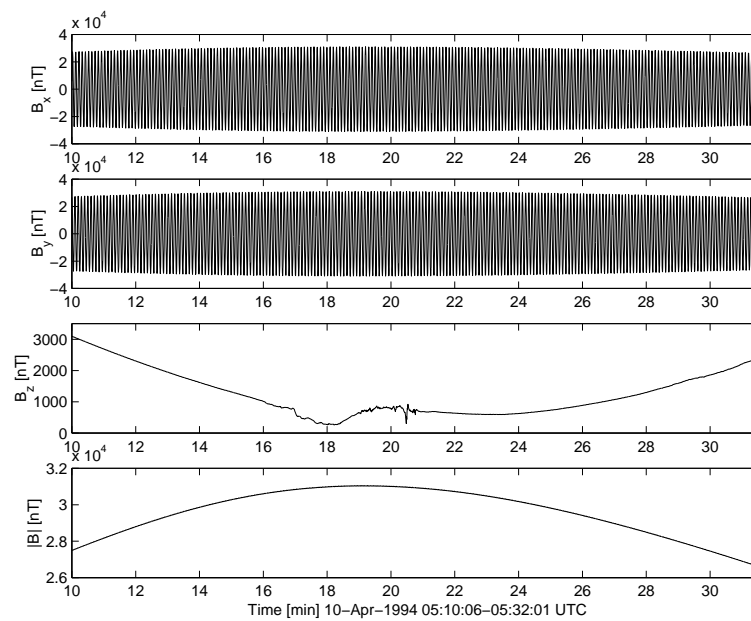

Figure 7.4: *Magnetic field measured by Freja F2 magnetometer, orbit 7281. The figures show the magnetic field projected onto the x, y and z axis of the magnetometer and the field strength.*

05:17. At approximately 05:19 it encounters a discontinuity, at which the field signature changed rapidly. The discontinuity occurs within a region of upward current. Finally Freja leaves the auroral oval at approximately 05:21.

Applying the filter directly the measured field with an error of 300 nT results in an error of approximately $\mathrm{atan}(300/30000) = 0.6$ deg.. The problem is solved selecting a batch interval outside this region. The result is a data gap, where the state estimation will have to be based on integration of the equations of motion of the spacecraft.

Assuming that field aligned currents cause the phenomena seen in Figure 7.4 the disturbance to the main field is mainly perpendicular to the spin axis. In the case in Figure 7.4 this would leave the x and y components of the measurements invariant, and they could be used in the filter. The attitude is, however, not always as nicely aligned as in Figure 7.4 and the estimator is hence designed with no measurement updates in the disturbed region.

It is evident that in order to automate the estimation process and at the same time get the required accuracy, disturbance detection is necessary. A simple test based on the log-likelihood ratio is proposed and applied in the following.

7.4.1   Attitude Reconstruction Results

The filter/smoother output includes several types of data that illustrate its performance. The measurement residual time histories indicate the filter/smoothers ability to fit the data. The attitude time histories illustrate the general state estimate.

Figure 7.5 shows the estimated and measured field measurements for the 7281 orbit.

Measurement Residual Time Histories   The measurement residual vector is $z_k - h(\hat{x}_{k|k}^s, t_k)$. The result should be a noise sequences with a RMS values less than or equal to the diagonal elements of the measurement noise covariance, R. If the process noise intensity were very small, then the measurement residual sequences would be almost white noise with RMS values approaching the diagonal elements of R.

Figure 7.6 shows the estimated F2 measurement residual time history.

The attitude is propagated from 05:16–05:24. The measurement residuals outside the data gap has RMS values are around 20 nT in the x and y components, which is in good agreement with the observation noise. A 20 nT error in the field components approximately correspond to an angular error of 0.04 deg.
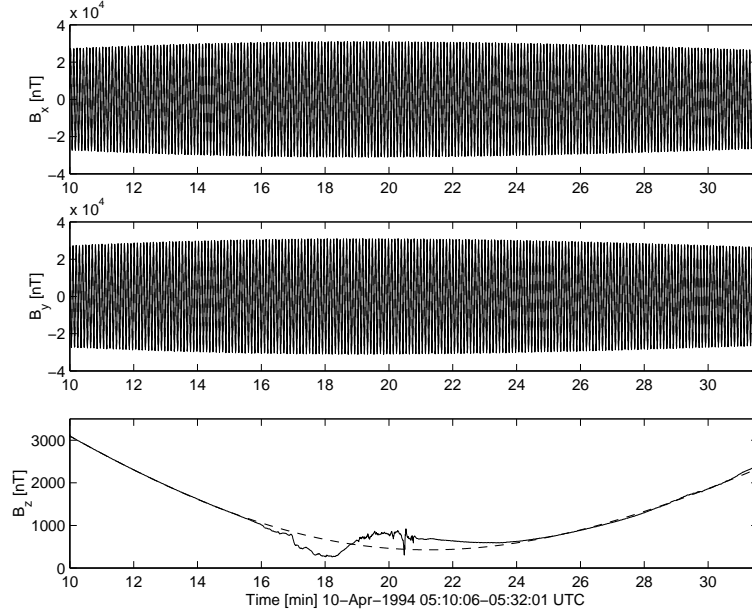
Figure 7.5: *Orbit 7281 – Estimated and measured magnetic field measurements.*

(RMS) in the determination of the spin phase. The error in the z-component is in around 2 nT (RMS) outside the data gap. The z component clearly demonstrates the perturbations to the main field, which is of interest for the magnetic field science investigators and they may be directly attributed to field aligned currents.

Around 05:30 the increased error indicate a perturbation to the field. This may very well be attributed to the morning auroral electrojet. Reasonable RMS noise levels indicates that the process noise is probably tuned correctly.

Note that the residuals in Figure 7.6 are not directly used in the magnetic field study. The important part is the state estimation, which is used in the correction of the motion induced electric fields.

7.4.1.1   Disturbance Detection

As mentioned above an automation of the disturbance detection is required in order to reject perturbed field measurements and thereby preserve accuracy. The
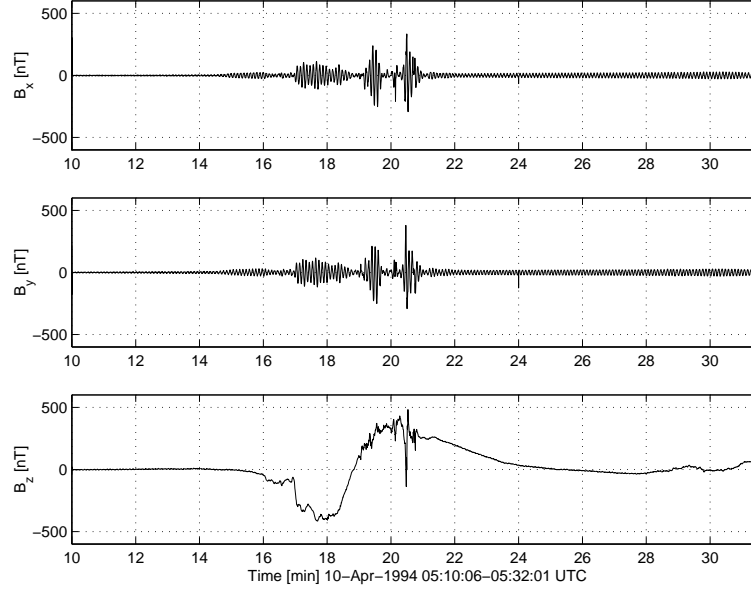
Figure 7.6: *Measurement residual time histories.*

results above are obtained using a CUSUM test outlined in the following.

The Detection Algorithm An increasing number of optimal likelihood function methods or ad hoc techniques for event detection are becoming available. Basseville and Nikiforov (1993) presents a very useful algorithm for detecting outliers called cumulative sum test (CUSUM). Essentially, the innovations are examined to determine whether they differ significantly from the statistical description of their values that assumes no failures.

If the innovations are assumed to be a set of Gaussian random variables the following hypothesis may be formulated

$$\begin{aligned}
\mathbb{H}_0 &\quad : \quad \nu(t) \in \mathcal{N}(\mu_0, \ \sigma_0^2) \\
\mathbb{H}_1 &\quad : \quad \nu(t) \in \mathcal{N}(\mu_1, \ \sigma_1^2)
\end{aligned}$$

where $\mathbb{H}_0$ represents fault free case and $\nu(t)$ are residuals. σ_0^2 is the estimate of the variance of the kth residual value based on the assumption that no failures have occurred. The value of $1/\sigma_0^2$ can be evaluated as the kth diagonal term

of $[\boldsymbol{H}_k \boldsymbol{P}_{k|k-1} \boldsymbol{H}_k^T + \boldsymbol{R}(k)]^{-1}$, which has already been calculated in the filter algorithm.

Statistical hypothesis testing theory indicates that a good choice of likelihood function for event detection is of the form of the log likelihood ratio. Let p_0 be the probability density of the residuals under hypothesis $\mathbb{H}_0$. A Sequential Probability Ratio Test (SPRT) between $\mathbb{H}_1$ and $\mathbb{H}_0$ is a comparison of the likelihood ratio

$$S_k = \ln \frac{p_1(r(0), \cdots, r(t_k))}{p_0(r(0), \cdots, r(t_k))}$$

against a threshold. Assuming an independent residual sequence, i.e. $p_i(r(0), \cdots, r(t_k)) = \prod_{n=0}^{k} p_i(r(t_n))$, the log-likelihood ratio term at time t_k may now be written as

$$s(t) = \ln\left(\frac{\sigma_0}{\sigma_1}\right) + \frac{1}{2\sigma_0^2}\Big(r(t) - \mu_0\Big)^2 - \frac{1}{2\sigma_1^2}\Big(r(t) - \mu_1\Big)^2 \qquad (7.11)$$

which is equivalent to a SPRT test based on $S_k = \sum_{n=0}^{k} s(t_n)$. This will show a negative drift before change, and a positive drift after change.

The following decision function can now be calculated recursively

$$g(t_k) = \begin{cases} g(t_{k-1}) + s(t_k) & \text{if } g(t_k) < \lambda, \\ \lambda & \text{if } g(t_k) \geq \lambda \text{ detection}, \\ 0 & \text{if } g(t_k) < 0. \end{cases} \qquad (7.12)$$

where $g(\cdot)$ is a cumulative sum initialized to zero, and λ is a threshold. In other words decide $\mathbb{H}_1$ whenever $g(t_k)$ exceeds λ, and $\mathbb{H}_0$ otherwise. This is a simple yet effective event detection algorithm.

Detection Results The threshold value was set to $\lambda = 100$ and both hypothesis are assumed zero mean. The variance of the $\mathbb{H}_0$ (no fault) is set to 10 nT, whereas the $\mathbb{H}_1$ variance is set to 100 nT. The z axis innovations and associated detection is shown in Figure 7.7.

The same fault detection scheme is also carried out on the x and y components, but as discussed previously the field aligned currents are mainly perpendicular to the field, and they are hence not as easily detected in B_x and B_y.

State Time Histories Plots of the attitude quaternion estimates are not very useful due to the rapid motion of the satellite. More useful are plots of the spin
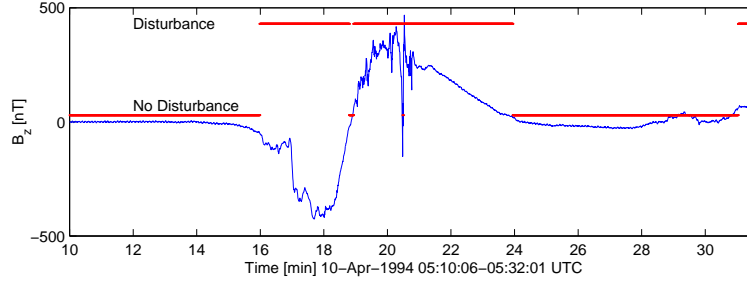
Figure 7.7: *Detection of magnetic disturbance by CUSUM log-likelihood test.*

vector direction versus time. The attitude is presented by the azimuth and declination of the spin axis in ECI. The results for orbit 7281 are given in Figure 7.8. The results are in good agreement with the estimated azimuth and declination given in the last Freja attitude file as shown in Table 7.3. There is a small drift in both azimuth and declination.

In addition to attitude information Figure 7.8 also presents the estimated inertia. The deviation from previous estimates made in the Sun is significant. The inertia converges rapidly from an initial estimate of 159.679 kgm^2 to 153.43 kgm^2. This is in good agreement with an increase in the spin of approximately 0.04 rad/sec.

Table 7.3: *Freja attitude information.*

Parameter	Attitude File	Estimated
Date	1994-04-08	1994-04-11
Time	04:30	05:10
Orbit	7254	7281
Azimuth	18.9 deg.	18.0 deg.
Declination	34.0 deg.	33.3 deg.
Spin rate	9.94 RPM	10.32 RPM
I_3	159.679 kgm^2	153.43 kgm^2

The effect of smoothing the estimates is most clearly seen by observing the estimated covariances in Figure 7.9. Figure 7.9.a presents the 2 times squared error covariance for the third quaternion element from the forward filtering of data. The covariance grows during the data gap, and it is reduced again as soon
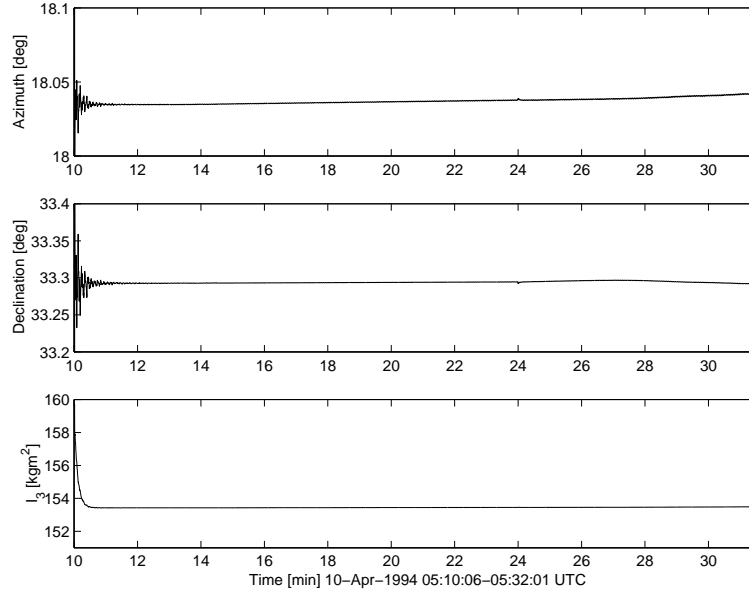
Figure 7.8: *Freja orbit 7281. Estimated spin axis azimuth and declination in ECI. Estimated spin axis inertia .*

as observations become available at 05:24. Figure 7.9.a illustrates the same situation after smoothing with data after the data gap. The results are clearly better, the covariance is reduced significantly during the data gap.

7.5 Perspective

The algorithm presented here is specially designed for the Freja mission and addresses some of the special issues related to Freja. The usefulness of the algorithm is, however, not limited to Freja, and another version of the algorithm is being worked on for the Swedish Astrid-2 mission. Astrid-2 was launched in December 1998. Due to problems with the star camera, an alternative magnetometer based algorithm is required that will allow the Electric field data to be extracted. Automation of an algorithm derived from the Freja results presented above is currently being implemented at the Danish Meteorological institute.
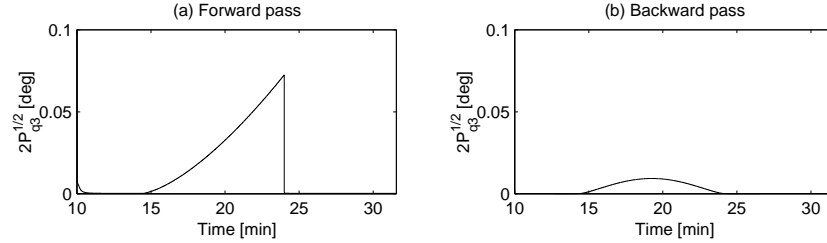
Figure 7.9: *Freja orbit 7281. Squared covariance estimate on q_3. (a) covariance after forward pass; (b) covariance after backward smoothing.*

7.6 Summary

The full use of Freja data electric field data required spacecraft attitude state estimates during the complete science observation phases. The motivation and problems associated with Freja were discussed in Sections 7.1 and 7.2.

Section 7.3 addressed the filter/smoother development and solution approach. The two main problems in the attitude reconstruction have been: 1) the lack of reliable magnetometer data during part of the orbit, when the science data is corrupted by the phenomena under investigation, and 2) thermal effects on the spin axis inertia, resulting in uncertainty in the spin rate.

Section 7.4 gave a brief description of the results achieved by processing Freja magnetometer data in a Kalman filter. In summary, the Freja attitude reconstruction algorithm has solved the initial science problem, getting accurate attitude estimates during eclipse. The filter is based on magnetometer data only combined with an accurate dynamic model. The field disturbances were detected using a CUSUM test and the attitude propagated during interval with perturbations to the main field.

Finally Section 7.5 discussed the use of a similar algorithm on data from Astrid–2.

Chapter 8

Conclusion and Recommendations

This thesis considered a number of aspects related to spacecraft attitude determination. The problem of estimating the attitude based on magnetometer measurements only was studied in detail. This chapter summarizes the work presented in this thesis. The main results are review and directions for further investigations are identified.

8.1   Conclusion

Theory and application was combined in this thesis. First some basic theoretical problems were addressed and at the end two real flight cases were investigated in detail. Results demonstrate the usefulness of magnetometer based solutions to attitude estimation, as a backup on small satellites demanding coarse attitude knowledge, or as a batch-processing reconstruction algorithm used in connection with a science mission.

The following conclusions are drawn on the accomplishments and contributions of this thesis:

– A general discussion of attitude representation was presented and the advantages of using a four component quaternion as rotation group specified was outlined. The quaternion provides a globally nonsingular two-to-one mapping of the rotation group. A unit norm constraint limits the number of independent parameters to one. An exponential series expansion of the

149

quaternion was presented, which may easily be truncated in linearization. It was argued that the series may be interpreted as a series of 4×4 skew symmetric matrices.

– An introduction to nonlinear attitude estimation based on Kalman filtering was given. It was demonstrated how temporal fusion of measurements makes full three-axis attitude determination possible with only one reference sensor.

– Consistency of the estimator in the presence of modeling errors was investigated. Given knowledge of the true system, limits on the noise statistics were established that prevents inconsistency of the estimator.

– The problems of preserving normalization of the quaternion and covariance singularity were demonstrated by use of the exponential quaternion series. The covariance singularity is numerically problematic, and a quaternion error approach was therefore taken that avoids the singularity by only estimating the three independent parameters in a first order approximation of the exponential series.

– An ADS design, where the magnetometer attitude estimate was used as a backup algorithm was presented. The result is a fault tolerant system, which enhance the autonomy of the Ørsted small satellite. Intense simulations based on a truth model has been carried out demonstrating the ability of the system to estimate attitude and rates with the required accuracy.

– Flight results from Ørsted demonstrates how a single magnetometer may provide us with valuable information about the state of the spacecraft. The use of a simple magnetometer combined with an attitude estimator has complemented the more sophisticated star camera and provided estimates of rate and attitude when the star camera constraints were violated. Due to boom oscillations and other problems this has frequently been the case over the first months of operation.

– Finally the Freja problem was addressed. The solution approach was outlined and the results evaluated against available reference data. The resulting estimator solved the problem of estimating the attitude during eclipse and data gaps. The filter state was augmented with an inertia state in order to facilitate accurate propagation during periods with perturbed field data.

Perturbations to the field were automatically detected by use of a statistical test. The accuracy of the solution solved the initial problem posed and enabled the compensation of motion induced disturbances on the electric science field measurements, thereby enhancing the Freja science mission.

8.2 Recommendations

The following topics are not covered in this work but it is believed that future investigations could be beneficial:

– With the advent of modern microprocessors, it has become increasingly possible to produce smart sensors in which the state estimation process is moved inside the sensor box. A typical example is the user segment of the GPS in which the receiver and navigation software are usually integrated into a single processor. The implementation of an attitude estimator with the magnetometer could be an interesting new application of the magnetometer based attitude determination.

– The Ørsted data give us valuable new data and a high accuracy reference, which will allow additional studies of magnetometer based solutions on real flight data. Problems with the Ørsted data are being addressed but a few problems related to the star camera timing and the boom oscillations remain open.

– The areas of nonlinear observers and differential geometry has in recent years received a lot of research interest. The results in these areas could possibly be transferred to the attitude estimation problem, yielding solutions (quaternions) that evolved on the S^3 manifold and thereby avoid the normalization problem entirely.

Appendix A

Coordinate Systems

This section describe the various coordinate systems applicable to this thesis:

Earth Centered Inertial (ECI) Coordinate System   Origin in the Earth's center. The xy-plane is parallel with the Earth's equatorial plane, the +x-axis is fixed in the direction of vernal equinox. +z is normal to the xy-plane in the direction of the north pole, and the y axis is formed by the cross product of z- and x-axes.
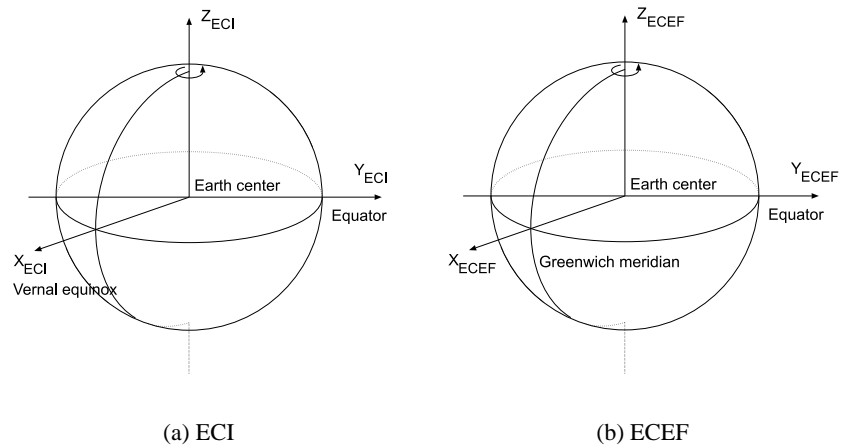

(a) ECI   (b) ECEF

Figure A.1: *Earth Centered Inertial (ECI) and Earth Centered Earth Fixed (ECEF) coordinate systems.*

Spacecraft Body (SCB) Coordinate System   Origin is defined in the space-craft structure and the frame is fixed to the spacecraft. The xy plane is defined by the interface plane where the satellite attaches to the launcher. The z axis is normal to the xy plane with the +z axis in the direction of the Ørsted boom, or the "boresight" of the solar array in the Freja case. The Ørsted y axis is per-pendicular to the long side of the main body, while the Freja y axis is along the magnetometer booms with +y defined in the direction of the F2 magnetometer. The x axis completes the orthogonal coordinate system. The Ørsted SCB system is given in Figure A.2(a) and the Freja SCB system in Figure A.2(b)

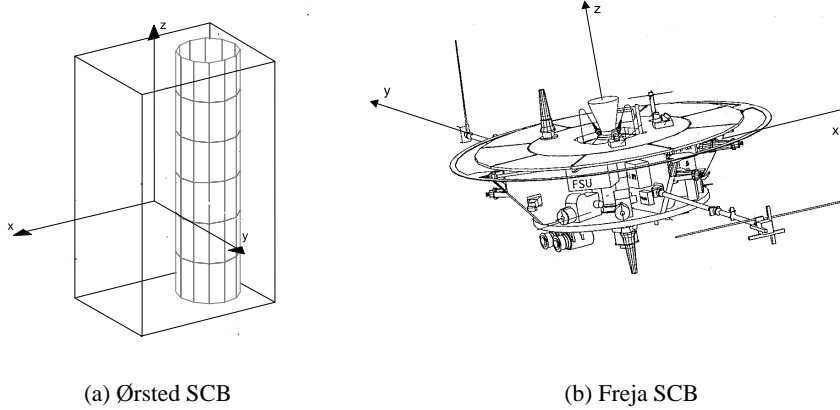(a) Ørsted SCB   (b) Freja SCB

Figure A.2: *Ørsted and Freja SCB coordinate systems.*

Principal (PCS) Coordinate System   Origin is in the center of mass of the spacecraft. The axes are defined by the principal axes of the spacecraft with the z axis aligned with the spin axis of the spacecraft. The x and y axes are perpendicular to the z axis. The rotation from SCB to P is implicit in this thesis.

Earth-Centered-Earth-Fixed (ECEF) Coordinate System   Origin is at the center of mass of the Earth. The xy-plane coincide with the Earth's equatorial plane, the +x-axis is fixed by the Greenwich Prime Meridian (GPM). +z is nor-mal to the xy-plane in the direction of the north pole, and the y axis is formed by the cross product of z- and x-axes, i.e. the y axis points 90 deg. to the east of
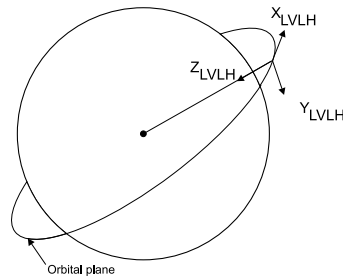
GPM.

Figure A.3: *Local Vertical Local Horizontal coordinate system.*

Local-Vertical-Local-Horizontal (LVLH) Coordinate System   Origin is at the center of mass of the spacecraft. The $+z$ axis (local vertical) is parallel to the radius vector, negative from the spacecraft center of mass to the center of Earth. The $+x$ axis is pointed in the direction of the angular momentum vector (perpendicular to orbit plane). The y axis (local horizontal) completes the orthogonal coordinate system. The $+y$ lies in the orbit plane in the direction of the negative velocity vector (only identical to the velocity vector for perfectly circular orbits). Note that this definition of LVLH deviates from traditional definitions.

Appendix B

Satellite and Space Environmental Models

B.1 Atmospheric Density Model

The Mass-Spectrometer-Incoherent-Scatter (MSIS-86) model describes the neutral temperature and densities in the upper atmosphere (above about 100 km). It is used to model the large periodic changes in the atmospheric density. MSIS-86 model an empirical model based on the extensive data compilation and analysis work of Hedin (1987) and his colleagues.

B.2 Orbit Propagation Models

General perturbations element sets generated by NORAD are used to predict position and velocity of the satellites. To do this one must be careful to use a prediction method which is compatible with the way in which the elements were generated.

Only ideal orbits describe true ellipses and have constant orbital elements. Real orbits experience both periodic and secular effects in their elements. Because of this, there are various ways of describing orbital elements. One way is to use osculating or instantaneous orbital elements, that is, the instantaneous values of each element at the specified epoch. The other is to use mean orbital elements.

NORAD maintains general perturbation element sets (Two Line Elements (TLE's) on all resident space objects. These element sets are periodically refined

so as to maintain a reasonable prediction capability on all space objects. In turn, these element sets are provided to users. The NORAD element sets are *mean* elements obtained by removing periodic variations in a particular way. In order to obtain good predictions, these periodic variations must be reconstructed in the same way they were removed by NORAD. Hence, inputting NORAD element sets into a different model (even though the model may be more accurate or even a numerical integrator) will result in degraded predictions. The NORAD element sets must be used with one of the models described in this report in order to retain maximum prediction accuracy.

The Special General Perturbation (SGP4) model generate predictions based on NORAD TLE's and at the same time allow quick calculations. The procedure to compute position and velocity state vectors for any desired time using SGP4 is well understood and detailed in Hoots and Roehrich (1980).

The basic perturbations that cause a satellite's path to deviate from an ideal Keplerian orbit result from

1. The non-spherical mass distribution of the Earth.

2. Atmospheric drag.

SGP4 apply these perturbational effects to orbits by the technique known as variation of parameters, where the parameters being changed are the orbital elements. If these effects were ignored and the orbit were propagated using 2-body (i.e., Keplerian) orbit theory, the error in the predictions would be apparent within the span of 2-3 hours.

The geopotential deviations from an *ideal* spherical mass distribution result in predictable changes to the orbit. The primary gravitational perturbational effects are on the orbital plane and the orientation of the orbit's apogee-perigee (or apsidal) line. The primary effects are "secular" in nature as they represent constant drift rates for the ascending node and the apsidal line as a function of time. The constant drift rates are a function of the semimajor axis, eccentricity, and inclination of the orbit. The secondary effects are periodic in nature and consist of both long- and short-term effects. The long term periodics are superposed on the secular effects. The short-term periodics, in turn, are superposed on the long-term periodic effects.

SGP4 uses a 4th order geopotential model which includes the equatorial bulge (2nd order) and the greater amount of mass in the southern hemisphere (3rd order). An additional mass deviation is included that is smaller than the second and third order deviations.

SGP4 use static methods to model the effects of atmospheric drag on satellite orbits. SGP4 models the density of the Earth's upper atmosphere using the fourth power of the orbital altitude. SGP4 applies drag effects to the orbit using a pseudo ballistic coefficient, normalized to the orbital altitude and current atmospheric density profile. The drag coefficients are usually empirically-fit (based on long-term behavior) in the orbit determination process.

B.2.1 Precision

The precision of the orbit propagation was verified against state vectors from the Solar Anomalous and Magnetospheric Particle Explorer (SAMPEX) spacecraft. The prediction based on mean elements stay well below 20 km error over a 15 days prediction interval when compared to the SAMPEX state vectors. The results of an example orbit are shown in Figure B.1.
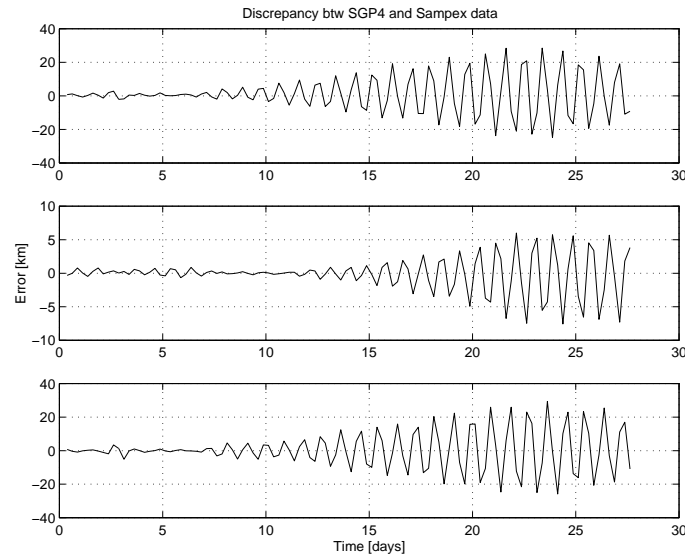

Figure B.1: *Discrepancy between SPG4 prediction based on TLE and actual state vectors from SAMPEX.*

The precision of the orbit prediction model, has only minor significance when used in the truth model. The analysis is, however, important when considering the on-board orbit model. The SAMPEX orbital state vectors were provided by

courtesy of H. Hoffmann, NASA Goddard Space Flight Center.

B.3   Geomagnetic Reference Field Model

As shown by Gauss in 1839, the main geomagnetic field (i.e., magnetic potential) can be represented by a spherical harmonic series, the first term being the simple dipole term. A gradient of the potential determines the magnetic vector field. The Earth's real magnetic field is the sum of several contributions including the main (core) field, the crustal (anomaly) field, and the external source (magnetospheric) fields.

The principal data sources for the main geomagnetic field modeling are the following:

– Permanent (standard) magnetic observatories worldwide

– Global satellite magnetic measurements

– Magnetic surveys from the aircraft and ships

Satellite data (MAGSAT and Dynamic Explorer 2) have also helped to evaluate the crustal (anomaly) fields at individual observatories and regions and have thus greatly enhanced the accuracy of observatory data for the main field modeling. Temporal variations of the internal field have been modeled by expanding the coefficients in a Taylor series in time. Most models include only the constant and first time derivative (secular variation) terms.

The International Geomagnetic Reference Field (IGRF) model is the empirical representation of the Earth's magnetic field recommended for scientific use by the International Association of Geomagnetism and Aeronomy. The IGRF model represents the main (core) field without external sources. They employ the usual spherical harmonics expansion of the scalar potential in geocentric coordinates. The IGRF model coefficients are based on all available data sources including geomagnetic measurements from observatories, ships, aircraft and satellites.

Bibliography

Andre, M., (Ed.) (1993). *The FREJA Scientific Satellite*. Vol. IRF Scientific Report 214. 3 ed.. Swedish Institute of Space Physics.

Bak, T. (1994). Attitude Determination Methods. Technical Report Ørsted Project TN-151. Aalborg University.

Bak, T. (1995). Onboard Models for Autonomous Attitude Determination. TN T03-06-021. Aalborg University.

Bak, T. (1996). Onboard Attitude Determination for a Small Satellite. In proc.: *Proceedings Third International Conference on Spacecraft Guidance, Navigation and Control Systems*. ESA.

Bak, T. (1997). The Autonomous Formation Flying (AFF) Sensor. Enginering memorandum. JPL.

Bak, T. (1998*a*). Attitude Reconstruction for FREJA, a Magnetometer based Approach. In proc.: *IFAC World Congress '99*.

Bak, T. (1998*b*). FREJA Attitude Estimation. Technical note R4246. Aalborg University.

Bak, T. and D. Bayard (1997). JPL Multipath Estimation Technique with a Generic GPS Receiver. Technical Report Enginering Memorandum, EM-3455-97-034. JPL.

Bak, T. and R. Wisniewski (1996). Passive Aerodynamic Stabilization of a low Earth orbit Satellite. In proc.: *Proceedings Third International Conference on Spacecraft Guidance, Navigation and Control Systems*. ESA.

Bak, T., H. H. Pedersen and C. Brøndum (1995). The Ørsted satellite with flexible boom. Master's thesis. Aalborg University.

Bak, T., R. Wisniewski and M. Blanke (1996*a*). Autonomous Attitude Determination and Control System for the Ørsted Satellite. In proc.: *IEEE Aerospace Application Conference*.

Bak, T., R. Wisniewski and M. Blanke (1996*b*). Gso-l: Assessment of attitude dynamics. In: *In ESA study on Geomagnetic Space Observatories* (Torsten Neubert, Ed.). DMI/GSO/RPT/005.

Ballard, B. and J. Hayes (1992). FREJA F2 Magnetic Field Experiment Software Requirements. Technical report. JHU/APL.

Bar-Itzhack, I. Y. (1996). REQUEST: A Recursive QUEST Algorithm for Sequential Attitude Determination. *Journal of Guidance, Control, and Dynamics* **19**(5), 1034–1038.

Bar-Itzhack, I. Y. and R. R. Harman (1997). Optimized TRIAD Algorithm for Attitude Determination. *Journal of Guidance, Control, and Dynamics* **20**(1), 208–211.

Bar-Itzhack, I. Y., L. Markley and J. Deutchmann (1991). Quaternion Narmalization in Additive EKF for Spacecraft Attitude Determination. In proc.: *Flight Mechanics/Estimation Symposium*.

Bar-Itzhack, I.Y. and Y. Oshman (1985). Attitude Determination from Vector Observations: Quaternion Estimation. *IEEE Transaction on Aerospace and Electronic Systems* **21**(1), 128–135.

Bar-Shalom, Y. and T.E. Fortmann (1988). *Tracking and Data Association*. The Academic Press.

Basseville, M. and I.V. Nikiforov (1993). *Detection of Abrupt Changes: Theory and Application*. Prentice Hall. New Jersey.

Bauer, Peter (1999). Analysis of thermal effects on the Ørsted science data. Preliminary Report.

Bøgh, S. A. (1996). ACS Benchmarking. Ørsted/TN 331. AAU. Aalborg University.

Bøgh, S. A. (1997). Fault Tolerant Control Systems - a Development Method and Real-life Case Study. PhD thesis. Aalborg University.

Bøgh, S. A., R. Wisniewski and T. Bak (1997). Autonomous Attitude Control System for the Ørsted Satellite. In proc.: *Proceedings of the IFAC Workshop on Control of Small Spacecraft, Breckenbridge, USA, Feb. '97.*

Bierman, G. J. (1977). *Factorization Methods for Discrete Sequential Estimation*. Vol. 128 of *Mathematics in Science and Engineering*. Academic Press.

Blanke, M. (1995). Aims and Tools in the Evolution of Fault-tolerant Control. In proc.: *ESF COSY Workshop, Rome.*

Bøgh, S. A., R. Izadi-Zamanabadi and M. Blanke (1995). Onboard Supervisor for the Ørsted Satellite Attitude Control System. In proc.: *5th ESA workshop on Artificial Inteligence and Knowledge Based Systems for Space.*

Bryson, A. E. (1994). *Control of spacecraft and aircraft*. Princeton university press.

Bucy, R.S. and P.D. Joseph (1968). *Filtering for Stochastic Processes, with Applications to Guidance*. Wiley. New York.

Challa, M. S. (1993). Solar, Anomalous and Magnetospheric Particle Explorer (SAMPEX) REal-Time Sequential Filter (RTSF). Evaluation report. NASA Goddard Space Flight Center.

Challa, M., S. Kotaru and G. Natanson (1997). Magnetometer-only Attitude and Rate Estimates During the Earth Radiation Budget Satellite 1987 Control Anomaly.

Chevalley, C. (1946). *Theory of Lie Groups*. Princeton University Press.

Clarke, D. S., M. T. Hicks, A. M. Fitzgerald, J. J. Suchman, R. J. Twiggs, J. Randolf and T. W. Kenny (1996). Picosat Free Flying Magnetometer Experiments. In proc.: *10th Anual AIAA Small Satellite Conference.*

Cohen, C. E. (1992). Attitude Determination Using GPS. PhD thesis. Stanford University, Department of Aeronautics and Astronautics.

Crassidis, J. L. and F. L. Markley (1997*a*). Minimum Model Error Approach for Attitude Estimation. *Journal of Guidance, Control, and Dynamics* **20**(6), 1241–1247.

Crassidis, J. L. and F. L. Markley (1997*b*). Predictive Filtering for Attitude Estimation Without Rate Sensors. *Journal of Guidance, Control, and Dynamics* **20**(3), 522–527.

Deutchmann, J., R. Harman and I. Bar-Itzhack (1998). A Low Cost Approach to Simultaneous Orbit, Attitude, and Rate Estimation Using an Extended Kalman Filter. In proc.: *AAS/GSFC 13th International Symposium on Space Flight Dynamics* (Tom Stengle, Ed.). Vol. 2. pp. 667–676.

Eisenman, A., C. C. Liebe and J. Jørgensen (1996). Astronomical Performance of the Engineering Model of Ørsted Advanced Stellar Compass. In proc.: *Space Sciencecraft Control and Tracking in the New Millennium* (E. Kane Casani and Mark A. Vander Does, Eds.). pp. 252–264.

Fisher, H. L., M. D. Shuster and T. E. Strikwerda (1989). Attitude Determination for the Star Tracker Mission. In proc.: *AAS/AIAA Astrodynamics Conference*. Orlando, Florida. pp. 139–150.

Flatley, T. W., J. K. Forden, D. A. Henretty, E. G. Lightsey and F. L. Markley (1990). On-board Attitude Determination and Control Algorithms for SAMPEX. In proc.: *Flight Mechanics/Estimation Theory Symposium*.

Gai, E., K. Daly, J. Harrison and L. Lemos (1985). Star-Sensor-Based Satellite Attitude/Attitude Rate Estimator. *Journal of Guidance, Control, and Dynamics* **8**(5), 560–565.

Goldstein, H. (1950). *Classical Mechanics*. Addison-Wesley. Reading, Massachusetts.

Grewal, M. S. and A. P. Andrews (1993). *Kalman Filtering, Theory and Practice*. Information and System Science Series. Prentice Hall.

Hamilton, W. R. (1866). *Elements of Quaternions*. Longmans, Green. London.

Handschin, J. E. (1970). Monte Carlo Techniques for Prediction and Filtering of Non-linear Stochastic Processes. *Automatica* **6**(4), 555–563.

Hedin, A. E. (1987). MSIS-86 Thermospheric Model. *J. Geophys. Res. 92*.

Hoots, F. R. and R. L. Roehrich (1980). Models for Propagation of NORAD Element Sets. Technical report. Spacetrack report no.3.

Hughes, P. C. (1986). *Spacecraft Attitude Dynamics*. Wiley and Sons, Inc.

ISSD (1999). Internet supported space database, http://issd.zarm.uni-bremen.de/. University Of Bremen, Germany.

Jakubczyk, B. and W. Respondek (1999). *Geometric Nonlinear Control*. Lecture notes, Aalborg University, Department of Control Engineering. Aalborg, Denmark.

Jazwinski, A. H. (1970). *Stochastic Processes and Filtering Theory*. Vol. 64 of *Mathematics in science and engineering*. Academic Press, Inc.. London.

Jørgensen, J.L. (1995). Development of the Ørsted Precision Attitude Instrument the Star Imager. In proc.: *The Chapman Conf. on Measurement Techniques for Space Plasmas*.

Kalman, R. E. (1960). A new approach to linear filtering and prediction problems. *Transaction of ASME, Series D, Journal of Basic Engineering* **82**, 35–45.

Kane, T. R., P. W. Likins and D. A. Levinson (1983). *Spacecraft Dynamics*. McGraw-Hill.

Langel, R. A. (1987). The main geomagnetic field. In: *Geomagnetism* (J. A. Jacobs, Ed.). Chap. 4, pp. 249–512. Academic Press.

Larson, W. J. and Wertz, J. R., Eds.) (1992). *Space Mission Analysis and Design*. Luwer Academic Publishers.

Lefferts, E. J., F. L. Markley and M. D. Shuster (1982). Kalman Filtering for Spacecraft Attitude Determination. *Journal of Guidance and Control* **5**(5), 417–429.

Lerner, G.M. (1978). *Spacecraft Attitude Determination and Control*. Chap. Three-Axis Attitude Determination, pp. 420–428. Reidel, Dordrecht, The Netherlands.

Liebe, C. C. (1995). Star Trackers for Attitude Determination. *IEEE Aerospace and Electronic Systems Magazine* **10**(6), 10–16.

Lightsey, E. G., E. E. Cohen, W .A. Feess and B. W. Parkinson (94). Analysis os spacecraft attitude Measurements using onboard GPS. *Advances in the Astronautical Sciences* **86**, 521–532.

Ljung, L. (1979). Asymptotic Behavior of the Extended Kalman Filter as a Parameter Estimator for Linear Systems. **24**(1), 36–50.

Ljung, L. (1987). *System Identification, Theory for the User*. Prentice-Hall information and system sciences series. Prentice-Hall.

Luehr, H. (1997). Magnetfeldmessungen auf dem schwedish-deutchen Satelliten FREJA. Technical report. Technischen Universitaet Braunschweig.

Markley, F. L. (1988). Attitude Determination Using Vector Observations and the Singular Value Decomposition. *Journal of the Astronautical Sciences* **36**(3), 245–258.

Markley, F. L. (1993). Attitude Determination Using Vector Observations: A Fast Optimal Matrix Algorithm. *Journal of the Astronautical Sciences* **41**(2), 261–280.

Maybeck, P. S. (1979*a*). *Stochastic Models, Estimation, and Control*. Vol. 1. Academic Press.

Maybeck, P. S. (1979*b*). *Stochastic Models, Estimation, and Control*. Vol. 2. Academic Press.

Melvin, P.J. and A. S. Hope (1993). Satellite attitude determination with GPS. *Advances in the Astronautical Sciences* **85**, 59–78.

Natanson, G. (1993). A Deterministic Method for Estimating Attitude From Magnetometer Data. In proc.: *43rd Congress of the International Astronautical Federation*.

Nielsen, O. V., B. Hernando, J.R. Petersen and F. Primdahl (1990). Miniaturisation of Low-Cost Metalic Glass Flux-Gate Sensors. *Magnetism and Magnetic Materials* **83**, 404–406.

Nijmeijer, H. and T. I. Fossen (1999). *New Directions in Nonlinear Observer Design*. Vol. 244 of *Lecture Notes in Control and Information Sciences*. Springer-Verlag.

Oshman, Y. (1999). Private Communication.

Oshman, Y. and F. L. Markley (1999). Sequential Attitude and Attitude-Rate Estimation Using Integrated-Rate Parameters. *Journal of the Astronautical Sciences* **22**(3), 385–394.

Overschee, P. Van and B. De Moor (1996). *Subspace Identification for Linear Systems: Theory-Implementation-Applications*. Kluwer Academic Publishers.

Padgett, C., K. Kreutz-Delgado and S. Udomkesmalee (1997). Evaluation of Star Identification Techniques. *Journal of Guidance, control, and Dynamics* **20**(2), 259–267.

Primdahl, F. and P. A. Jensen (1984). Dansk Rumforskningsinstitut's raket magnetometer eksperiment (in danish). *Gamma, Tidskrift for fysik*.

Psiaki, M. L., F. Martel and P. K. Pal (1990). Three-Axis Attitude Determination via Kalman Filtering of Magnetometer Data. *Journal of Guidance, Control and Dynamics* **13**(3), 506–514.

Rauch, H. E., F. Tung and C.T. Striebel (1965). Maximum likelihood estimates of linear dynamic systems. *AIAA Journal* **3**(8), 1445–1450.

Reigber, C., (Ed.) (1996). *Champ, Phase B*. Scientific technical report STR96/13. champ project office.

Schei, T. S. (1997). A Finite-Difference Method for Linearization in Nonlinear Estimation Algorithms. *Automatica*.

Shuster, M. D. (1989). A Simple Kalman Filter and Smoother for Spacecraft Attitude. *Journal of the Astronautical Sciences* **37**(1), 89–106.

Shuster, M. D. (1993). A Survey of Atttitude Representations. *Journal of the Astronautical Sciences*.

Shuster, M. D. and S.D Oh (1981). Attitude Determination from Vector Observations. *Journal of Guidance and Control* **4**(1), 70–77.

Stuelpnagel, J. D. (1964). On the Parametrization of the three-dimensional rotation group. *SIAM review* **6**, 422–430.

Thornton, C.L. (1976). Triangular Covariance Factorization for Kalman Filtering. Ph.d. thesis. University of California at Los Angeles.

Wahba, G. (1965). A Least Squares Estimate of Satellite Attitude. *SIAM Review* **7**(3), 409.

Wertz, J. R., (Ed.) (1978). *Spacecraft Attitude Determination and Control*. Kluwer Academic Publishers.

Wisniewski, R. (1997). Satellite Attitude Control Using Only Magnetic Actuation. PhD thesis. Aalborg University.

Zhou, W.-W. and M. Blanke (1989). Idenfitication of a Class of Nonlinear State-Space Models Using RPE Techniques. *IEEE Transaction on Automatic Control* **34**(3), 312–316.